Color Measurement at Low Light Levels

Mehdi Rezagholizadeh

Doctor of Philosophy

Department of Electrical and Computer Engineering

McGill University

Montreal,Quebec

2016

A thesis submitted to McGill University in partial fulfilment of the requirements for the degree of Doctor of Philosophy

DEDICATION

This thesis is dedicated to my mother
for her continued support and endless love, and to my brother, Ali,
who had to face the hardships of supporting my parents alone while I
was away from the family, to my father to whom I am gratefully
indebted and to my beloved wife, and to the new member of our
family, Kowsar.

And to the memory of my sister-in-law, Parisa.

ACKNOWLEDGEMENTS

This research project would not have been possible without the support of many people. I would like to thank them all who contributed to this thesis.

I would first like to thank the most my supervisor, Professor Clark, who was not only my PhD research advisor but also the one who helped me in creating my career path and a teacher who I learned from a lot. He helped me in making hard decisions during this period and trusted me all the time. I have always benefited from his illuminating scientific advice and valuable knowledge and support.

I owe my deepest gratitude to my colleagues (especially Ms. Tara Akhavan and Ms. Afsoon Soudi) from my internship at Irystec Inc. for their wonderful collaboration. They supported me greatly and were always willing to help me. I want to thank them for the excellent cooperation and for all the opportunities I was given to conduct my research. And I would like to kindly thank TandemLaunch Inc. and Irystec Inc. for running the subjective evaluation study for my research.

I am very grateful to the members of my committee, Professor Langer, Professor Arbel, Professor Funt, Professor Mullen and Professor Nowrouzezahrai for their time and expertise and their great comments on my research.

I am deeply indebted to my colleagues who supported me during my research in Centre for Intelligent Machines (CIM) and my group-mates in the Visual Motor Research Lab. I specially thank Jonathan Bouchard, Amin Haji-Abolhassani, Siavash Gorji, Yasin Nazzar, Qing Tian and Mehrsan Javan.

Furthermore, I should thank Dr. Y. Lin-Alexander, McGill Engineering Doctoral

Award (MEDA), Mitacs internship programs, Fonds Qubcois de la Recherche sur la Nature et les Technologies (FQRNT), and Natural Sciences and Engineering Research Council of Canada (NSERC) for their support of this work.

Last but not least, this research would not happen without the sacrifice of my mother, mother-in-law, and beloved wife.

ABSTRACT

Ambient light level drives the human visual system into three phases: scotopic, mesopic and photopic vision. In photopic conditions, light level is far above the visual system activation threshold; cones are mainly responsible for our color vision and rods are saturated due to their higher sensitivity to light. Mesopic range refers to the condition where both cones and rods are active and contribute to color vision. In scotopic vision, the light level is very low such that cones are inactive (i.e. there is no color vision); however, rods are still able to contribute to our vision.

Low light vision is of high importance in many computer vision and color science applications such as night time driving, display industry, consumer electronics, virtual reality devices, image sensors and photography at night mode. However, study of low light vision is acquainted with several challenges such as: first, the uncertainty and noise come into play; second, color perception mechanisms of the human visual system are not fully known; third, the number of existing research and models in the literature is small; fourth, computer vision field and industry are far behind not only the current findings, but also the existing well-known perceptual models in the domain.

The human visual system is driven by photons. The details of the colorful journey of photons from triggering photoreceptors to the final visual perception stage inside the visual system is still to a high extent unknown. The methodology of this thesis involves: studying from first principles the physical rules governing the probabilistic nature of human vision at low light levels; modeling mesopic color perception using

the maximum entropy based spectral theory of color vision; and then developing a real time bidirectional mesopic color appearance model to be used in the image rendering algorithms which are responsible for reproducing colors of the image as they appear in the original scene.

Several simulations and computational tests on various datasets with real world and synthetic images are performed, and the methods proposed in this thesis are compared with other existing techniques. The results show the importance of mesopic color appearance modeling and the vital role of noise at low light levels. Moreover, the results support the feasibility of spectral modeling for mesopic vision, and this thesis suggest a bidirectional color appearance model for the purpose of luminance retargeting of images in the image rendering pipeline.

ABRÉGÉ

Le niveau de luminance ambiant entraine le système visuel humain dans trois domaines : la vision scotopique, mésopique et photopique. En condition photopique, la luminance est de loin supérieure au seuil dactivation des cônes; les cônes sont principalement responsables de notre perception chromatique et les bâtonnets sont saturés à cause de leur plus grande sensibilité à la lumire. Le domaine msopique se rapporte à la condition où les cônes et les bâtonnets sont actifs et contribuent à la perception chromatique : la luminance est au-dessus du seuil du cône et au-dessous de la marge de saturation du bâtonnet. Dans la vision scotopique, la luminance est très basse telle que les cônes sont inactifs; cependant, elle est toujours au-dessus du seuil de détection des bâtonnets. Cette thèse se concentre sur la vision mésopique et scotopique et étudie la perception humaine des couleurs en ces deux domaines du système visuel humain.

La vision en faible luminance est d'une grande importance dans plusieurs applications de la vision par ordinateur et de la colorimétrie tels que la conduite de nuit, l'industrie de l'affichage, l'électronique grand public, les dispositifs de réalité virtuelle, les capteurs d'images et la photographie en mode nocturne. Cependant, l'étude de la perception chromatique en faible luminance est accompagnée de plusieurs défis comme : premièrement, l'entrée en jeu de l'incertitude et du bruit; deuxièmement, la méconnaissance de la plupart des mécanismes de la perception chromatique chez l'humain; troisièmement, le faible nombre de recherches existantes et de modèles dans la littérature; quatrièmement, le retard du domaine de la vision par ordinateur et de

l'industrie non seulement en termes de résultats actuels, mais également au niveau des modèles perceptuels bien connus du domaine.

Le système visuel humain réagit aux photons qui atteignent la rétine. Les détails du voyage haut en couleur des photons, du déclenchement des photorécepteurs à l'étape finale de perception visuelle à l'intérieur du système visuel, sont en grande partie toujours inconnus. La méthodologie de cette thèse comprend : l'étude des lois physiques qui régissent la nature probabiliste de la vision humaine en conditions de faible luminance; la modélisation de la perception mésopique des couleurs en utilisant la théorie spectrale de la vision chromatique basée sur l'entropie maximale; et le développement d'un modèle mésopique d'apparence de la couleur bidirectionnel et temps réel qui peut être utilisé par les algorithmes de rendu d'image qui sont responsables de la reproduction des couleurs en conditions de faible luminance de façon fidèle à la scéne originale.

Plusieurs expériences objectives sur divers ensembles de données avec des images réeles et synthétiques sont exécutes et les méthodes proposées dans cette thèse sont comparées à d'autres techniques existantes. Les résultats démontrent l'importance de la modélisation de l'apparence des couleurs (color appearance modeling) en condition de faible luminance et le rôle essentiel du bruit en de telles conditions. Plus encore, les résultats démontrent la faisabilité de la modélisation spectrale pour la vision mésopique et cette thèse suggère un modèle bidirectionnel d'apparence des couleurs à des fins de recalage de la luminance des images dans le pipeline de rendu d'image.

TABLE OF CONTENTS

LIST OF TABLES

LIST OF FIGURES

LIST OF ACRONYMS

HVS	Human Visual System
CRT	Cathode Ray Tube
CAM	Color Appearance Model
iCAM	image Color Appearance Model
OLED	Organic Light Emitting Diode
GMA	Gamut Mapping Algorithms
GRA	Gamut Reduction Algorithms
GEA	Gamut Extension Algorithms
IQA	Image quality assessment
CVD	Color vision deficiency
SNR	Signal to noise ratio
CMOS	Complementary MetalOxideSemiconductor
CCD	Charge Coupled Device
ADC	Analog to Digital Conversion
DAC	Digital to Analog Conversion
HDR	High Dynamic Range
SPD	Spectral Power Distribution
PCA	Principal Component Analysis
EGR	Effective Gamut Ratio
JND	Just Noticeable Difference

CHAPTER 1
Introduction

The human visual system (HVS) is able to work effectively over a wide luminance range from starlight to sunlight, which can be categorized into the so-called photopic, mesopic and scotopic ranges. Photopic vision refers to our vision in day light situations (high light levels, when the luminance is above 10 cd/m^2 [1]) in which only cones are responsible for our vision. As the light level falls off (e.g. at twilight when the luminance level is in the [0.001 10] cd/m^2 range [1]), the visual system goes smoothly from photopic vision to mesopic vision, in which both cones and rods contribute to color vision. In the so-called scotopic situations (e.g. at night when luminance is below 0.001 cd/m^2 [1]), vision is only mediated by rods, and we lose our color perception. The photopic condition has been the main focus of most color research, and the mesopic and scotopic conditions have not been investigated very much [8]. It is worth mentioning that throughout the thesis, the term "*low light*" will only be used when we refer to both mesopic and scotopic conditions.

1.1 Problem Statement

While the human visual system can adapt itself to a wide range of light levels, it is desirable to have imaging devices, such as cameras, be able to operate in a similar range as well. However, the current technology is far behind the capability of human eye. The fact that the human visual system can accommodate low light situations necessitates the importance of studying low light levels. However, studying

the human visual system at low light levels comes with several challenges that will be discussed briefly in the following.

Most of the theories, measures, models and methods in color science have been developed for high intensities [8]. These theories, measures, methods, and models cannot be used for low light situations. For instance, a color difference formulae which is derived for photopic conditions can not be leveraged in evaluating techniques developed for assessing dark images [9].

Low light levels usually introduces some noise and uncertainty into the human visual perception. Furthermore, the issue of noise, which is also a serious concern for CMOS image sensors, especially at low signal levels, has not been fully addressed in the literature. The main reason for this is that, to a large extent, the human color vision mechanisms have not been well understood.

Color appearance models (CAMs) provide a tool to transform tristimulus values to perceptual attributes of color. Color perception algorithms developed for machine vision mostly rely on color appearance models. The outcome of an ideal color appearance model should resemble human color perception in all conditions such as different adaptation, light levels and viewing conditions. Although there are a couple of comprehensive color appearance models for the photopic condition, none of them perform well in the mesopic range. This implies that mesopic color perception mechanisms are different from photopic perceptual mechanisms. This difference can be partly explained by rod intrusion into color perception of mesopic vision. Hence, we end up with a third problem: to a large extent, the human color vision mechanisms

have not been well understood. There are only a few currently available color appearance models suited to the mesopic range, none of which perform well in terms of resembling human perception. Moreover, these models are ad-hoc empirical models.

In today's world, every individual spends a lot of time in front of displays in various applications such as consumer electronic devices (e.g. smart phones, tablets and laptops), automotive industry [10], and virtual reality interfaces (e.g. head-mounted displays). Working with bright displays raises power consumption and eye strain issues which affect customer satisfaction. For example, it has shown that using e-Readers with backlighting interferes with the human circadian rhythm [11]. Dimming the display is a trivial solution to both issues. The new display technologies, such as OLED, let the user dim the display to less than 2 cd/m^2, which is in the mesopic range. However, dimming the display to the mesopic range reduces visual acuity, and especially the perceived quality of colors in images. Hence, a compensation algorithm should be employed to preserve the color appearance quality of the original image on the dimmed display [2].

In this thesis, we focus on the following three main problems at low light levels:

1. investigating effects of different types of noise on the cone responses and image sensor color measurements at low light levels (scotopic and mesopic range);
2. developing a mesopic vision model which is able to take the measurement noise into account;
3. developing an image compensation algorithm to keep the color appearance of bright images on a dim display which is viewed in a dark environment.

Addressing low light level situations has a wide range of applications in photography [12],designing biosensors [13], image processing [14], machine vision, and color science [15]. Working under low light conditions is of particular interest in machine vision applications such as night vision, tone-mapping techniques, low-light imaging, photography, and surveillance cameras. We elaborate some of the use cases in more detail in section 1.3.

1.2 Approach

Human vision is mediated by photons captured by the photoreceptors. Our research methodology involves understanding color measurements from the primary level of photon detection. In this regard, using the physical principles, we model the photon detection process by the photoreceptors or image sensors. This principal step will help us to extract the basic principles governing the probabilistic nature of photoreceptors responses and color measurements at low light levels. Achieving this goal will enable us to attain other objectives of primary concern in machine vision research e.g. addressing mesopic and scotopic conditions in current digital cameras, and introducing efficient denoising algorithms.

Moreover, the methodology of this research involves spectral modeling of mesopic color vision, which gives us a powerful tool for taking noise in color measurements into account. The "spectral theory of color perception" was proposed by Clark and Skaff [16]. This technique is a maximum entropy spectral modeling approach, which has potential for modeling color vision when noise is involved. The Clark and Skaff model treats the noise as an inherent part of the modeling process, and an estimate of the noise level sets the trade-off between the consistency of the solution with

the measurements and the spectral smoothing imposed by the maximum entropy constraint.

At the final step, our goal is to employ a suitable mesopic color appearance model in the color retargeting algorithms to be used in the image rendering pipeline of displays. Color retargeting algorithms aim to adjust the colors of the rendered image on a display according to the intended luminance level of the original image and the bright level of the display. An image retargeting algorithm employs an appropriate color appearance model and the inverse of this color appearance model at the same time. In this research, the inverse of a color appearance model will be developed to serve an image retargeting algorithm.

In summary, this thesis has some theoretical contributions to the study of low signal to noise color measurement and color appearance modeling. During this work, several computational tests, simulations and experiments are done in order to investigate the performance of modeling. Furthermore, this work has a wide range of applications as mentioned in 1.3.

1.3 Applications

1.3.1 Display Technology

Ajito, Obi, Yamaguchi, and Ohyama [17] point out that "The range of the reproducible color, i.e., color gamut, of the conventional display devices such as CRTs (cathode ray tubes) and LCDs (liquid crystal displays) is sometimes insufficient for reproducing the natural color of an object through color imaging systems." With emerging new technologies such as quantum dots and organic light emitting diodes (OLEDs), display technology has been advancing quickly giving users a broader color

experience. OLED displays have narrow-band primaries which give rise to a larger gamut area compared to conventional LCD displays, and they have great potential for displaying high quality images and saturated colors [18]. Due to their emissive pixel structure, OLED displays exhibit a high contrast ratio, and a high and constant color gamut at all luminances. However, there are some perceptual issues that should be addressed for the wide gamut displays such as observer metameric failure [19], and gamut mapping between the input image and the display gamut.

Metameric failure refers to having noticeably different color perception by two observers on a single display at the same time [20]. Displays with narrow-band primaries are more susceptible to observer metamerism as compared to conventional displays such as CRTs [21]. All existing color models and standards are developed based on the mean observer (also called standard observer) color matching functions. However, studies show that the mean observer may fail to match individual observers significantly [20]. We can think of two types of solutions for the observer metamerism failure: hardware solutions [22, 23, 24, 21, 25] and software approaches [26, 27, 20]. Bear in mind that metamerism on dimmed displays would be intensified due to the increased uncertainties in the visual system and lower signal to noise value of displays at low light levels.

Gamut mapping algorithms (GMAs) are divided into gamut reduction and gamut extension algorithms [28, 29, 30, 31, 32]. In contrary to old display technologies (with smaller gamut than the input image), for which gamut reduction algorithms (GRAs) were employed to fit the image gamut to the display gamut, wide gamut displays have a larger gamut than the standard sRGB gamut (i.e. the

color space which is commonly used to represent captured images from imaging devices). Hence, gamut extension algorithms (GEAs) emerged to be used for wide gamut displays. However, the number of available GEAs is not large as compared to available GRAs [33, 28, 33, 34]. Moreover, there are some challenges in the area of gamut mapping: first, most GEAs output oversaturated images [33], second, GMAs usually are not good in keeping the perceptual fidelity of the original image on the rendering medium [35]; third, GMAs usually alter the skin tone and memory colors, and people are more sensitive to skin tone and memory color changes [36, 37]; fourth, dark images are more prone to noise and applying gamut extension algorithms may intensify chromatic noise. Hence, it turns out that GMAs have yet to be improved to address the mentioned challenges [33, 38].

1.3.2 Tone Mapping and High Dynamic Range Images

Tone mapping refers to the process of mapping high dynamic range image data to a relatively low dynamic range rendering medium (e.g. displays or printers) in a way that the reproduced image perceptually matches the original scene. Tone mapping algorithms should be informed by accurate color appearance models so that the perceptual fidelity of the output image is maintained after applying the tone mapping transformations. The problem is that existing tone mapping techniques suffer from lack of good CAMs for mesopic conditions. Current tone mapping techniques and color appearance models are trying to solve different problems; however, as Erik Reinhard states in [39], these two are two sides of the same coin (i.e. tone reproduction algorithms and color appearance models should unify to predict the correct appearance of images with a wide range of intensities).

1.3.3 Image Quality Assessment

Image quality assessment (IQA) aims at measuring the quality of an image in terms of appearance from different perspectives such as image naturalness, clarity, sharpness, color, noise, contrast and lightness. Assessing image quality may be achieved by employing a human subject who can tell us how good an image may look like from a specific quality attribute point of interest. This approach gives us a subjective quality measure; however, we may desire an objective way of assessing image quality. The objective approach is defined as a set of mathematical models and computational techniques to address image quality measurements. Here a question may arise that what the benefit of such an approach would be? A particular application of objective image quality assessment techniques is to replace a human subject in evaluating the quality of images, and accordingly, gives rise to a less expensive, more effective, more repeatable and consistent, and more time efficient approach to achieve this goal [40]. Hence, objective methods are geared to constructing automated systems to predict the quality of images as they appear to a human observer. These methods leverage different approaches to achieve the desirable performance, from the simple computational models to highly complicated models of human visual system (HVS) [41].

We can determine the precision of each objective image quality measure by comparing the given results of the measure with those of the human subjective evaluations; however, most of the readily available objective metrics are developed based on simple test patches and can not be used for more complex scenes such as natural images. Moreover, most IQA techniques employ a color difference formula between

the test image and reference image [42]. The choice of the color difference formula is different for various algorithms but the common issue for all of them is that they fail to comply with the assumptions for which that formula is valid. Lucassen et. al in [9] mentioned that "*These formulae are tuned to an ever increasing number of data sets obtained from human observers in vision experiments employing specific stimulus sizes and viewing conditions, the so called reference conditions. When applying such a color difference equation however, one should be aware of its preferred reference conditions, and hence its limitations for some practical cases.*" Color difference formulas can be used under certain conditions such as a specific viewing condition or under a limited range of luminance levels (usually photopic conditions).

1.3.4 Color Identification

The micro-array sensor biochip, is a miniaturized laboratory comprised of arrays of sensing elements integrated in a CMOS chip, designed in a way that they can respond to a specific biological reaction or a biological element such as DNA hybridization [43]. Some types of biochips, such as **colorimetric biosensors** or **fluorescence biosensors**, use color changes as a salient feature for detecting their target. To avoid the high workload required for labeling color changes manually, a color appearance technique which is reliable under low signal to noise ratios, may be employed to replace humans.

1.3.5 Image Enhancement for Color Deficient People

Color vision deficiency (CVD) refers to a variation in the cone photoreceptors spectral sensitivity (i.e. a shift in the spectral cone sensitivity functions or lack of one type of L, M, and S cones or more). CVD can be categorized into three classes:

anomalous trichromacy (that is a shift in the spectral sensitivity of one cone type), dichromacy (that is the lack of one cone type), and monochromacy (that is missing two or three cone photoreceptor types in the retina). The first two groups form 99.9% of all color-deficiencies and about a quarter of these are dichromats [44]. Dichromats can be divided into *protanopes*, *deuteranopes*, and *tritanopes*. The first two categories are close enough in term of their symptoms such that they take a single name as *red-green* dichromats. The perceptual color space of dichromats is two-dimensional. Hence, dichromats can not discriminate colors as well as color normal people do and consequently, they may occasionally find object recognition or color identification a harder task as compared to other people in their life. For example in [45], it is argued that the number of colors used to visualize information in geographical maps is not optimized for color deficient people. Existing solutions for color-blindness can be divided into hardware and software solutions. As a hardware solution, color-blindness glasses use color filters to help color-deficient people to improve their color discriminability. Although they are able to address the discriminability issue for some colors, they usually bring about some other color confusions [44]. Software solutions provide some techniques to take into account color-blindness for electronic devices.

Techniques for dealing with color deficiency can be classified into the simulation and recoloring (compensation) approaches [46]. Simulation techniques can help color normal observers to see how colors may appear to color deficient people. Having a good color appearance model for color-blind people is deemed necessary for any recoloring technique. There are many simulation models in the literature and most

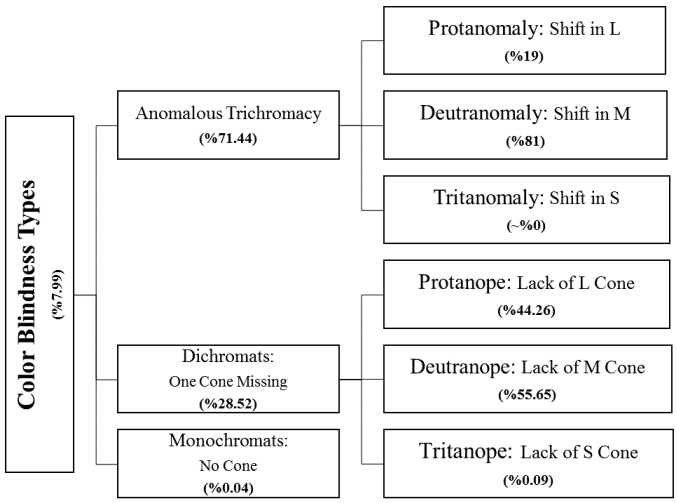

Figure 1–1: Different types of color-blindness

of them are using linear models based on projecting the 3-dimensional color space of color normal people onto the two dimensional subspace of dichromats. However, it is reported that the 2 dimensional representation of dichromat's color perception space cannot explain the extensive color perception experience of color deficient observers [47].

Recoloring techniques aim at improving the color contrast for color-blind people. As a case in point, a real-time temporally coherent recoloring technique is introduced in [46]. The rational behind this technique is that in a perceptual uniform color space, if we find the direction in a color space along which the maximum color contrast loss in the image takes place for a color-deficient observer, then by recoloring the image we would be able to recover the most possible color contrast loss for that observer.

There are several factors that could be taken into account in proposing a recoloring technique:

1. being real-time,
2. keeping naturalness of colors for color vision deficient people,
3. keeping color contrast,
4. preserving temporal coherence (i.e. the mapped colors should not change a lot with a small difference in the image content by the recoloring techniques),
5. keeping similar perceptual difference in the images as for trichromats,
6. neutral colors should be kept neutral after mapping

However, none of the available recoloring methods is able to take all of these factors into account at the same time. Furthermore, Paramei, Bimler, and Cavonius indicate that luminance is an important factor in the color perception of protanopes [48]. However, to the best of our knowledge, the effect of luminance, especially in mesopic range, on the color appearance of color deficient people has not yet investigated completely and not considered in any recoloring technique.

1.3.6 Chromatic Noise Removal

Color noise (or chromatic noise) can be defined as any unwanted distortion or artifacts that may occur in chromatic channels of an image. Evaluating and removing color noise will help us to make optimal color measurement and reproduction systems. Signal to noise ratio (SNR) is one of the conventional and well-known methods of evaluating noise not only in image processing but also in the general signal processing field. However, signal to noise ratio is not a suitable measure in the context of color noise perception and consequently image quality assessment as a whole, because it is not a perceptual quantity (i.e. it does not necessarily match the human perception). Much research has been focused on introducing a proper perceptual measure for

chromatic noise and several metrics have been proposed [49, 50, 51, 52, 53, 54, 55]. Similar to IQA techniques, absolute color noise levels can be measured using a color difference formula; hence, this shows the necessity of employing appropriate color difference measures. At the present time, CIE94, CIEDE2000, and CIELab color difference formulae are mostly used for this purpose [56].

Aside from the effect of noise on the perceptual quality of an image, there are many well-known image post-processing operators such as image enhancement and tone mapping which result in boosting noise levels [57]. Hence, it is of high importance to remove noise from the image before displaying it or doing any post processing operation. While there are many noise removal techniques proposed for gray-scale images and from the luminance channel, chromatic noise has gained less attention due to the lower visibility of chromatic noise as compared to achromatic noise [58, 59, 60, 61, 62]. The higher visibility of achromatic noise as compared to chromatic noise stems from the visual system spatial and temporal contrast sensitivity functions. The luminance contrast sensitivity function has a band-pass nature with respect to the spatial and temporal dimensions as compared to the low-pass shape of the chromatic contrast sensitivity functions. [63]. The importance of removing chromatic noise from dark images will be investigated in this thesis.

1.4 Thesis Contributions

The contributions of this thesis are as follows:

1. Development of a photon-accurate model of cone photoreceptor responses for use in studying cone signals close to the absolute threshold of the visual system

(a) It is shown that close to the absolute threshold of the visual system, cone responses become noisy and the distribution of the chromaticity representation of cone responses form an elliptical shape over time.

(b) It is demonstrated that the spectral composition of light falling on cones affects the size and orientation of the ellipses fitted to the distribution of the chromaticity representation of the cone responses.

2. Development of a photon-accurate image sensor model to analyse the color measurement at low light levels

   (a) photon noise, read noise, and quantization error as shown to lead to uncertain measurements distributed around the noise free measurements; and the chromaticity of these noisy samples are distributed in a cloud that can be well-fit to an elliptical region in the xy-chromaticity diagram.

   (b) It is shown that, even for an ideal image sensor, in scotopic conditions, obtaining stable measurements of color is impossible due to the physical limitation imposed by the fluctuations in the photon emission rate

   (c) It is demonstrated that, as compared to the chromaticity of noise-free measurements, dark current shifts the chromaticity of measured samples towards the chromaticity of the camera black point in the xy-chromaticity diagram. The amount of this shift depends on the light levels; the lower the luminance is, the larger the amount of the shift would be.

   (d) It is shown that dark current dominates the other sensor noise types in the image sensor.

3. Development of a maximum entropy spectral modeling approach to mesopic vision
   (a) Evaluation of existing mesopic vision models
   (b) Unification of photopic, mesopic, and scotopic vision models in the spectral theory of color vision
   (c) The first mesopic vision model which takes noise into account is presented
   (d) Incorporating the recent CIE system for mesopic photometry in a color vision model
4. Development of a color retargeting approach for mesopic vision to serve image rendering algorithms
   (a) application of the Shin CAM to real world images,
   (b) derivation of the inverse of Shin's mesopic color appearance model,
   (c) development of a color retargeting approach based on Shin's model,
   (d) development of a technique for perceptual rendering of images and compensating color deviations imposed by the human visual system while viewing a dimmed display in the dark.

1.5 Thesis Overview

In this thesis, color measurement and color perception at low light levels are studied. In this regard, the photon detection processes of photoreceptors/image sensor is modeled by taking the physical principles underlying photon emission/absorption into account at low light levels. We divide the low light region into night and twilight conditions. These two conditions, which relate to scotopic and mesopic range of the human visual system, are studied in this thesis respectively.

The first chapter introduces the problems, their importance from different perspectives (applications), and the approaches taken to address the problems. In **Chapter 2**, background information is presented and a comprehensive literature review of the existing theories is done.

Chapter 3 investigates uncertainties in ideal cone responses in the scotopic range caused by photon emission. In this regard, physical principles are leveraged to develop a framework to take into account the effects of the probabilistic nature of photon emission (the photon noise) on the ideal cone responses. Applying this model results in the observation that the normalized spectral power distribution of light becomes more uncertain (noisier) at low light levels than at high light levels which leads to an increase in the uncertainty of cone responses. Furthermore, a colored patch viewed in the scotopic range gives rise to uncertain color measurements (by ideal cone cells) whose chromaticities are distributed over an area of roughly elliptical shape centered on the high intensity chromaticity of the color patch. The size of these elliptical regions is a function of the light intensity and the chromaticity of color patches; however the orientation of the ellipses depends only on the patch chromaticity and not on the light level. Moreover, the results of this work indicate that the spectral composition of light is a determining factor in the size and orientation of the ellipses. The material in this chapter was published and presented in *IEEE Conference on Computer and Robot Vision 2014* [15], for which the candidate was the first author, and performed the work described therein, and did the writing of the manuscript.

Chapter 4 concerns modeling the color measurement performance of image sensors under low signal-to-noise ratios. Our methodology involves tracking photons to the moment when they are absorbed and measured by different channels of the image sensor. In this regard, physical law governing photon emission are employed to derive an estimate of the low light spectral power distribution of the light coming to the image sensor. Then, an image sensor model is implemented and used to study the luminance and noise induced effects on the sensor color measurements. The methodology and results of this chapter was published as a journal paper in the *Journal of Imaging Science and Technology* [64]. The candidate was the first author of this paper, and developed the method, performed the simulations and wrote the manuscript.

In **Chapter 5**, we evaluate some of the most prominent color vision models available for mesopic range. We introduce a spectral-based color vision model for mesopic conditions based on the maximum entropy spectral modeling approach of Clark and Skaff [16], which was developed for photopic range. The extension of this model can predict the color appearance under mesopic conditions as well as the photopic range. Moreover, this method incorporates the new CIE system for mesopic photometry, leading to an increased accuracy of the model. In mesopic vision, two factors come into play as compared with the photopic spectral modeling. First of all, image noise becomes significant. The Clark-Skaff model treats the noise as an inherent part of the color vision modeling process, and an estimate of the noise level sets the trade-off between the consistency of the solution with the measurements and the spectral smoothing imposed by the maximum entropy constraint. Second of all,

both the rod and the cone systems are active. The relative contribution of the rod and cone systems depends on the overall light level in this regime, and our approach is adaptive in this sense. We perform several computational tests and simulations to compare the performance of our spectral mesopic color vision model with that of the existing methods. The results show that the proposed method works very well in this regard, and also demonstrates the potential of our model to become a part of the existing tone mapping algorithms. We also propose a color retargeting algorithm based on Shin's model [65] to be used in the color rendering pipeline of displays. The main contributions of this algorithm are as follows:

I- application of the Shin CAM to a real world image,

II- derivation of the inverse of Shin's model,

III- development of a color retargeting approach based on Shin's model,

IV- perceptual rendering of dark images and compensation of color deviations imposed by the human visual system while viewing a dimmed display in the dark.

Sections 5.1 and 5.2.1 of this chapter were published and presented in the *Color Imaging Conference 2013* [8]. The candidate was the first author of this paper, performed the work described therein, and did the writing of the manuscript. The remaining of this chapter represents the research which was done in a collaboration with our industrial partner, IRYStec Software Inc. In this regards, the development of the theories and performing the quantitative evaluation was done mainly by the candidate. This research was published in the Journal of Imaging Science and Technology in which the candidate was the first author and wrote the manuscript [7].

Chapter 6 concludes the thesis and proposes future work according to the results and contributions of this thesis.

CHAPTER 2
Literature Review

In this chapter, we will review the literature of mesopic color perception and scotopic vision. First, a background knowledge of human visual system operation at low light levels will be presented. Then, we will briefly go over the microscopic view of how individual photoreceptors respond to the coming photons and what happens to human vision in the scotopic range. Next, we introduce mesopic vision and existing mesopic color appearance models. Finally, the chapter will be wrapped up by reviewing the application of mesopic color vision models in advanced image rendering and color reproduction techniques.

2.1 Background: Human Visual System

Our visual system is able to adapt to a wide range of light levels from a bright sunny day (around $10^5 cd/m^2$) [66] to star-lit scenes (around $10^{-3} cd/m^2$), [66]. Our eye can capture a high dynamic range of luminance (around 4 orders of magnitude [39]) simultaneously.

According to the light level, the human visual system works in three different modes called: photopic, mesopic and scotopic vision. Photopic vision refers to our vision in day light situations (above 10 cd/m^2 [1]) in which only cones are responsible for our color vision. As the light level falls off to a luminance of 10 cd/m^2 [67], the visual system smoothly goes from photopic vision to mesopic vision, in which both cones and rods contribute to color perception. In the so-called scotopic range (below

Table 2–1: Different modes of the human visual system [1]

The Visual System Mode	Photopic Luminance Range (log cd/m^2)	Responsible Photoreceptors	Status of the Visual System
Photopic	[1 , 6]	Cones	Good Color Vision
Mesopic	[-3 , 1]	Cones and Rods	Poor Color Vision
Scotopic	[-6 , -3]	Rods	No Color Vision

0.001 cd/m^2 [1]), there is no color vision, and human vision is only mediated by rods. The photopic condition has been the main focus of most color research, and the mesopic and scotopic conditions have not been investigated extensively [68, 69, 15].

The human visual system has different sensitivities under different lighting conditions, being less sensitive in bright scenes as compared to dark ones. Weber's law indicates that the just noticeable difference of the stimulus changes with a constant ratio of the stimulus intensity. Adjusting this sensitivity is done partly by changing the pupil size and partly by the cone and rod photoreceptors' adaptation mechanisms. Light level plays an important role in the appearance of colors [70]. In mesopic conditions, an increase in rod contributions leads to enhancement of perceived brightness and a decrease in the saturation of spectral lights. Hue scaling experiments show that rod contributions to mesopic vision results in monochromatic lights in the range of 460-520 nm appearing more bluish, and monochromatic lights in the range of 540-610 nm appearing more greenish [71]. Results of a color identification experiment performed by Ishida indicates that close to the lower luminance range of mesopic vision green is mostly confused with blue and"red", "pink, "orange" and "brown" are reported interchangeably [70].

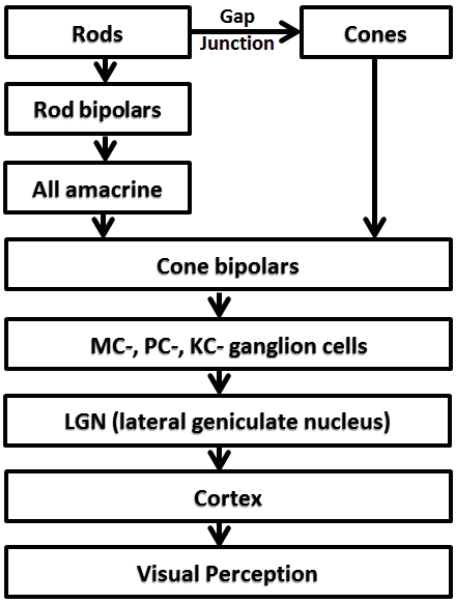

Figure 2–1: The schematic of the visual pathways of the human visual system. This diagram is reproduced from Fig. 10.3 in [3].

2.1.1 Physiological Background of the Human Visual System at Low Light Levels

There are several layers in the human visual system working in parallel to transport photoreceptor responses to the visual cortex. Figure 2–1 shows the schematic of visual pathways of the human visual system. Light falls on the retina and stimulates four types of photoreceptors: the rods and three different cones sensitive to long (L-), medium (M-) and short (S-) wavelengths. The output of a rod cell is connected to a rod bipolar cell and the cone photoreceptor is connected to the cone bipolars (on-bipolar and off-bipolar cells).

Signals from the rod bipolar cells are transmitted to the ganglion cells through amacrine cells and cone bipolars [3]. The ganglion cells then feed to the three pathways which convey the retinal information to visual cortex: the parvocellular pathway

(PC pathway) corresponding to the red/green opponency, magnocellular pathway (MC pathway) corresponding to achromatic signals, and koniocellular pathway (KC pathway) corresponding to the blue/yellow opponency [67]. According to Hering's color opponency theory, there are three pairs of primary colors (and three types of corresponding opponent cells) in the human visual system: red/green, blue/yellow, and white/black [72]. Each type of the opponent cells is sensitive to one of these pairs, and only can respond to one color at a time. For example, the red/green opponent cells are sensitive to both red and green stimuli, but they can only detect red stimulus or green stimulus at a time.

In the photopic condition, rod cells are saturated and only cone cells respond. In the mesopic conditions, a gap junction forms between rods and cone bipolar cells [73, 3]. Rods can contribute to the mesopic color vision through this gap junction[73].

In the scotopic condition, there is no cone contribution to the visual pathways. However, in this condition, rod photoreceptors are very sensitive to light such that they can respond to even a single photon. It is worth mentioning that cones are also able to signal capturing of a single photon, but the resulting response is weaker than for rods.

2.2 Visual Perception under a Rain of Photons

In this section, we review the literature concerning the visual processes triggered by photons. The square root, or *de Vries -Rose Law* holds that at low light levels (but above the absolute threshold of the visual system) contrast detection thresholds are inversely proportional to the square root of the background luminance of the stimulus. This law was discovered by de Vries (1943) and evaluated later by Rose

(1948) who showed that, at low light levels, the detection threshold is determined by quantum fluctuations [74].

The literature can be divided into two different groups: first, rod oriented, and second, cone oriented works. The former concentrates on investigating rod responses to single photons [75]. Researchers have recorded cellular responses to single photons absorbed by rods, a step which opened up a new door to understanding our vision by answering basic questions such as: how many photons are required for seeing or detecting a dark adapted stimulus. The physical fact that photon arrival is governed by a Poisson distribution, together with the rod responses to single photons, led to powerful models of the photon absorption process [76, 77]. These models are able to explain *the frequency of seeing curve* which represents the probability of detecting a dark adapted light stimulus as a function of intensity. In addition to the randomness which arises from the Poisson process driven nature of photon emission, there is another source of fluctuations, which is the internal noise of the visual system. This internal noise is referred to as *dark current*. Dark current is described and modelled in [78, 79]. Reproducibility of the single photon response (i.e. the rod response to a single photon should not change considerably over time) was another achievement of earlier research in explaining rods' ability in counting photons [77]. A complete review of the research in this area can be found in [4]. Schwartz and Rieke proposed that, in scotopic conditions, when photons may arrive at a very low rate, adjusting the adaptation gain of the visual system is performed after absorption of every individual photon is signalled [80]. This finding indicates a highly reliable and fast adaptation

mechanism inside our visual system that is able to respond to even a single photon absorption.

In comparison to rods, less research has been done concerning cones and their responses to photons. This might be due, in part, to the fact that cone sensitivity at low light intensities is lower than that of rods. Does it mean that cones are less capable than rods when it comes to counting photons? Not at all, cones are also able to count photons similar to rods; however, they are more prone to noise. Cone responses are recorded from the outer segment of photoreceptors. Superimposing these responses for dim flashes of light at various wavelengths reveals the *Principle of Univariance,* which states that, once a photon with a certain wavelength is absorbed, the response of the cell is independent of the wavelength of that photon [81]. Other research projects have carried out behavioural experiments to investigate cone absolute threshold in terms of the number of photons required to activate visual pigment molecules [82]. A photon accurate model of the human eye was proposed by Deering [83]. This comprehensive photon absorption and detection model takes the position, size, shape and orientation of cones into account. This model can be deployed in simulating the human visual system and evaluating displays and other image rendering hardware.

2.2.1 What is a single photon able to do?

In 1942, Hecht, Shlaer, and Pirenne performed an experiment to determine what would be the lowest possible intensity for a normal human observer to see a presented flash of light, as a function of the wavelength of the light. In this way they estimated the "*frequency of seeing*" curve [84]. This pioneering work led to many useful and

interesting results and inspired much research in this area [85]. Indeed, the result of *frequency of seeing* experiments acknowledges the importance of physics of the light on our vision.

In this subsection, we look at what a single photon is capable of in terms of its effect on the visual system, and also the perception it may give rise to. Our discussion will be mostly focused on the inherent randomness of photon emission/absorption, especially in low light conditions. Photon emission is governed by a Poisson process whose photon emission rate is set by the light source power and its relative spectral power distribution.

The probability that K or more photons in a unit of time are absorbed by the photoreceptors may be obtained as [86]:

$$P(K, x) = \sum_{m=K}^{\infty} w(m, x) = 1 - \sum_{m=0}^{K-1} w(m, x) \tag{2.1}$$

where the average number of photons absorbed in the unit of time in repeated trials is represented by x; and for a monochromatic stimulus of wavelength λ, the probability of absorbing m photons in a unit of time (absorption rate) by photoreceptors is given by:

$$w(m, x) = \frac{x^m \ e^{-x}}{m!}. \tag{2.2}$$

The above equations are used for the purpose of modeling the *frequency of seeing* curve. However, the quantity x does not thoroughly represent the entire process taking place inside the retina, and needs to be modified before it can be used as a model for the *frequency of seeing* data. The reason is: not all the absorbed photons

contribute to vision; but only those which can initiate the photoisimerization of photoreceptors are involved in that process. Photons reach the cornea with the average rate of $x_{cornea}(\lambda) = \frac{E_{cornea}(\lambda)}{h\nu}(photons.mm^{-2}.sec^{-1})$ where E_{cornea} (in $W\ mm^{-2}$) is the flux density of the source at the cornea. The quantity x_{cornea} can be obtained as follows:

$$x_{retina}(\lambda) = x_{cornea}(\lambda)\frac{A_{pupil}}{A_{retina}}\tau(\lambda) \tag{2.3}$$

where $\tau(\lambda)$ is the transmission correction coefficient for ocular media and A_{pupil} is the area of pupil in mm^2. We assume no correction for the ocular media transmission, so $\tau(\lambda) = 1$. In the next step, the number of absorbed photons is calculated, and this number depends on the wavelength of the incoming photons and the sensitivity of photoreceptors. The mean of the number of photons at the cornea can be obtained as $\overline{N} = x_{cornea}A_{pupil}\Delta T$, where ΔT represents the integration time of the visual system. However, not all of the photons incident on the retina will be absorbed by photoreceptors, and moreover, not all the absorbed photons will lead to successful isomerization. As a result, we can assume that the overall efficiency coefficient α represents the proportion of successful isomerizations to the total number of photons reaching the cornea, R^*.

$$R^* = \alpha\overline{N} \tag{2.4}$$

The term "α" for rods depends on several factors such as: the transmission correction coefficient for ocular media, $\tau(\lambda)$; the fraction of light penetrating into the outer segment of the photoreceptor, f_{guided} where $f_{guided} \leq 1$; the optical density of rhodopsin

$D(\lambda)$ in the outer segment; and the quantum efficiency of successful isomerization, γ.

$$\alpha = \tau(\lambda)\ f_{guided}[1 - 10^{-D(\lambda)}]\gamma \tag{2.5}$$

Based on the above discussion, the probability of seeing can be obtained as follows [82]:

$$P(see|\overline{N}) = P(K, R^*(x)) = \sum_{m=K}^{\infty} w(m, R^*(x)) \tag{2.6}$$

In the probability of seeing expression, there are two free parameters: first, the detection threshold, K (i.e. the number of required photons for seeing); and second, the term α which may vary from person to person. Figure 2–2 shows the effect of these underlying parameters on the shape of the probability of seeing curve. This curve is plotted as a function of mean number of photons at the cornea. It is noteworthy that shape of the curve is independent of the "α" parameter [77].

So far, we have not considered the effect of spontaneous rhodopsin isomerization leading to generate a dark current. In the following, dark current is introduced and taken into account in the probability of seeing formulation.

2.2.1.1 Incorporating Dark Current in the Model

In the preceding subsection, we described the photoisomerization process, which follows photon absorption by a photoreceptor. However, photon absorption is not the only process which may give rise to isomerization; it might also happen spontaneously even when no photon is exposed to a photoreceptor. This spontaneous event is called thermal isomerization and the resulting current in the transduction cascade is known

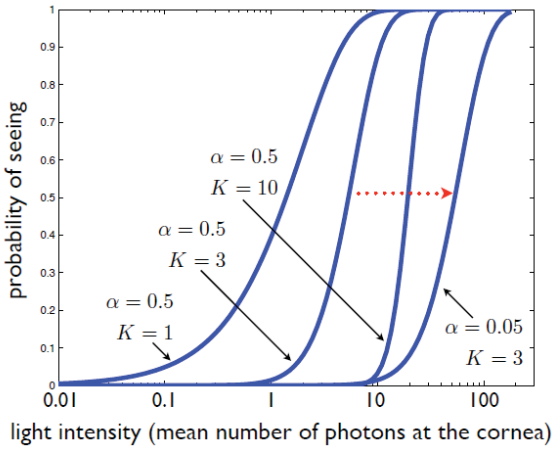

Figure 2–2: The probability of seeing curves for different parameters in the Eq. 2.6. The figure is taken from [4].

as *dark current*. Dark current limits the performance of the visual system, especially in the scotopic range; a case in point is hampering visual detectability. A very well-known model for the probability of seeing experiment taking dark current into account is proposed by Sakitt [78] as follows

$$P(see|\overline{N}) = P(K, R^* + D) = \sum_{m=K}^{\infty} w(m, (R^* + D)) \tag{2.7}$$

where D represents the additive Poisson noise modeling the dark current in the visual system.

2.3 Scotopic Vision Models

In the scotopic range, cone photoreceptors are inactive and only rods are responsible for our vision. It has been known for a long time that rods individually can not give rise to any color perception; however, recent findings show a blue or bluish green color perception even in dim conditions [87]. This bluish perception is

partly explained by the Purkinjie shift effect (i.e. the relative brightness of blue and red objects changes by moving from daylight to a twilight region [86]).

"Day-for-night" simulation is a term in the movie-making field which refers to reproducing scotopic scenes from scenes filmed in photopic conditions. The main reason behind using the day-for-night technique is to avoid the hardships associated with night-time filming and to get high quality images. In the movie-making industry day-for-night simulation can be done by adding a bluish effect, a loss of acuity and desaturation to the photopic image. However, this approach can not completely address the human scotopic visual experience for an observer viewing a scotopic scene on a photopic display [88]. A case in point, to be encountered in day-for-night simulation, is that scotopic visual perception may change according to the surrounding context of a target object [87]. Moreover, it is reported that binocular disparity changes in scotopic conditions and this is suggested to be considered in any realistic scotopic model [88].

Noise is another important factor in scotopic vision modeling, especially when close to the absolute threshold of the visual system. Thompson, Shirley, and Ferwerda proposed that adding noise to day-for-night simulation provides a better quality of scotopic perception [89]. In this regard, a static noise with a normal distribution is introduced. Kellnhofer, Ritschel, Myszkowski, Eisemann, and Seidel introduced a quantal noise model for scotopic vision simulation [90]. This model is more accurate and is plausible when close to the absolute threshold of the visual system. The proposed method can be deployed in future scotopic displays (i.e. displays which are

able to reproduce scotopic conditions and have a screen brightness that can go down to the scotopic range), which have not yet been invented due to technical limitations.

2.3.1 Noise in Visual Systems

For both imaging devices and the human visual system, as the light level goes down, the effect of noise becomes more significant (see the de Vries-Rose Law in Section 2.2) [15]. In this situation, an imaging device will acquire a noisy signal with a low value of signal to noise ratio. In human vision, a lower signal to noise level results in changes in the appearance of measured colors. Several works discussed the impact of light level on human color perception [91, 92, 70, 93]. It is unanimously accepted that reducing the light level gives rise to color shifts (see the Bezold-Brücke effect in Section 2.4), and this effect is mostly attributed to the rod intrusion into the mesopic vision (dim light situation in which both rods and cones contribute to vision) [94, 65]. However, the issue of noise at low light levels is still an ongoing problem for artificial image sensors.

Low light imaging is a challenging issue for photographers due to the low signal to noise level. In this situation, a photographer may be faced with a dilemma: keeping the exposure setting of the camera the same as in regular lighting conditions, which causes a low signal to noise ratio, or increasing the exposure time, which leads to motion blur with hand-held cameras. Noise adversely affects the quality or color appearance of an image taken by an imaging device.

To the best of our knowledge, the effect of noise at low light levels on the color measurements of imaging devices has not been addressed yet. One of the most recent works concerning this topic is the work done by Kirk and O'Brien, which proposes a

perceptual tone mapping approach to convert high dynamic range low light images to a result perceptually closer to the human mesopic vision experience [95]. However, the authors did not take into account any noise in their model and left it as future work. Evaluating color noise will help us in creating optimal color reproduction systems. Additionally, modern cameras are constructed based on digital imaging sensors; and nowadays, due to their easy fabrication and low power consumption, CMOS sensors have become the most prominent imaging sensors. However, the performance of CMOS cameras has yet to be optimised, especially in terms of noise in low light photography [12], and capturing high dynamic range scenes.

Last but not least, linear transformations are widely used in color science. Linear transformation can not ideally map the source and destination color matching functions and this induces some errors in the process of conversion. These errors are usually deemed negligible for a noise-free system. However, in practice, imaging devices, displays, and printers employ linear transformations to move between color spaces and at the same time they are subject to noise which might magnify linear transformation errors. The induced errors can bring about color shifts and reduce image quality. The effects of noise and linear transformation on the color gamut were investigated by us in [96]. In this regard, a typical image sensor is modeled and employed for this study. A detailed model of noise is considered in the process of implementing the image sensor model. Several simulations were performed over the implemented framework and the results show that the imperfections of linear transformation combined with the image sensor noise shrinks the gamut of the

output images. Moreover, in [97], Burns discussed an image noise analysis in multispectral color imaging and pointed out that the underlying error by the color-space transformation is comparable to the intrinsic noise of the image sensor.

2.4 Mesopic Color Appearance Models

Color appearance models provide a tool to transform tristimulus values to perceptual attributes of color. Color perception algorithms developed for machine vision mostly rely on color appearance models (CAMs). The output of an ideal color appearance model should resemble human color perception in all conditions such as different adaptation, light levels and viewing conditions. However, a comprehensive mathematical model that is able to address all the underlying factors in human color perception would be very complex and computationally heavy. Moreover, color perception mechanisms of the human visual system have not yet been identified completely enough to be incorporated in that hypothetical ideal color appearance model.

There is an abundant number of models available for photopic conditions such as: the Hunt model [98], RLAB model [99], CIECAM97 [100] and CIECAM02 [101] models, most of which are described in [102]. Each of these models are based on some simplified assumptions and take limited factors underlying human color perception into account. A case in point is that most color appearance models do not incorporate the spatial or temporal properties of the visual system.

The *Bezold-Brücke effect* shows that hue perception depends on the luminance of the stimulus [86]. In other words, the hue of objects in the mesopic range will be different than in photopic conditions. At low light levels, two factors come into play as

compared with high light levels (photopic conditions): first, the signal to noise ratio decreases (either in the human visual system or in an artificial image sensor); and second, rods contribute to our vision[103]. Psychophysical evidence shows that cones and rods interact in the mesopic range [103]; however, the form of this interaction is controversial. Hence in mesopic vision, the photopic color appearance models will not work. Aside from the aforementioned limitations of photopic CAMs, there are only a few currently available color appearance models suited to the mesopic range, none of which perform well enough in terms of resembling human color perception. Moreover, these models are ad-hoc and non-physical fitting models to experimental data. Hunt proposed a color appearance model which considers rod responses [104]. Kwak, MacDonald, and Luo introduced a lightness predictor for mesopic vision to address the stimulus size effect in their model [105]. The other presented mesopic models are not CAMs since they do not take the viewing condition into account. We refer to them as *mesopic color vision models*. Hence, color vision models cover a greater number of models, which can be less general -in terms of considering visual appearance phenomena- and might have more limiting assumptions as compared with CAMs. Shin, Matsuki, Yaguchi, and Shioiri introduced a mesopic model based on psychophysical experiments on color patches [65]. Cao, Pokorny, Smith, and Zele proposed another mesopic vision model [71], which was employed in Kirk's perceptual tone mapping operator for low light conditions [95] and in the color retargeting approach proposed by Wanat and Mantiuk [2]. Rezagholizadeh and Clark proposed a maximum entropy-based spectral color vision model for mesopic conditions [8]. This work will be presented in Chapter 5. A comparison of four algorithms that

can realistically simulate the appearance of night scenes on a standard display is presented in [106]. In the following section, the challenges of studying mesopic vision will be briefly introduced.

2.4.1 Challenges of Mesopic Vision

As mentioned earlier, the human visual system may work in photopic, mesopic or scotopic modes and among them mesopic vision is much more complex than the other two. In this subsection, we briefly review the main challenges of mesopic vision.

According to [1], from physiological point of view, the main reasons behind this complexity are: first, rod-cone interactions; second, different rod and cone retinal spatial distributions; third, mixed spectral sensitivities of rods and cones; and fourth, changes in the spatial and temporal properties of the photoreceptor responses.

Mesopic photometry is one of the main existing challenges of mesopic vision. Scotopic photometry is obtained from the scotopic luminous efficiency function ($V'(\lambda)$), which is also known as the rod spectral sensitivity function. Since cones are not active in the scotopic region, the scotopic luminous efficiency function solely depends on the rod sensitivity function. A similar explanation can be given for photopic photometry, where only cones are responsible for luminance perception and the photopic luminous efficiency function can be determined as a linear combination of cone spectral sensitivities. In contrast to photopic and scotopic photometry, obtaining mesopic photometry is more challenging, because the mesopic luminous efficiency function should be determined by both cones and rods' spectral sensitivity functions and their interaction in mesopic vision. This interaction is not necessarily linear and depends on the light level. Hence, the mesopic luminous efficiency function should

be adaptively updated with the light level. Several photometry systems have been proposed in the literature [107, 108, 109, 110]; however, there is still no agreement on one. A CIE system for mesopic photometry has been recently recommended as a new model for the transition of the eye spectral sensitivity from the photopic to scotopic range as a function of luminance for mesopic conditions [111]. This mesopic photometry system is introduced in the next subsection.

The other challenges of mesopic vision are noise and uncertainty. In mesopic vision, the impact of noise (photon noise and dark current) on our visual perception becomes significant. Hence, mesopic vision comes with uncertainties due to the uncertain cone and rod photon counting. This uncertainty may lead to difficulties in color identification in the mesopic range as has been reported in some studies [70]. Hence, noise is a crucial part of mesopic vision modeling, though the number of models considering noise is rare [64].

To sum up, the mentioned factors make mesopic vision challenging, and detailed models of mesopic vision are to a high extent unknown. Hence, mesopic vision is still a hot research topic and the current mesopic color appearance models do not yet completely describe the human visual experience in the corresponding condition. In the next subsection, we will review the new CIE system for mesopic photometry.

2.4.1.1 CIE System for Mesopic Photometry

CIE has recently recommended a new photometry system for mesopic vision [111]. The new photometry system incorporates the transition of the eye spectral sensitivity from the scotopic luminous efficiency function $V'(\lambda)$ to photopic luminous efficiency function $V(\lambda)$ as a function of the photopic and scotopic luminance levels [111]. This

photometry system introduces a new formulation to derive the normalized mesopic eye spectral sensitivity, V_{mes}, and mesopic luminance, L_{mes}, as follows:

$$\begin{aligned} M(m)V_{mes}(\lambda) &= mV(\lambda) + (1-m)V'(\lambda) \quad 0 \leq m \leq 1 \\ L_{mes} &= \frac{683}{V_{mes}(\lambda_0)} \int_{\Lambda} V_{mes}(\lambda) L_e(\lambda) d\lambda \end{aligned} \tag{2.8}$$

where m is a mesopic measure varying in the range [0 1] ($m = 0$ corresponds to the fully scotopic and $m = 1$ corresponds to the fully photopic conditions); λ_0 is equal to 555 nm; L_e is the spectral radiance in $W.m^{-2}.sr^{-1}.nm^{-1}$; and, $M(m)$ is a normalizing function leading the maximum of V_{mes} to be equal to 1. Given the scotopic and photopic luminance values, the mesopic luminance can be calculated using the following iterative approach:

$$\begin{aligned} & m(0) = 0.5 \\ & L_{mes}(n) = \frac{m(n-1)L_p + (1 - m(n-1))L_s V'(\lambda_0)}{m(n-1) + (1 - m(n-1))V'(\lambda_0)} \\ & m(n) = 0.767 + 0.3334 \log(L_{mes}(n)) \quad 0 \leq m(n) \leq 1 \end{aligned} \tag{2.9}$$

where n indicates the iteration number, and $V'(\lambda_0) = 683/1699$.

2.4.2 Models

In this subsection, we discuss some of the well-known mesopic vision models currently available in the literature.

2.4.2.1 Hunt's Model for Mesopic Vision

Hunt proposed a complex color appearance model, which is one of the best-known and most complex color appearance models [104]. The Hunt model includes

different viewing components such as the stimulus, the background and the surroundings. In this section, we will briefly introduce how this model addresses mesopic vision in its formulation. This model requires the absolute luminance level of the reference white and adapting field, together with the scotopic luminance of the scene. Since the scotopic luminance data is usually unavailable, Hunt proposed a formula to predict this quantity according to the photopic luminance and the correlated color temperature of the illuminant as follows

$$L_{AS} = 2.26 L_A [(T/4000) - 0.4]^{1/3} \tag{2.10}$$

where L_{AS} is the scotopic luminance, L_A refers to the photopic luminance and T is the color temperature of the illuminant. In the Hunt model, rod responses are incorporated directly into the achromatic signal and then the achromatic signal is employed in obtaining other color correlates in the model such as chroma and hue. In this model, the rod responses are derived using the following formula:

$$\begin{aligned} A_S &= 3.05 B_S [f_n (F_{LS} S / S_w)] + 0.3 \\ f_n[I] &= 40[I^{0.73}/(I^{0.73} + 2)] \\ F_{LS} &= 3800 j^2 (5L_{AS}/2.26) + 0.2(1 - j^2) 4 (5L_{AS}/2.26)^{1/6} \\ j &= 0.00001/[(5L_{AS}/2.26) + 0.00001] \end{aligned} \tag{2.11}$$

where S and S_w correspond to the scotopic response of the stimulus and reference white, respectively; $f_n[I]$ represents the photoreceptor response function to the light level I; and f_{LS} is the scotopic luminance level adaptation factor.

The total achromatic signal, A, can be obtained by combining rod responses, A_S, and cone achromatic signals, A_a, as follows:

$$\begin{aligned} A &= N_{bb}[A_a - 1 + A_S - 0.3 + (1^2 + 0.3^2)^{1/2}] \\ A_a &= 2\rho_a + \gamma_a + (1/20)\beta_a 3.05 + 1 \end{aligned} \tag{2.12}$$

in which ρ_a, γ_a, and β_a represent the LMS responses in the Hunt model and N_{bb} refers to the brightness background induction factor. The above equations describe how the Hunt model involves rod responses in mesopic vision. This model is complex and the selection of its parameters is not straightforward.

2.4.2.2 Kwak's Lightness Prediction Model for Mesopic Vision

Kwak et al. proposed a new lightness predictor for mesopic vision based on the CIECAM02 lightness operator [105]. It is shown that the new operator improves the CIECAM02 to be able to better address the mesopic range. This lightness predictor, J_{s+p}, takes both cone and rod responses into account. Using the same notation as the Hunt model, the total achromatic signal in Kwak's model is calculated as a weighted summation of the cone's contribution to the achromatic response and the rode achromatic signal as follows:

$$\begin{aligned} A &= A_a + \alpha A_S \\ A_a &= 2R'_a + G'_a + 0.05B'_a - 0.305 \end{aligned} \tag{2.13}$$

where α is the weighting factor, A_S is derived from the Hunt model [104] as shown in eq. 2.11. (R'_a, G'_a, B'_a) are the adapted cone signals, which can be derived from the normalized cone responses (R', G', B'):

$$
\begin{aligned}
R'_a &= 400\frac{(F_L R'/100)^{0.42}}{(F_L R'/100)^{0.42}+27.3}+0.1 \\
F_L &= 0.2k^4(5L_A)+0.1(1-k^4)^2(5L_A)^{1/3} \\
k &= 1/(5L_A+1)
\end{aligned}
\tag{2.14}
$$

where L_A refers to the photopic luminance. Finally, the new lightness predictor is introduced in the following:

$$
\begin{aligned}
J_{s+p} &= 100(\frac{A}{A_w})^{\kappa z} \\
z &= 1.48+\sqrt{\frac{Y_b}{Y_w}}.
\end{aligned}
\tag{2.15}
$$

In the above equation, κ is the surround factor and the subscripts w and b refers to the reference white and background, respectively. This model has been claimed to be able to better describe the lightness dependent changes of hue and the Purkinje shift phenomenon in the mesopic range than the CIECAM02 model. However, this model does not consider any direct input from rod responses to the chromatic modelling of mesopic vision.

2.4.2.3 Modeling Blue Shift in Moonlit Scenes

The model proposed by Khan and Pattanaik [73] aims at addressing the *"Blue Shift"* in dark scenes. Recent findings show that rod cells contribute to off-bipolar cells during the scotopic condition by forming chemical synapses (gap junction). Based on this theory, to explain the blue shift, the authors hypothesize that these synapses are only established between rods and S cones. Then, they propose the following steps to derive the mesopic RGB response from the original image RGB

values (i.e. the image sensor measurements represented in the RGB color space).

1. Given the image RGB values, the scotopic luminance value, I_{rod}, is obtained when the adaptation intensity is set to 0.03 cd/m^2. However, this work does not give any particular model for obtaining the scotopic luminance from the RGB values.

2. For each pixel, the scotopic luminance is plugged in to the Hunt model [112] to derive the cone responses at the light intensity I and the rod responses R_{rod}.

3. In the scotopic condition, cone response values, R_l, R_m, and R_s, are assumed to be zero, since cone cells do not respond in the scotopic range.

4. The final mesopic simulated image is obtained by adding 20% of the rod response to the S-cone signal and then projecting the result back into the initial RGB space.

$$R_s = R_s + 0.2R_{rod} \tag{2.16}$$

The way the authors address the blue shift is by adding 20% of the rod response to the S-cone signals.

2.4.2.4 Cao's Model of Mesopic Vision

Cao et al. proposed a model for mesopic vision based on experiments they conducted [71]. The results of the experiments show that rod contributions to the PC, MC, and KC pathways linearly relate to rod contrast. The essence of the model, which is only valid for the mesopic range, is summarized in the following:

1. The image RGB values are transformed to the LMSR photoreceptor space which gives the cone and rod responses.

$$[E_L \; E_M \; E_S \; E_R]^t = M_E.[R \; G \; B]^t \tag{2.17}$$

Table 2–2: The parameters of the Cao model for mesopic vision [2]

Y $[cd/m^2]$	$\kappa_1(Y)$	$\kappa_2(Y)$
10	0	0
0.62	0.0173	0.0101
0.10	0.173	0.357

where M_E is the corresponding transformation matrix.

2. Since rods and cones share their pathway to the visual cortex, rod responses can be combined with the cone responses according to the following equation:

$$\begin{bmatrix} L \\ M \\ S \end{bmatrix} = \begin{bmatrix} 1 & 0 & 0 & \kappa_1(Y) \\ 0 & 1 & 0 & \kappa_1(Y) \\ 0 & 0 & 1 & \kappa_2(Y) \end{bmatrix} \begin{bmatrix} E_L \\ E_M \\ E_S \\ E_R \end{bmatrix} = M_c(Y) \begin{bmatrix} E_L \\ E_M \\ E_S \\ E_R \end{bmatrix}. \tag{2.18}$$

The coefficients $\kappa_1(Y)$ and $\kappa_2(Y)$ are derived by interpolation from the experimental measurements done by Cao et al. with respect to the original scene's luminance level, Y (see table 2–2).

2.4.2.5 Shin's Color Appearance Model for Mesopic Vision

Shin et al. proposed a modified version of the Boynton two-stage model [113] with fitting parameters to account for the rod intrusion in mesopic vision [65]. The parameters of the model are obtained as a function of illuminance based on the asymmetric color matching experimental data. In their experiment, the observer is presented with a Munsell color chip under the mesopic condition and is asked to

match the appearance of that patch with a simulated image, reproduced by this model in the CRT display under the photopic condition. The model takes in the cone responses after adaptation and outputs achromatic, red/green, and blue/yellow opponent responses. This model is described in greater detail in Chapter 5.

2.5 Advanced Image Rendering Techniques for Mesopic Vision

2.5.1 Perceptual Tone Mapping Operators for Mesopic Vision

Handling high dynamic range scenes is challenging for cameras. Capturing high dynamic range scenes might introduce over/under-exposed regions into the output image. One way to avoid this problem was introduced by Debevec and Malik [114] who suggest imaging with multiple exposures and combining them. Currently available CCD or CMOS image sensors are capable of capturing a wide range of luminance values; however, most existing displays are not able to display more than two orders of magnitude. Tone mapping is an approach for solving this problem of mapping the high dynamic range image intensities to the low dynamic range display outputs to have the reproduced image perceptually closer to the original scene.

Applying a tone mapping operator to an image may cause changes to the color appearance of the original image [115, 116]. To address the color changes, a color correction method should be applied to the tone-mapped image. Pouli et al. propose a color correction technique in which the image is transformed into the IPT space and then the ICH space [116]. To find the color corrected image, the lightness component of the tone-mapped image is combined with the hue of the original image and the corrected chroma factor, which is introduced in [116]. However, the color correction approaches are not perceptual, they are not powerful enough to take

viewing conditions into account, and they can not address mesopic induced effects on the color appearance of images.

Reinhard states that "tone mapping techniques and color appearance models are two sides of the same coin" [39]. In other words, even though tone mapping operators and color appearance models are supposed to solve the same problem, they are currently very divergent. On the CAM side, many models are available such as: the Hunt model, the RLAB model, and the CIECAM97 and CIECAM02 models, most of which are described in [102]. However, none of them are appropriate to be used in tone mapping algorithms, and among them, models that focus on mesopic vision appearance are few. We can say that tone mapping techniques suffer from a lack of a suitable color appearance model for mesopic vision.

From the tone mapping point of view, several perceptual tone mapping operators have been proposed, including the multi-scale model by Pattanaik, Ferwerda, Fairchild, and Greenberg [117], the perceptually-based tone mapping by Irawan, Ferwerda, and Marschner [118], and the iCAM06 tone reproduction technique [119]. A complete review of the available tone mapping operators can be found in [66]. In the remainder of this subsection, we review the existing tone reproduction (also known as tone mapping) operators which take the mesopic range into account.

Pattanaik et al. developed a model of adaptation and spatial vision based on a multiscale representation of the human visual system, color processing, as well as luminance [117]. This model accounts for a wide range of changes, such as visual acuity, colorfulness, and apparent contrast, which varies with illumination. Ferwerda, Pattanaik, Shirley, and Greenberg proposed a model for visual adaptation in which

different human visual system phenomena such as threshold visibility, visual acuity, temporal adaptation, and color correction are involved [93]. Durand and Dorsey extended the Ferwerda tone mapping operator by adding a blue shift mechanism to address the mesopic color appearance of night scenes [120]. This blue shift operator is built on the Hunt data, which shows that white preference changes in very dark conditions toward the normalized $RGB = [1.05, 0.97, 1.27]$. However, this model oversimplifies the complex mesopic vision mechanisms. Krawczyk, Myszkowski, and Seidel introduced a local contrast compression technique in which they included some perceptual phenomena related to mesopic vision such as changes in visual acuity and rod contributions to mesopic vision [121]. Mikamo, Slomp, Tamaki, and Kaneda decoupled the luminance component from the chromatic content of the image and then discounted the red content of the image in the CIE LAB color space depending on the average luminance level of the image [122]. Two of the most recent and well-known perceptual tone mappers are reviewed in greater detail in the following.

2.5.1.1 iCAM06 Tone Compression Model for Mesopic Vision

This approach is one of the best-known image appearance methods in the literature. The iCAM06 tone mapping technique accounts for the mesopic condition by including the rod response in its tone compression operator [119], which is summarized as follows.

1. The chromatic adapted image is input to the tone compression unit. First, the image is converted to the Hunt-Pointer-Estevez color space. Then, the cone responses (R'_a, G'_a, B'_a) are obtained using the cone response functions introduced by

Hunt [112] from the (R', G', B') inputs from the previous step.

$$
\begin{aligned}
R'_a &= \frac{400(F_L R'/Y_w)^p}{27.13 + (F_L R'/Y_w)^p} + 0.1 \\
G'_a &= \frac{400(F_L G'/Y_w)^p}{27.13 + (F_L G'/Y_w)^p} + 0.1 \\
B'_a &= \frac{400(F_L G'/Y_w)^p}{27.13 + (F_L G'/Y_w)^p} + 0.1 \\
F_L &= 0.2k^4(5L_A) + 0.1(1 - K^4)^2(5L_A)^{1/3} \\
k &= 1/(5L_A + 1)
\end{aligned}
\tag{2.19}
$$

where Y_w refers to the luminance of the local adapted white image, p is a user adjustable parameter (which determines the steepness of the photoreceptor responses) and L_A is the adaptation luminance.

2. The adapted rod response (A_S) is calculated using the Hunt model [112].

$$
\begin{aligned}
A_s &= 3.05B_s[\frac{400(F_{LS}S/S_w)^p}{27.13 + (F_{LS}S/S_w)^p}] + 0.3 \\
F_{LS} &= 3800j^2(5L_{AS}/2.26) \\
&+ 0.2(1 - j^2)^4(5L_{AS}/2.26)^{1/6} \\
L_{AS} &= 2.26L_A \\
j &= 0.00001/[(5L_{AS}/2.26) + 0.00001] \\
B_S &= \frac{0.5}{1 + 0.3[(5L_{AS}/2.26)(S/S_w)]^{0.3}} \\
&+ \frac{0.5}{1 + 5[5L_{AS}/2.26]}
\end{aligned}
\tag{2.20}
$$

where S and S_w are the luminance of the chromatic adapted image and that of the

reference white, respectively, and L_{AS} is the scotopic luminance value.

3. The tone compression output (RGB_{TC}) is computed as a linear combination of the cone responses (RGB'_a) and the rod response (A_S).

$$RGB_{TC} = RGB'_a + A_s \tag{2.21}$$

It is assumed that rod cells contribute to all cone responses with the same weights; however, this is questionable based on the recent findings [95].

2.5.1.2 A Perceptual Tone Mapping of Mesopic Vision based on the Cao Model

Kirk and O'Brien established a perceptually-based tone mapping method accounting for mesopic conditions based on the Cao model [95]. The Cao model can be summarized in three fundamental steps (we keep the same notations as [95]).

1. Rod responses are involved in setting three regulators: g_L, g_M, and g_S.

$$\begin{aligned} g_L &= 1/(1 + 0.33(q_L + \kappa_1 q_{rod}))^2 \\ g_M &= 1/(1 + 0.33(q_M + \kappa_1 q_{rod}))^2 \\ g_S &= 1/(1 + 0.33(q_S + \kappa_2 q_{rod}))^2 \end{aligned} \tag{2.22}$$

where κ_1 is a coefficient which adjusts the correct proportion of the rod to cone response, q_i, $i \in \{L, S, M\}$ represent the cone responses, and q_{rod} indicates rod responses. These three regulators will determine the amount of the color shift in the opponent color model.

2. Regulators and rod responses determine the amount of shift in each opponent

channel using the following formulas:

$$\begin{aligned}
\Delta o_{R/G} &= x\kappa_1(\rho_1\frac{g_M}{m_{max}} - \rho_2\frac{g_L}{l_{max}})q_{rod} \\
\Delta o_{B/Y} &= y(\rho_3\frac{g_S}{s_max} - \rho_4 W)q_{rod} \\
\Delta o_{Luminance} &= zWq_{rod} \\
W &= (\alpha\frac{g_L}{l_{max}} + (1-\alpha)\frac{g_M}{m_{max}})
\end{aligned} \tag{2.23}$$

where x, y, and z are free tuning coefficients; $l_{max} = 0.637$, $m_{max} = 0.392$, and $s_{max} = 1.606$ are the maximum values of cone fundamentals [95]; and ρ and α are fitting parameters set as: $\rho_1 = 1.111$, $\rho_2 = 0.939$, $\rho_3 = 0.4$, $\rho_4 = 0.15$ and $\alpha = 0.619$. W is a positive value which can be used as a measure of mesopic level, where $W = 0$ indicates the fully photopic condition. It is worth mentioning that the color shifts are nonlinear functions of the g_is but linear functions of rod response.

3. The shifted cone responses which account for mesopic color appearance effects are introduced as a linear combination of the cone responses and the calculated color opponent shift components.

$$\begin{aligned}
\hat{q} &= [q_L\ q_M\ q_S]^T + \Delta\hat{q} \\
\Delta\hat{q} &= A^{-1}\Delta o
\end{aligned} \tag{2.24}$$

where A is the transformation matrix between the opponent color space and the corresponding shifted cone response.

$$\begin{aligned}
o_{R/G} &= \hat{q}_M - \hat{q}_L \\
o_{B/Y} &= \hat{q}_S - (\hat{q}_L + \hat{q}_M) \\
o_{Luminance} &= \hat{q}_L + \hat{q}_M
\end{aligned} \tag{2.25}$$

2.5.2 Color Retargeting Approaches for Mesopic Vision

A typical image processing chain is comprised of a scene, a camera which takes a picture of the scene, a display which shows the taken picture and a human observer. The ultimate goal of the display technology is to reproduce the image on the display such that it visually matches the original scene for the human observer [123]. To achieve this goal, the display technology needs to be able to physically reproduce real-world scenes with high dynamic range and different brightness levels (hardware improvement); on the other hand, visual system mechanisms such as contrast, luminance and color perception have to be taken into account in display rendering units (software improvement) [93, 83]. For example, the minimum brightness level of traditional displays was so high that we could only reproduce images in photopic conditions; however, the new OLED technology can go as dim as 2 cd/m^2, which is in the mesopic range, and now we can think of reproducing photopic images on mesopic displays as well. Hence, to have perceptual displays, it is vital to know human color perception mechanisms and to be able to model them. The model should be comprehensive enough to take into account all aspects of human color vision in all visual conditions such as different light levels [124].

Color appearance models aim at reproducing color perceptual attributes of a simple stimulus as the human visual system perceives them. Therefore, by definition, color appearance models should be very useful in achieving perceptual displays. However, most color appearance models are valid only under certain limited conditions: first, most of them do not take spatial and temporal properties of the human visual system into account; second, they model the appearance of simple stimuli such

as color patches [125]; third, they are developed for photopic conditions [126, 69]; and, fourth, they assume pixels are independent from each other [127].

Image color appearance models (iCAMs) are proposed to fill this gap by incorporating the spatial and temporal vision to model the appearance of complex stimuli [119]. But even these models do not work well in the mesopic range. A case in point is the iCAM06 model proposed by Kuang, Johnson, and Fairchild [119], in which the rod contributions are added to the cone responses uniformly. However, recent studies show that the rod contributions to different channels are not the same [71, 128]. Hence, the model used for mesopic vision in image appearance models should be improved. Moreover, existing iCAMs and CAMs are only able to *simulate* (i.e. predict the appearance of the original scene as a human observer perceives) the appearance of stimuli. They are not designed to *compensate* for (i.e. reproduce colors on a rendering medium with a specific viewing condition to match the original scene colors) appearance changes of stimuli rendered on different mediums with different viewing conditions. For example, when a bright scene is reproduced on a dim display, the contrast degradation and the hue and saturation shift due to mesopic vision will heavily affect the visual appearance of the image content. In this case, a compensation algorithm should be employed to retrieve the original image's appearance.

An *image retargeting* technique aims to provide a unified framework for both the simulation and compensation algorithms, and it can be thought of as a bidirectional image color appearance model. Wanat and Mantiuk proposed a retargeting method which consisted of global and local contrast retargeting units together with a color

retargeting block [2]. A perceptual color retargeting method employs a color appearance model (responsible for predicting the color of the original scene) for simulation purposes and its inverse for compensation purposes. Since, in theory, the scene and rendering device luminance can be in any of the three photopic, mesopic, or scotopic ranges, the color appearance model should be viable for all luminance levels as well. However, as was mentioned in the preceding sections the number of models considering the mesopic and scotopic range and rod contributions is small [8, 69].

We only have a handful of color retargeting methods and none of them perform very well in simulating and compensating images in dark conditions. An eligible color vision model for perceptual color retargeting algorithms should possess two main features: first, the model must be applicable to the entire luminance range of the human visual system (photopic, mesopic and scotopic vision); and second, the model must be invertible. We can add a third condition, which is that the model must be computationally inexpensive, if the algorithm is going to be used in real time applications. Taking these three conditions into account, only the Cao and Shin model would be qualified to be deployed in a color retargeting framework. The Cao model, however, has shown a poor performance in reproducing colors in mesopic conditions over both color patches [8] and complex stimuli [2]. This is mainly due to the linearity assumption made in Cao's model between the color and the illuminance, which oversimplifies the color mechanisms of the human visual system. Two of the existing color retargeting methods are reviewed in the following.

2.5.2.1 The Wanat Color Retargeting Approach based on the Cao Mesopic Model

The luminance retargeting method proposed by Wanat and Mantiuk [2] consists of tone-curve optimization, spatial contrast processing, and color retargeting. In this work, the inverse of the Cao mesopic model, which is introduced in 2.5.1.2, is developed and employed in the color retargeting method [2] and summarized in the following:

1. The image RGB values are transformed to the LMSR photoreceptor space which gives the cone and rod responses.

$$[E_L \; E_M \; E_S \; E_R]^t = M_E.[R \; G \; B]^t \tag{2.26}$$

where M_E is the corresponding transformation matrix.

2. Since rods and cones share their pathway to the visual cortex, the photoreceptor responses are combined according to the following equation:

$$\begin{bmatrix} L \\ M \\ S \end{bmatrix} = \begin{bmatrix} 1 & 0 & 0 & \kappa_1(Y) \\ 0 & 1 & 0 & \kappa_1(Y) \\ 0 & 0 & 1 & \kappa_2(Y) \end{bmatrix} \begin{bmatrix} E_L \\ E_M \\ E_S \\ E_R \end{bmatrix} = M_c(Y) \begin{bmatrix} E_L \\ E_M \\ E_S \\ E_R \end{bmatrix}. \tag{2.27}$$

The coefficients $\kappa_1(Y)$ and $\kappa_2(Y)$ are introduced in 2.5.1.2.

3. The result of retargeting for a new target luminance value $\tilde{Y}$ can be obtained by:

$$\begin{bmatrix} \tilde{R} \\ \tilde{G} \\ \tilde{B} \end{bmatrix} = \frac{\tilde{Y}}{Y}(M_c(\tilde{Y})M_E)^{-1}M_c(Y)M_E \begin{bmatrix} R \\ G \\ B \end{bmatrix} \tag{2.28}$$

2.5.2.2 The Wanat Color Retargeting Approach based on the Color Saturation Function

In [2], Wanat and Mantiuk proposed a complete Cao-based color retargeting algorithm; however, they reported that the performance of this method was unsatisfactory and ended up using a simple color correction formula according to the image and the target luminance. The color retargeting model of this method is as follows:

$$\begin{aligned} \hat{R}_i &= \tilde{Y} \times (\frac{\tilde{R}_i}{\tilde{Y}})^{\frac{s(Y)}{s(\tilde{Y})}} \\ s(Y) &= \frac{Y}{(Y+\kappa)} \end{aligned} \tag{2.29}$$

where Y and $\tilde{Y}$ are the image luminance and the luminance of the tone-mapped image, respectively, κ is an adjusting factor and $\tilde{R}_i$ refers to the i_{th} channel of the tone-mapped image.

While their tone mapping algorithm showed improved performance compared to many other methods [2], the color retargeting method did not show a significant contribution for image reproduction in the mesopic range [7].

2.6 Concluding Remark

Development of a realistic color appearance model based on the human visual system functionality which addresses the issue of noise under low luminance levels is an ongoing problem in color science. Future studies toward developing more realistic mesopic and scotopic models need to extract the basic principles governing the probabilistic nature of the visual perception at low light levels and incorporate them in the models. Achieving this goal will facilitate the attainment of other objectives of primary concern in machine vision research e.g. developing image quality measures, introducing efficient denoising algorithms, developing realistic color noise perception models, addressing mesopic and scotopic conditions in current digital cameras and developing new tone mapping algorithms for rendering color images that can be perceived more naturally.

CHAPTER 3
At Night: Photon Detection in the Scotopic Range

According to the de Vries-Rose law, the impact of the probabilistic nature of photon emission on the contrast sensitivity of the human visual system becomes more significant at low light levels [74]. This chapter aims to investigate the impact of photon noise and light level on cone responses close to the absolute threshold of the visual system (scotopic range) assuming that cones are ideal photodetectors without any internal noise. In this regard, physical principles are leveraged to develop a framework for estimating low light spectra at any arbitrary level from their high intensity spectral power distributions.

The results of this study show that close to the absolute threshold of the visual system, the chromaticity representation of ideal cone responses (to a color patch viewed over time) spread around the chromaticity of the high intensity patch; and the distribution of these chromaticities are mainly confined to an elliptical region in the xy-chromaticity diagram. The size of these ellipses changes as a function of the light intensity and chromaticity of the high intensity color patches. The orientation of the ellipses depends only on the patch chromaticity and not on the light level. Moreover, the results of this chapter indicate that the spectral composition of light is a determining factor in the size and orientation of the ellipses.

3.1 Preliminaries: Physical Aspects of Photons (Photon Emission)

Einstein and Planck hypothesized that photons carry an exact amount of energy specified by the frequency of the quantum. The energy of the electromagnetic field with frequency ω is an integer multiple of $h\omega$ [129]. The word, "photon" was coined by Lewis in 1926. Photons are the particles that constitute light and each photon is characterized by two values: frequency and polarization state. The frequency of photons may be changed using a separate controlled manipulation process [129]; however, the frequency of photons remains unchanged under interaction with matter [130]. Photon emission follows a Poisson distribution and the probability of emitting n photons per unit time by a monochromatic light source with a wavelength λ and an average emission rate of x is given by [86]:

$$P(x, n) = \frac{x^n \ e^{-x}}{n!}. \tag{3.1}$$

For an arbitrary stimulus with a spectral power distribution $S(\lambda)$, the probability of emitting k photons for each wavelength can be obtained by [86]:

$$\begin{aligned} P(x(\lambda_0), k) &= \frac{e^{-x(\lambda_0)} x(\lambda_0)^k}{k!} \\ x(\lambda_0) &= \frac{Ft}{hc} \int_{\lambda_0}^{\lambda_0+\delta\lambda} \lambda S(\lambda) \ d\lambda \end{aligned} \tag{3.2}$$

where x denotes the average number of photons (of particular wavelength λ_0) emitted per unit time, F is the power of light in watts, t is the integration time (i.e. the sampling time of the photo-detector) in seconds, $c = 2.997925 \times 10^8 (m.s^{-1})$, and Planck's constant $h = 6.626176 \times 10^{-34}$ $(J.s)$.

3.2 Preliminaries: Biophysical Aspects of Photons (Photon Absorption)

In this subsection, we will briefly review what is happening from the moment photons reach the cornea until they are absorbed by the photoreceptors. Assume that a group of photons reach the cornea and pass through the lens. Some of the photons (especially those in the ultra-violet region) are absorbed by the pigment molecules within the lens and the rest take the path to the retina through the watery gel called *vitreous*. Cone and rod photoreceptor cells are spread over the retina in a non-uniform pattern. Cones are concentrated in the fovea, a small spot around the center of the retina containing no rods. Away from the fovea, rods are the dominant photoreceptors, and the rod to cone ratio is about 30:1. Photons falling on the retina will be captured by a photoreceptor depending on the wavelength and the photoreceptor type [130]. The direction of arrival is another important determining factor in photon absorption, especially for cones; however, this factor is beyond the scope of this research. Different photoreceptor types exhibit different sensitivities to photons with various wavelengths. For instance, L cones are more sensitive to photons of longer wavelengths, while S cones are more sensitive to short wavelengths. The wavelength dependency and photoreceptor type can be incorporated in deriving the mean photon absorption rate, x, as follows

$$x = \frac{tF}{hc} \int \lambda S(\lambda) \rho_i(\lambda) \; d\lambda \qquad i = \{L, M, S, Rod\} \tag{3.3}$$

where $\rho_i(\lambda)$ indicates the spectral sensitivity of a photoreceptor of type i; $[F \times S(\lambda)]$ is the spectral radiant power distribution and $[S(\lambda)]$ defines the relative spectral

radiant power distribution. In the marginal case (i.e. for a monochromatic stimulus), $S(\lambda) = \delta(\lambda - \lambda_0)$ and $\rho_i(\lambda_0) = \rho = constant$.

3.3 Methods: How Does Spectral Power Distribution Change with Intensity?

This section introduces a model to obtain an estimate for the low intensity spectral power distribution of light from its corresponding high intensity spectral power distribution. The spectral power distribution of light is usually measured at high intensities and this measured spectrum can not be extended (or trusted) to other intensities without modification.

To begin with, the photon emission rate in successive time intervals is a Poisson random process, which is given by Equation 3.2. This equation is written in the continuous form; however, since we usually deal with the discrete version of spectral power distributions, we can convert it to the discrete form as follows:

$$S_d(\lambda) = \sum_{i=1}^{N} s_i \delta(\lambda - \lambda_i) \tag{3.4}$$

where $s_i = S_d(\lambda_i)$ and the λ_is specify the wavelength samples in the discrete spectral power distribution. Bear in mind that $\sum_{i=1}^{N} s_i \Delta\lambda_i = 1$. If we assume uniform sampling, then $\Delta\lambda_i = \lambda_i - \lambda_{i-1}$ is constant along the distribution.

In the remainder of this section, we introduce a spectral power distribution simulator based on the light intensity level. In this regard, we assume that we are given the spectral power distribution of a light source at a high intensity (S_d^h) and want to derive the power spectral distribution under other intensities (S_d^e). It is worth

mentioning that the intensity of the spectral power distribution might be changed by altering the power of the light source.

The following equations reveal how the estimated spectrum at an arbitrary intensity level can be derived given the high intensity spectrum power distribution (S_d^h). We consider the high intensity spectral power distribution to be the most reliable descriptor of the light source (i.e. the high intensity spectral power distribution shows negligible fluctuation, compared to the absolute number of emitted photons, during the measurement time.) So, we can obtain the estimated average photon number per unit time, $x^e(\lambda|S_d^h)$, emitted by the light source with the given power of F' as follows:

$$\begin{aligned} x^e(\lambda_i|S_d^h) &= \frac{F't}{hc}(s_i^h \lambda_i \Delta(\lambda_i)) \\ \text{subject to: } & \sum_{i=1}^{N} s_i^h \Delta\lambda_i = 1 \end{aligned} \tag{3.5}$$

where the superscript ^{e} in the equations indicates the estimated variable for low intensity conditions. However, these equations are general and can be used for the purpose of estimating the high intensity spectral power distribution as well, even though the estimated spectral power distribution will be close to the S_d^h. Then, the probability of emitting k photons per unit time by the light source in the low intensity condition is given by:

$$P(x^e(\lambda_i|S_d^h), k) = \frac{e^{-x^e(\lambda_i|S_d^h)} x^e(\lambda_i|S_d^h)^k}{k!}. \tag{3.6}$$

The term $x^e(\lambda_i|S_d^h)$ can be obtained for varying source power (F'). Given the distribution function ($P(x^e(\lambda_0), k)$) a set of samples $[X(\lambda_i)]_1^N$ are drawn for the entire

wavelength range and the estimated spectral power distribution can be derived as follows

$$S_d^e(\lambda_i) = \frac{\frac{X(\lambda_i)hc}{\lambda_i}}{\sum_{j=1}^{N} \frac{X(\lambda_j)hc}{\lambda_j \Delta\lambda_j}} = \frac{X(\lambda_i)}{\lambda_i \sum_{j=1}^{N} \frac{X(\lambda_j)}{\lambda_j \Delta\lambda_j}}. \tag{3.7}$$

The final step in getting the power distribution function is to compute the energy of each sample and normalize all such that $\sum_{i=1}^{N} s_i^e \Delta\lambda_i = 1$.

It is worth mentioning that if you change the bin size (i.e. the size of $\Delta\lambda_i$), the accuracy and resolution of the estimated spectrum will be changed (the smaller bin size will give a higher accuracy). Hence, it is up to the user to determine the bin size according to their required precision. The difference between the high intensity spectral power distribution and the estimated low intensity one can be obtained as follows:

$$D = \sqrt{\Delta\lambda \sum_{i=1}^{N} (S_d^e(\lambda) - S_d^h(\lambda))^2}. \tag{3.8}$$

A sample calculation of the estimated spectral power distribution for different light intensities of an arbitrary high intensity spectral power distribution is shown in Figure 3–1. The parameters of the calculation are set as $t = 0.2s$, $\Delta\lambda = 5nm$, and F is depicted at the top of each sub-figure. Figure 3–2 shows the difference between the estimated spectral power distribution (SPD) and the high intensity SPD in terms of the formula for Euclidean distance between the distributions given in Eq. (3.8).

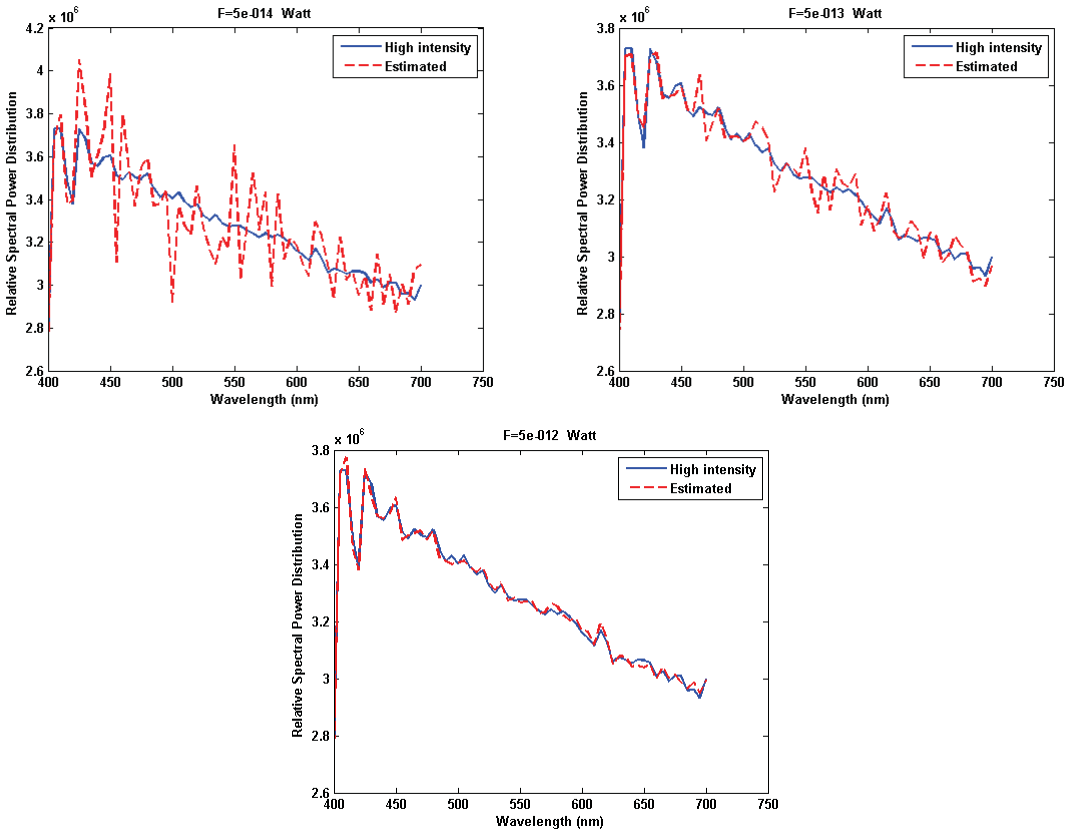

Figure 3–1: The estimated spectral power distribution of a light source with an arbitrary spectral power distribution using Equation 3.7 at different intensities. (t=0.2 sec and $\Delta\lambda = 5nm$).

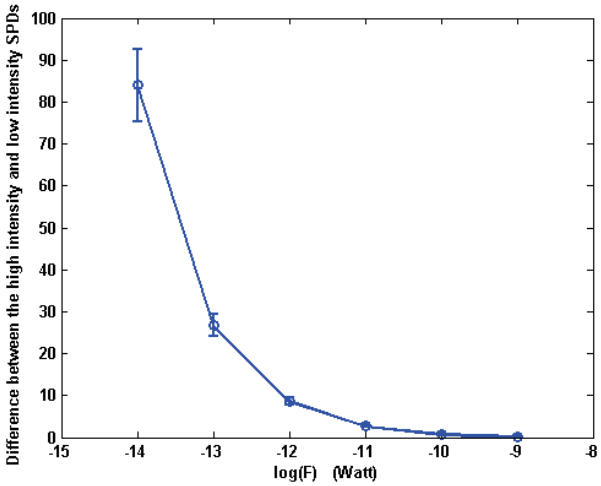

Figure 3–2: The difference between the estimated spectral power distribution (SPD) and the high intensity SPD in terms of the Euclidean distance between distributions. Error bars show the standard deviation of this difference measure in different trials. The parameters set are the same as in Figure 3–1.

3.4 Results and Discussion

3.4.1 Scenario I: How photoreceptor responses vary under different luminance levels

In the following, we consider a case in which it is assumed that cones are ideal i.e. cones do not have any internal noise in their responses in very dim light conditions. It is investigated how cones would respond in such conditions. In this regard, several light intensities are examined for a given spectral power distribution in Fig. 3–1 and for each one the estimated spectral power distribution of light (see Eq. 3.7) is used to obtain cone responses as follows:

$$R_i = \int S_d^e(\lambda)\rho_i(\lambda)d\lambda \qquad i = 1, 2, 3 \tag{3.9}$$

Hence, we use the estimated spectral power distribution under different intensities and calculate the cone responses assuming that cones are ideal photodetectors. Subsequently, we can investigate how the chromaticity representation of the cone responses to a given stimulus may change with the light intensity. We keep the situation the same as the estimated spectral power distributions in Fig. 3–1. R_i in Eq. (3.9) is the i^{th} element of the cone response vector R, and can be transformed to the XYZ space using a linear transformation as follows:

$$R_{XYZ} = MR \tag{3.10}$$

For each intensity level, 100 spectral power distribution samples are drawn; then, the chromaticity of color for each sample is obtained from the XYZ coordinates and shown in a chromaticity diagram (see Fig. 3–3(a)). In this subfigure, the lowest area ellipse surrounding all the samples of the same intensity and centered at the chromaticity of the highest intensity sample is plotted for each intensity level. The last step is dedicated to obtaining color differences between trials of the low intensity estimation and the high intensity response, in which the spectral power distribution fluctuation is negligible, using the following formula.

$$\begin{aligned} E_{xy}(i,j) &= \sqrt{{\Delta x_{ij}^c}^2 + {\Delta y_{ij}^c}^2} \\ \Delta x_{ij}^c &= x_i^c(F_j) - x^c(F_h) \\ \Delta y_{ij}^c &= y_i^c(F_j) - y^c(F_h) \end{aligned} \tag{3.11}$$

To avoid confusion with the Poisson distribution factor x, which was introduced earlier, we name the chromaticity coordinates as x^c and y^c. In Eq. (3.11), $x_i^c(F_j)$

and $y_i^c(F_j)$ refer to the chromaticity coordinates of the i^{th} sample of the j^{th} intensity. Similarly, $x^c(F_h)$ and $y^c(F_h)$ refer to the chromaticity coordinates of the high intensity response. To derive a single measure of chromaticity difference for each intensity, the mean of $E_{xy}(i,j)$ over all trials of each intensity is obtained.

$$\overline{E_{xy}} = \frac{1}{T}\sum_{i=1}^{T} E_{xy}(i,j) \tag{3.12}$$

The result of this computation is shown in Fig. 3–3 (b). Error bars for each intensity in this figure indicate the standard deviation of chromaticity differences for the samples of each intensity. Acknowledging our previous discussion, this figure shows that the mean chromaticity difference and its standard deviation (i.e. fluctuations among trials of each intensity) decrease as light intensity increases. We wrap up

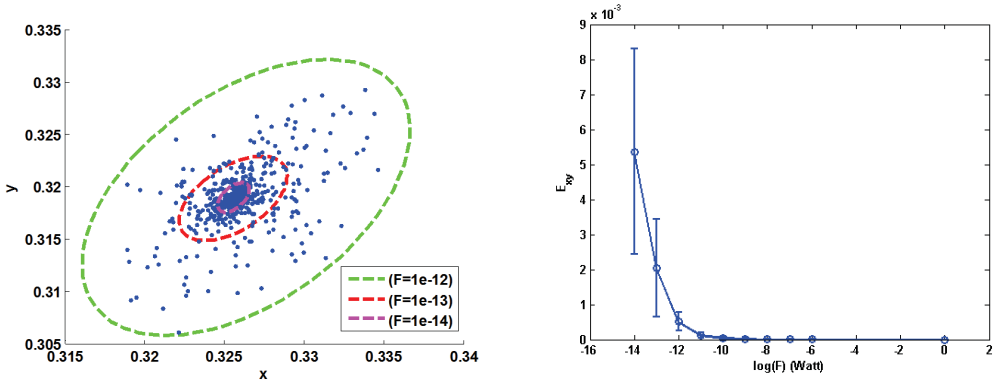

(a) (b)

Figure 3–3: (a) Chromaticity diagram for different trials (each color represents a single intensity of light). At each intensity, the smallest ellipse which encloses all the corresponding samples of that intensity is depicted. The distance between the consecutive ellipses falls off as light intensity increases, implying that as intensity reduces fluctuations become more and more severe. (b) The mean chromaticity difference between trials of the same intensity and the high intensity chromaticity.

this subsection by pointing out some remarks: first, in the implementation of this scenario, we did not take into account the dark noise effect; second, the discussion can be extended to other imaging systems like digital cameras (see Chapter 4); and third, for the sake of argument, we did not assume any internal noise for cones and it is shown that cone responses become more uncertain in scotopic conditions, not due to the limits imposed by the sensory system, but due to the physical limits introduced by the light source and the large fluctuations that appear in the photon stream in such conditions.

3.4.2 Scenario II: Photon Detection and MacAdam Ellipses

MacAdam published the results of his color matching experiment, which was done in different points of the chromaticity space in 1942 [131]. The experiment was performed with a constant luminance of about 48 cd/m^2, which is considered as photopic luminance. The target and test stimuli were created by the same set of red, green, and blue primaries. The experiment consisted of multiple levels, within which 25 different central chromaticities were examined, and each level was associated with a certain central chromaticity. At each level, the chromaticity of the test stimulus was fixed at a central point and the chromaticity of the target could vary along intersecting lines passing through the same selected central point. The observer (PGN) could adjust the color of the test stimulus by turning a knob. The standard deviations of different adjustments along different directions for each single central chromaticity were determined and related to the just noticeable color differences. For each central point in the chromaticity space, the standard deviations (SD) corresponding to all the lines along which the color of the test stimulus were changing

were plotted and an ellipse was fit to the SD points. Ellipses obtained in this way are known as MacAdam ellipses. This work and further developments of this study were used as a basis for color discrimination investigation and development of line elements inside the chromaticity space.

It is worth mentioning that a uniform chromaticity-scale surface and some color difference formulae have been proposed based on McAdam ellipses; however, none of them received much interest in color science and they are not being used today. Moreover, MacAdam ellipses in 1942 were derived based on acquisition of the data from only one subject and later from two subjects in 1949. Hence, the results are subject to change when dealing with a broader range of observers. Last but not least, MacAdam ellipses represent the indistinguishable colors in the chromaticity space. These ellipses were constructed under photopic conditions and they should be extended to be appropriate for low light conditions.

Here, we are going to examine the similarity between the results of our test and McAdam‘s ellipses. In the following, a test similar to that of the previous scenario is done over several chromaticity values. These chromaticities are reproduced under different light levels considering the physical principles stemming from the Poisson distribution governing the photon emission. Two spectral databases: Munsell color patches, and the Metacow spectral database are selected to generate the cone responses and their corresponding chromaticity representations within the xy-chromaticity diagram. For each spectral power distribution, a number of cone responses are generated over different light intensities and these samples are plotted in the chromaticity diagram. In the next step, the PCA algorithm is exploited to find

Table 3–1: The list of used Munsell color patches

Hue	Value	Chroma
10 GY	60	10
5 Y	50	4
7.5 YR	50	8
10 R	60	10
10 RP	40	10
2.5 P	60	8
5 PB	40	10
5 B	50	6
7.5 BG	70	6
5 G	70	8

principal vectors along which chromaticity sample points are spread. This procedure determines the orientation and size of data variance. The result of this test over each database is reported in the following.

3.4.2.1 Munsell Database

Cone responses are obtained for a set of chosen Munsell patches based on their given spectral reflectance function and assuming an equi-energy light source. These color patches are selected according to Shin's suggestion in [65] to cover various hue angles. The list of these Munsell color patches used for our test is shown in Table 3–1. The values and notation for the listed Munsell coordinates come from the Munsell book of color.

3.4.2.2 MetaCow Database

The MetaCow spectral database is a (4200×6000) pixel synthesized spectral image sampled in 5 nm increments from 380 to 760 nm. The chromaticities spanned

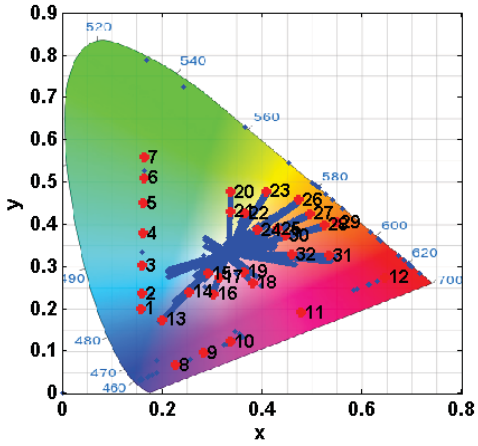

(a)

Figure 3–4: The chromaticity values spanned by the MetaCow spectral database are indicated by blue dots. The selected points for the experiment are marked as red asterisks with designated numeric indices.

by the spectral image are shown in the chromaticity diagram in Fig. 3–4 and among these points, 32 are selected for the sake of our experiment.

The power of the light source varies in the range of $[1 \times 10^{0}$,$6 \times 10^{-15}]$ watts and for each light intensity 200 samples are generated. Sample sets are formed by including samples generated from the highest intensity $F = 1W$ to a selected minimum intensity for each set (such as $F = 6 \times 10^{-15}$ watts). In this way, four sets with low intensities: $10^{-12}, 10^{-13}, 10^{-14}$, and$6 \times 10^{-15}$ watts are produced for each database. The results of the experiment for the biggest sample set (which includes all generated samples) of the Munsell and MetaCow datasets are shown in Figs. 3–5 and 3–7, respectively. As these figures indicate, the chromaticity representation of the cone responses generated for each color patch in the xy-chromaticity diagram are distributed over a region which can be well-fit to an elliptical region. These ellipses

are reminiscent of the MacAdam ellipses. The PCA algorithm gives the estimated parameters of a fitted ellipse to the samples. The size of semi-major and semi-minor axes are set to 10 times larger than the standard deviation of the samples around the primary components derived from the PCA method. Figures 3–6 and 3–8 show how the size of semi-major and semi-minor axes and the inclination angle for the fitted ellipses to Munsell and MetaCow samples change with the minimum intensity. The results depict that: first, the orientation of the ellipses is independent of the light level; second, the size of ellipses depends on the light intensity and as the light level decreases the variation in the size of ellipses falls off; third, the bluish patches have smaller sized ellipses while the ellipses of reddish patches are larger in size, which is in agreement with the available chromatic discrimination ability curves (e.g. see Fig. 7. of [16]).

3.5 Concluding Remarks

This chapter investigates the effect of photon noise on the cone responses close to the absolute threshold of the visual system (i.e. the lowest possible level of light in which rods get activated by photons [132]), and points out the importance of addressing scotopic conditions in machine vision applications. In this regard, the potential of spectral modeling is exploited to reveal the uncertainties of cone responses due to the physical nature of light. A photon detection framework and the associated basic physical principles behind photon emission are employed to predict how cone responses may be affected by the intensity of light. The results of this research indicate that: first, even ideal cone responses in the scotopic range become uncertain; second, an ellipse fits the chromaticity distribution associated with cone responses

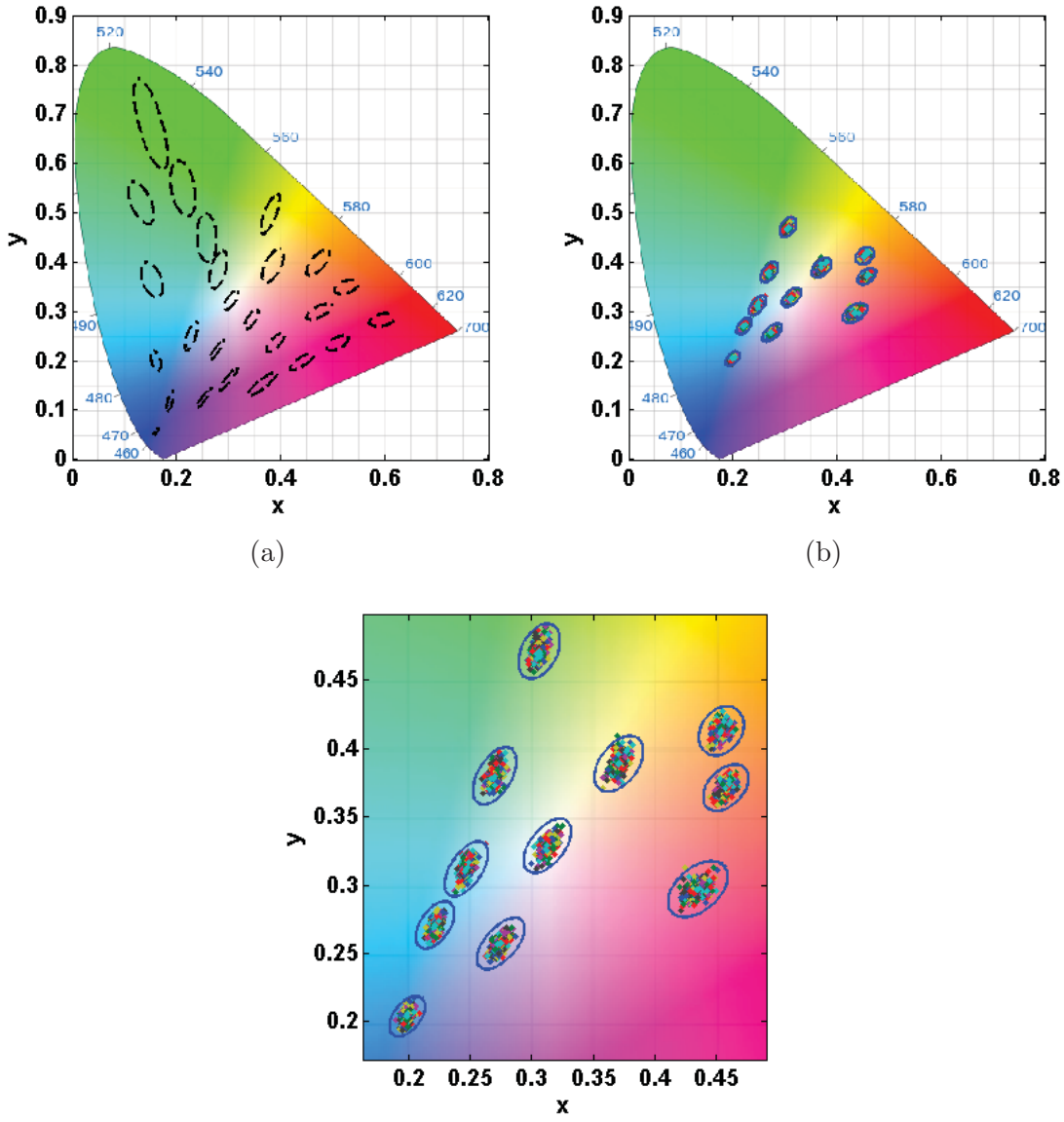

(a) (b)

(c)

Figure 3–5: The results of scenario II performed over the Munsell database. (a) MacAdam (1942) ellipses for observer PGN plotted in the chromaticity diagram. (b) Drawn samples for each color patch and the fitted ellipse to each sample set are plotted.(c) The results of sub-figure (b) are magnified.

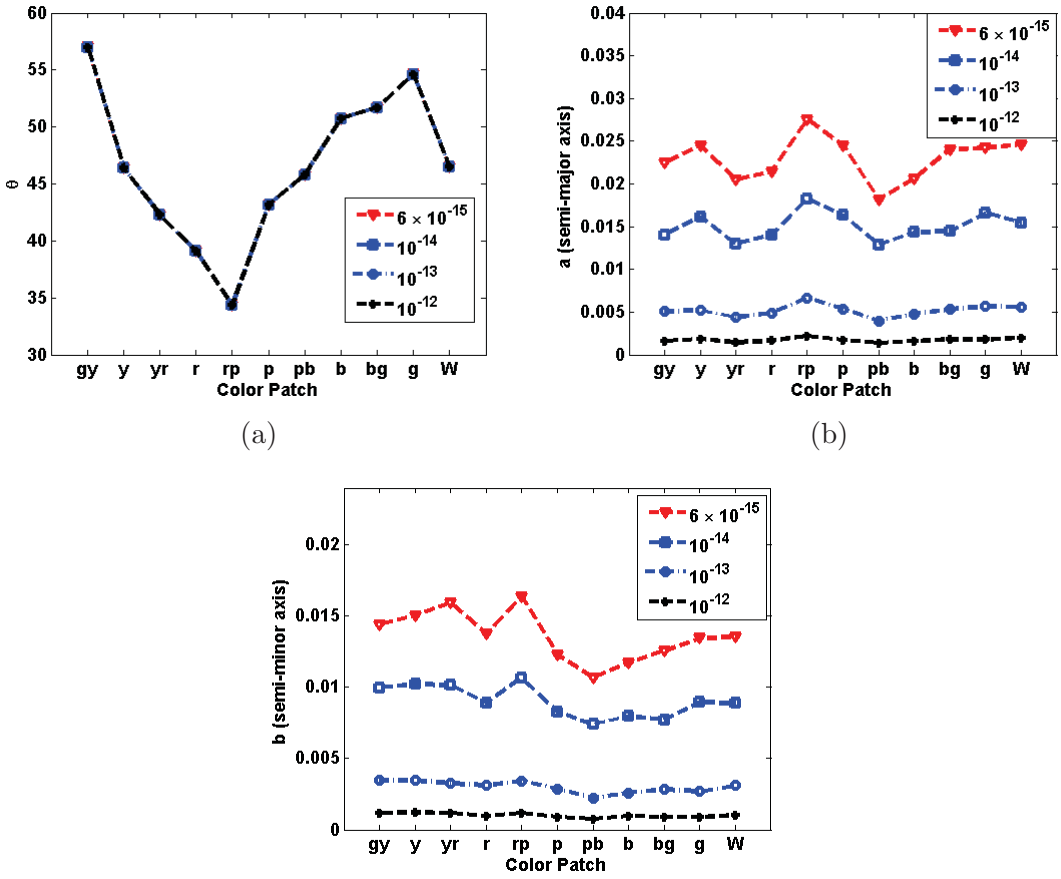

Figure 3–6: The estimated parameters of fitted ellipses to the Munsell samples. (a) The estimated inclination angles of ellipses obtained from the PCA algorithm for different minimum low intensities are shown for all color patches.(b,c) The semi-major and semi-minor size of fitted ellipses for various minimum intensity levels are shown, respectively.

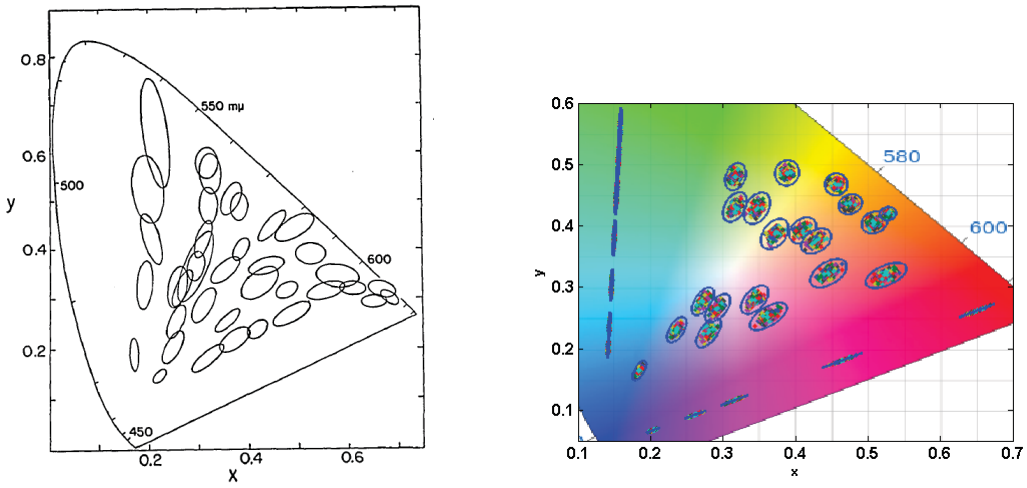

(a) (b)

Figure 3–7: The results of scenario study II performed over the MetaCow database. (a) Brown-MacAdam (1949) ellipses for observer WRJB plotted in the chromaticity diagram. The image is taken from [5]. (b) Drawn samples for each spectral sample of the MetaCow database and the fitted ellipse to each sample set are plotted.

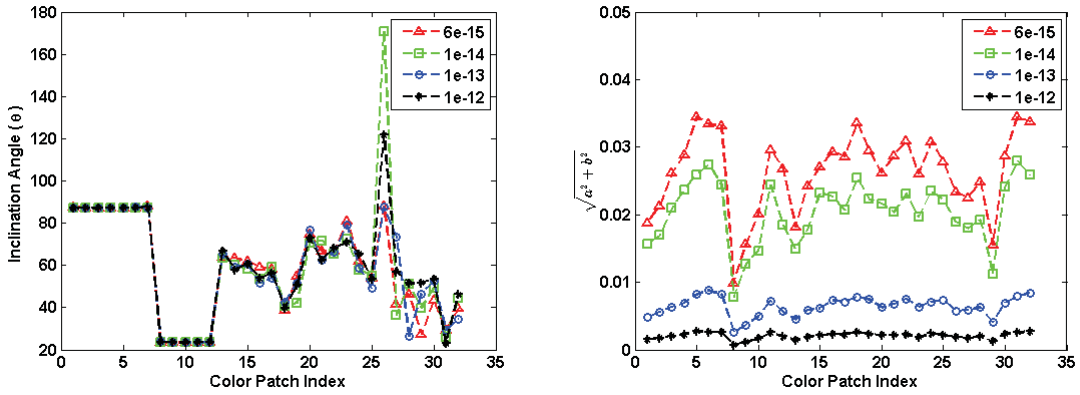

(a) (b)

Figure 3–8: The estimated parameters of fitted ellipses to the MetaCow samples. (a) The estimated inclination angles of ellipses obtained from the PCA algorithm for different minimum low intensities are shown for all color patches. (b) The size of fitted ellipses for various minimum intensity levels are shown, respectively.

to each color patch; third, the size of ellipses depends on the chromaticity of the color patch, the light level, and the spectral composition of light; and, fourth, the orientation of ellipses depends on the chromaticity of the color patch and the spectral composition of light. The results of this chapter have implications for modeling human visual perception close to the absolute threshold, developing a uniform color space for low light levels, and reproducing (simulating) dim images more accurately. At the present time, machine vision and computer graphics algorithms underestimate the impact of photon noise on the appearance of dim images, for which the methodology of this chapter can be leveraged as a practical solution for simulating scotopic scenes.

CHAPTER 4
At Night: Image Sensor Modeling and Color Measurement at Low Light Levels

One of the most important challenges that arises at low light levels is the issue of noise, or more generally speaking, low signal to noise ratios. In Chapter 3, the effect of photon noise on cone responses was investigated close to the absolute threshold of the visual system. In this chapter, effects of different image sensor noises such as photon noise, dark current noise, read noise, and quantization error are investigated on low light color measurements (scotopic and mesopic ranges). A typical image sensor with a detailed model of noise is implemented and employed for this study. We perform simulations with different scenarios to derive the patterns of behavior corresponding to each type of noise from the implemented image sensor outputs.

4.1 Image Sensor Modeling

The focus of this section is on modeling and simulating the image sensor of a digital camera. We consider the image formation model, noise model, and analog to digital converter (ADC) components in the image sensor model. Figure 4–1 shows a diagram of an image sensor model, which is the modified version of the Hasinoff model introduced in [133]. We can think of two main reasons for modeling digital camera imaging systems. First, it is done to reconstruct hyperspectral images taken by spectrometers, or to be used in computer graphics applications. Second, it helps evaluate the camera design, output image quality, or optimize the performance of the

camera in terms of adjustable parameters (e.g. exposure time or ISO setting) [134, 133].

A typical digital camera is comprised of the following elements: an optical system, image sensor, image storage, and image processor [135]. When the shutter of a camera opens, a stream of photons enters the camera and falls on the image sensor. A color image sensor consists of three sensor types, which usually are referred to as R, G, and B sensors. The exposure setting determines the amount of photons captured by the sensors. Each sensor type has a specific spectral quantum efficiency (i.e. the proportion of electrons generated as a result of photon catches for an area of 1 (m^2) that subtends 1 (sr)). A pixel of an image sensor consists of a photodetector, a color filter, and a readout circuit. The rain of photons hitting the photodetrector produces a photocurrent. This photocurrent, together with the photodetector dark current (which will be described later), is accumulated during the integration time as far as the sensor capacity allows. The maximum sensor charge capacity is known as the *full well capacity* and determines the level of saturation for each sensor. When the integration time is over, the readout circuit is responsible for measuring the produced voltage in the pixels. This process is prone to noise known as the *readout noise*. The structure of the readout circuit is the main difference between the CCD and CMOS type image sensors.

4.2 Noise Model

Noise can be defined as any unwanted event which degrades the image quality. In our simulation framework, we assume an additive model for the noise and the

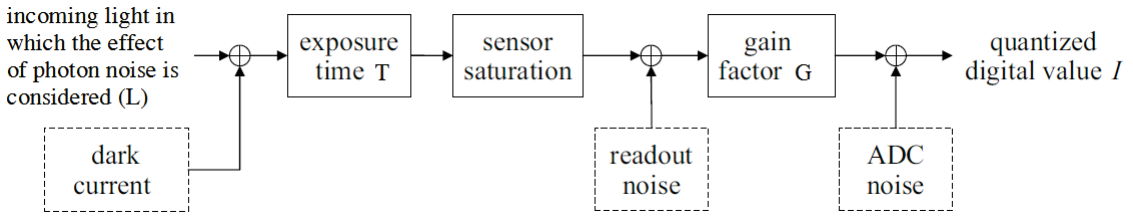

Figure 4–1: Image sensor prototype for a single channel is shown.

following noise types are considered as the most significant sources underlying the image distortion.

-Photon Shot Noise: This can be defined as the variations in the number of photons emitted from the light source and, consequently, the number of photons detected in the image sensor at different times. This phenomenon is rooted in the probabilistic nature of photon emission as described in section 3.1.

-Dark Current Noise: The current produced inside the image sensor in the absence of light is referred to as the *dark current noise*. This current is not generated as a result of photogeneration, but as a result of the impurities that exist in the silicon wafer [136]. Dark current noise is also known as *thermal noise* and ambient temperature has a high influence on its amplitude. Dark current introduces shot noise to the measurement [136] and can be modeled by a Poisson distribution with a variance of $(\sigma_{dark}^{\kappa})^2$ for the κ^{th} sensor type. Since the variance of a Poisson distribution is equal to its mean, the parameter $(\sigma_{dark}^{\kappa})^2$ represents the average number of generated electrons as a result of dark current for each pixel per unit time.

$$N_{dark}^{\kappa}(\alpha, \beta) \sim \text{Pois}((\sigma_{dark}^{\kappa})^2) \tag{4.1}$$

-Read Noise: This refers to the noise in the readout circuit, caused by an on-chip amplifier, and can be modeled as having a white Gaussian distribution with standard deviation σ_{read}[137]. Readout noise is one of the factors that limits the dynamic range of image sensors.

$$N_{read} \sim \mathrm{N}(0, \sigma_{read}) \tag{4.2}$$

-Quantization Noise: In the last step of generating the digital image in the image sensor prototype, the amplified voltage should be quantized into discrete values. Quantization error introduced in this step is known as *quantization noise* and represented as σ_{adc}. The induced noise by the amplifier of the analog-to-digital conversion unit (ADC) is considered negligible.

4.3 Photon Noise Aware Formulation of the Light Spectral Power Distribution

In this section, we discuss a continuous form of the spectral photon noise modeling, which was introduced in section 3.1. Photon emission from a light source follows a Poisson distribution. For a monochromatic light source of particular wavelength λ_0 and known average number of emitted photons per second x, the probability of emitting n photons per unit of time can be obtained by Eq. 3.1. Given the spectral radiance, $L(\lambda)$, the average emitted number of photons, per unit time, per unit area, and per unit steradian, for a central wavelength λ_0 can be obtained by calculating the following integral over an infinitely small range of $[\lambda_0 - \delta/2, \lambda_0 + \delta/2]$:

$$x(\lambda_0) = \frac{1}{hc} \int_{\lambda_0 - \delta/2}^{\lambda_0 + \delta/2} \lambda L(\lambda) \;\; d\lambda. \tag{4.3}$$

The wavelength range of the spectrum, $[\lambda_{min},\ \lambda_{max}]$, can be discretized into N intervals of the length δ such that $\{\lambda_{max} - \lambda_{min} = N\delta\}$. Hence, $x(\lambda_i)$ of the i^{th} wavelength bin can be approximated as:

$$x(\lambda_i) = \frac{1}{hc}\int_{\lambda_i-\delta/2}^{\lambda_i+\delta/2} \lambda L(\lambda)\ \ d\lambda \approx \frac{\lambda_i L(\lambda_i)\delta}{hc}. \tag{4.4}$$

Let $L(\lambda)$ represent the high intensity radiance of a light. Our goal is to derive an estimate of this spectral radiance at an arbitrary lower intensity. The high intensity spectral radiance is the most complete description of the light, and this quantity, at any lower intensity, can be predicted from the given high intensity spectrum, as follows.

The Poisson distribution, $\text{Pois}(x(\lambda_i))$, corresponding to each bin of the high intensity spectral radiance is fully characterized by knowing the $x(\lambda_i)$ values. We define the intensity factor $F \leq 1$, which is a scale factor to change the light level. The estimated spectral radiance after applying the intensity factor F can be obtained by drawing samples, $\{\tilde{X}_F(\lambda_i)\}_1^N$, from $\{\text{Pois}(F \times x(\lambda_i))\}_1^N$ distributions. Hence, the estimated spectral radiance, $\tilde{L}_F(\lambda)$, for the intensity factor F and central wavelength λ_i is given by:

$$\tilde{L}_F(\lambda_i) = \frac{\tilde{X}_F(\lambda_i) \times hc}{\lambda_i \delta}. \tag{4.5}$$

By taking this approach, we can establish the effect of shot noise on low light spectral radiance estimations. It is worth mentioning that $\tilde{L}_{FN}(\alpha, \beta, \lambda)$, which denotes the quantal number of photons falling on the location (α, β) of the image sensor in $(photons/sec/m^2/sr/nm)$, can be obtained from the radiance quantity $\tilde{L}_F(\alpha, \beta, \lambda)$,

as

$$\tilde{L}_{FN}(\alpha, \beta, \lambda) = \frac{\tilde{L}_F(\alpha, \beta, \lambda) \times \lambda}{hc}. \tag{4.6}$$

4.4 Pixel Measurement Model

The voltage produced by an image sensor can be determined by using the following formula:

$$V^{\kappa}(\alpha, \beta) = G_{Ve^-} \times f_{sat}\left(T \times \int_{\lambda_{min}}^{\lambda_{max}} \tilde{L}_{FN}(\alpha, \beta, \lambda) Q_e^{\kappa}(\lambda) d\lambda + T \times N_{dark}^{\kappa}(\alpha, \beta)\right). \tag{4.7}$$

In this equation, $\kappa \in \{R, G, B\}$, T indicates the exposure time in (sec), G_{Ve^-} is the conversion gain in $(volts/e^-)$, $\tilde{L}_{FN}(\alpha, \beta, \lambda)$ represents the number of incident photons at the location (α, β) of the image sensor obtained from the spectral radiance $\tilde{L}_F$ at intensity factor F in $(photons\ /sec\ /m^2\ /sr\ /nm)$, and $Q_e^{\kappa}(\lambda)$ is the quantum efficiency of the κ^{th} sensor in $(e^-\ m^2\ sr/photons)$, $N_{dark}^{i}(\alpha, \beta)$ represents the number of generated electrons as a result of dark noise in the κ^{th} channel for the pixel (α, β), and $f_{sat}(.)$ indicates the saturation function of the sensor.

The quantum efficiency curve for the κ^{th} sensor type is defined as the proportion of the electrons generated by the sensor, N_e^{κ}, to the number of incident photons with the wavelength (λ), N_{ph}^{κ} [138].

$$Q_e^{\kappa}(\lambda) = \frac{N_e}{N_{ph}^{\kappa}(\lambda)} \tag{4.8}$$

The measured voltage by the readout circuit is found with this equation:

$$\tilde{V}^{\kappa}(\alpha,\beta) = V^{\kappa}(\alpha,\beta) + N_{read}(\alpha,\beta) \tag{4.9}$$

The raw output image of the camera can be obtained after applying the gain factor, and the quantization process is as follows.

$$I^{\kappa}(\alpha,\beta) = [G \times \tilde{V}^{\kappa}(\alpha,\beta)]_{n_b} \tag{4.10}$$

In the above equation, $[.]_{n_b}$ represents the "n_b-bit" quantization operation that outputs the integer part of the given operand $G \times \tilde{V}^{\kappa}(\alpha,\beta)$, in the range of $[0, 2^{n_b} - 1]$. Hence, the standard deviation of the quantization noise of the κ^{th} channel at the location (α,β) of the image is given by

$$\sigma_{ADC}(\alpha,\beta)^{\kappa} = I^{\kappa}(\alpha,\beta) - G \times \tilde{V}^{\kappa}(\alpha,\beta). \tag{4.11}$$

Finally, the *signal-to-noise ratio* (SNR) can be defined as the ratio of the non-saturated output of the noise free signal to the variance of the noise. The total variance of noise for each sensor type at each pixel location can be estimated as follows [139]:

$$Var^{\kappa}(\alpha,\beta) = V^{\kappa}(\alpha,\beta) \times G^2 + \sigma^2_{read} \times G^2 + (\sigma^{\kappa}_{ADC}(\alpha,\beta))^2. \tag{4.12}$$

For non-saturated pixels in the image, the SNR value of each channel can be obtained by the following formula [133]:

$$SNR^{\kappa}(\alpha,\beta) = \frac{\left[G \times G_{Ve^-} \times T \times \int_{\lambda_{min}}^{\lambda_{max}} \tilde{L}_{FN}(\alpha,\beta,\lambda) Q^{\kappa}_{e}(\lambda) d\lambda\right]^2_{n_b}}{V^{\kappa}(\alpha,\beta) \times G^2 + \sigma^2_{read} \times G^2 + \sigma^2_{ADC}}. \tag{4.13}$$

Using the introduced model of the image sensor, we are able to investigate the effects of different types of noises on the color measurements of image sensors at various light levels.

4.5 Results and Discussion

4.5.1 Materials and Methods

We designed a set of simulations intended to investigate the effects of different noise types on the color measurements of image sensors. The simulations were done using the spectral radiances selected from "A Data Set for Color Research," prepared by Barnard et. al [140]. The data set contains the spectral sensor sensitivity curves of the Sony DXC-930 three chip CCD video camera, and the spectra of 23 of the Macbeth color patches illuminated by 26 different light sources. The Sony DXC-930 sensor sensitivity curves are used in the image sensor simulation phase of this work, and the spectra, which we refer to as the *RGB598* spectral database, are leveraged for our simulations. The sensor quantum efficiency curves are shown in Fig. 4–3. Each spectrum is sampled in 4 nm steps from 380 to 780. Details about this database can be found in [140]. The chromaticities spanned by the 598 spectra of this database are shown in the chromaticity diagram in Fig. 4–2, and among these points, 20 are selected for the sake of our simulations. First, each spectral radiance is scaled to have a spectrum with a luminance value of 100 (cd/m^2), then to obtain a lower luminance value, the spectrum is used as $L(\lambda)$ in Eq. 4.4-4.6 to estimate the corresponding low intensity spectral radiance $\tilde{L}_F$ at an intensity factor F. It is worth mentioning that since the luminances of the scaled spectral radiances are set to 100

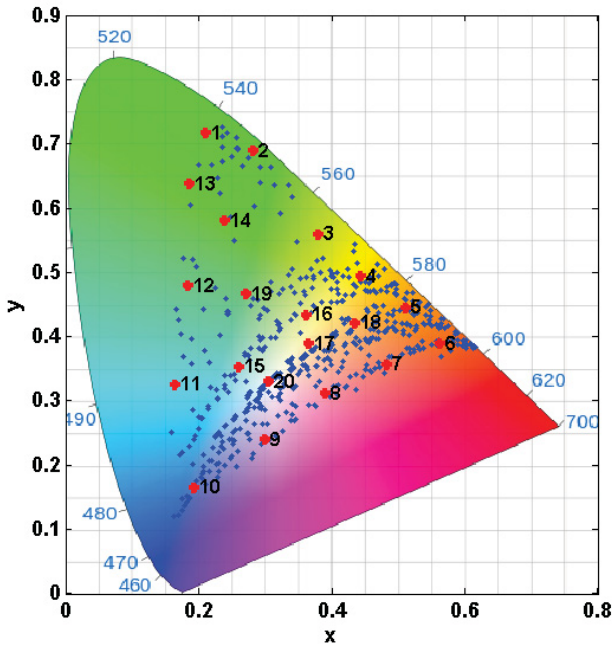

Figure 4–2: The chromaticity values spanned by the *RGB598* spectral database are indicated by blue dots. The selected data points are marked as red asterisks with designated numeric indices.

(cd/m^2) at the intensity factor $F = 1$, the approximate luminance value of $\tilde{L}_F$ can be obtained with the formula: $F \times 100(cd/m^2)$.

For each data point, the raw output of the image sensor is generated from the modeled framework at a specific condition defined for each scenario. The parameters selected for the image sensor model at the temperature of $20°C$ are listed in Table 5–3. The camera black RGB for Sony DXC-930 is provided in the $RGB598$ database and this value is scaled to obtain the variance of dark noise $(\sigma^{\kappa}_{dark})^2$. Full-well capacity, read noise standard deviation (σ_{read}), and the conversion gain (G_{Ve^-}) are selected from [135]. Based on these selected values, the parameter G is determined such

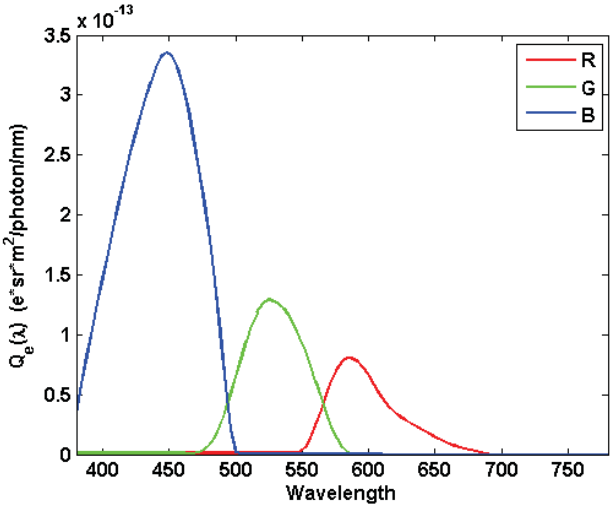

Figure 4–3: The quantum efficiency curves of image sensors in $(e^{-}\ sr\ m^2/photon/nm)$.

that the output of sensor best fits the empirical measurements given in the $RGB598$ database.

To account for uncertainties imposed by noise, 200 measurements are recorded for each sample in each trial. The measured samples (I) are converted to the XYZ space (I_{XYZ}), and then to the xy-chromaticity space. This transformation is given by (assuming that the camera sensitivities can be linearly constructed by the XYZ color matching functions with good precision):

$$\begin{aligned} I_{XYZ} &= M \times I \\ M &= (T_{XYZ} \times T_{XYZ}^{t}) \times (C \times T_{XYZ}^{t})^{-1}. \end{aligned} \tag{4.14}$$

In this formula, T_{XYZ} and C are $(3 \times N)$ matrices representing the XYZ color matching function and the camera sensitivity curves respectively. The camera sensitivity

curves can be obtained through the quantum efficiency function, $Q_e^{\kappa}(\lambda_i)$, as follows:

$$\begin{aligned} C^{\kappa}(\lambda) &= G_{Ve^-} \times G \times Q^{\kappa}(\lambda) \\ Q^{\kappa}(\lambda_i) &= \frac{hc}{\lambda_i} \times Q_e^{\kappa}(\lambda_i) \quad \kappa \in \{R, G, B\}, \quad i \in \{1, 2, ..., N\}. \end{aligned} \tag{4.15}$$

A question may arise here, asking whether it is correct to use CIE photopic colorimetry at low light levels. The answer is yes, as long as we are focusing on the color measurements of the camera and not the color perception of the measured samples at low light levels. Color measurements can be represented in any color space. Moreover, CIE photopic colorimetry is commonly used in cameras for the process of creating the output image. Hence, we record the measurements at low light conditions and evaluate the photopic appearance of the measured samples.

The simulations were carried out over three scenarios and followed by an SNR sensitivity analysis. Before demonstrating the results, we state the main assumptions and considerations of this work.

1. Temperature is assumed constant, and so the dark noise parameters are fixed in the simulations.
2. The noise model is additive in the image sensor simulation framework.
3. The image sensor linearly responds to light intensity variations before its saturation limit. Sensor linearity is discussed in [141] in more detail. In [141], Barnard and Funt mentioned that "The Sony DXC-930 camera that we used for our experiments is quite linear for most of its range, provided it is used with gamma disabled."
4. Raw uncompressed output images are considered for our analysis.

Table 4–1: Parameters of the Model at $20°C$

Sensor Parameters	Parameter Value
$G_{Ve^-}(V/e^-)$	0.0002
$(\sigma^{\kappa}_{dark})^2$ $(e^-/pixel/sec)$	$[195, 230, 218]$
σ_{read} (e^-)	4
G	141.67
Full Well Capacity(e^-)	9000
T(sec)	1
n_b	8

5. *Reset noise*, *photodetector response nonuniformity* (PRNU), and *dark signal nonuniformity* (DSNU) are not incorporated in our modeling. For our research, we assume that their impacts on the introduced model are negligible. For further details refer to [139].
6. Color measurements are done at low light levels but evaluated in photopic conditions. Hence, the use of photopic uniform color spaces such as CIE Lab to analyse the results can be justified accordingly.

We performed the simulations according to three scenarios which will be described in the coming subsections. The paradigm of the simulations in each of these scenarios is depicted in Fig. 4–4. Given the parameters of the image sensor and an arbitrary high intensity spectral power distribution, a measured sample set of the input SPD will be generated by the image sensor to take into account the randomness in the image sensor or the SPD over time. Then the measured samples are transformed to the XYZ space. The principal components analysis (PCA) will be performed over the XYZ samples to find the parameters of an ellipse which can be best fit to the chromaticity distribution of the measured sample set. At the same

time, the XYZ samples are converted to the CIE Lab space to be compared to the noise free sample using the ΔE_{ab} color difference metric.

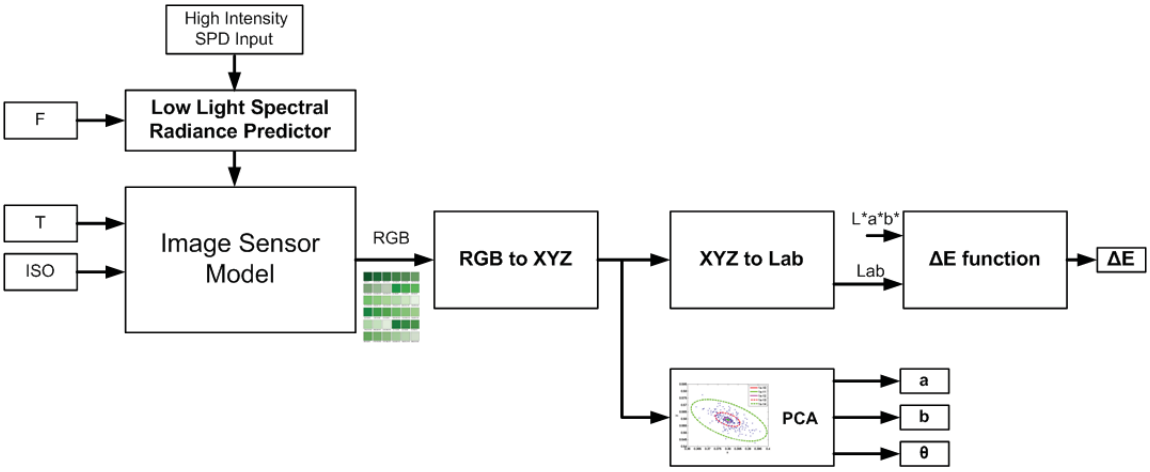

Figure 4–4: A basic schematic of the simulation procedure is shown. $L^*a^*b^*$ represents the noise free measurement from the image sensor in the Lab color space.

4.5.2 Scenario I: Ideal Image Sensor and Light Intensity

In the first scenario, we consider the case where there is no noise corrupting the output image, and we have a perfect image sensor that is able to detect single photon events and the sensor can respond without saturation. We would like to investigate the effect of photon noise on the color measurements of an ideal image sensor. In this regard, the 20 data points shown in Fig. 4–2 are considered for this scenario. The log of the intensity factor is set to values $\log(\mathrm{F}) \in \{0, -7, -8, -9, -10, -11, -12, -13, -14\}$. The results of the simulations are shown in Figs. 4–5 and 4–6. Figure 4–5-a indicates that generated samples form an elliptic shape in the chromaticity diagram. The Principal Components Analysis (PCA) algorithm is used to find a fitted ellipse for generated samples of each data point [142].

Generated samples and the fitted ellipses of the third data point for different intensity factors, as well as the number of incident photons on the image sensor for various luminance values are plotted in Figs. 4–5-b and 4–5-c respectively. In Fig. 4–5-b, the distance between consecutive ellipses grows as the light intensity decreases. Figures 4–6-a and 4–6-b show the inclination angle and size of the fitted ellipses for some intensity factors. The approximate size of each ellipse is found with the formula $\sqrt{a^2 + b^2}$, where a and b represent the size of the semi-major and semi-minor axes of the ellipse. The inclination angle represents the angle between the semi-major axis and the x-axis of the xy-chromaticity space. The results indicate that the inclination angles, with a good approximation, are independent of the intensity level; however, the size of the ellipses inversely changes with intensity, suggesting that even if we had an ideal image sensor with no internal noise, we would still have to deal with the photon noise and uncertainties imposed by physical limitations. Since distances in the chromaticity diagram do not correspond to the human visual system color discriminability, the perceptual distance metric ΔE_{ab} is used as an index to show to what extent the effect of noise on color measurement at different intensities would be noticeable to a human observer from trial to trial. In this regard, for each data point, the ΔE_{ab} measure is derived as follows:

1. The standard D65 illuminant is assumed as the white reference for the calculations at the luminance of 100 cd/m^2 (the Y value of the reference white is kept constant during the entire simulation).
2. The XYZ values of each sample are scaled to equalize the Y value of the sample and that of the standard illuminant, in order to compare the color coordinates

of the low intensity samples ($F < 1$) and the high intensity sample generated at ($F = 1$).

3. CIELab coordinates of each sample are obtained.
4. ΔE_{ab} is calculated between each sample and the average chromaticity coordinates of corresponding high intensity samples.
5. The average of ΔE_{ab} values over the samples of each intensity factor is reported.

The result of ΔE_{ab} is shown in Fig.4–6-c indicating that as the light level falls off, the chromaticity variations among different measurements of the same color patch (measuring the same color patch over time) become noticeable.

4.5.3 Scenario II: Effects of Dark Current on Image Sensor Responses at Low Light Intensity

It is shown in the first scenario that photon noise may cause uncertainties in the measurements in the scotopic range when the image sensor is deemed ideal and no other noises may disturb the measurement. In this subsection, the effect of dark current is examined separately from the other intrinsic noise types, when only photon noise and dark current affect the image sensor, and the sensor saturation function is not considered in the sensor model. The intensity factor is set to F $\in \{1, 0.5, 0.1, 0.05, 0.01, 0.005, 0.001\}$ (corresponding to the luminance values of $\{100, 50, 10, 5, 1, 0.5, 0.1\}$ cd/m^2 respectively) during each trial of the simulation. For the sake of this scenario, only the boundary data points (indices 1-13) from the initial 20 data points are used in order to make the resulting figures more clear.

The results shown in Figs. 4–7 and 4–8 indicate that the dark noise may cause more significant effects on the color measurement at lower intensities than does the photon noise. The result is that the dark noise pushes the low intensity measurements

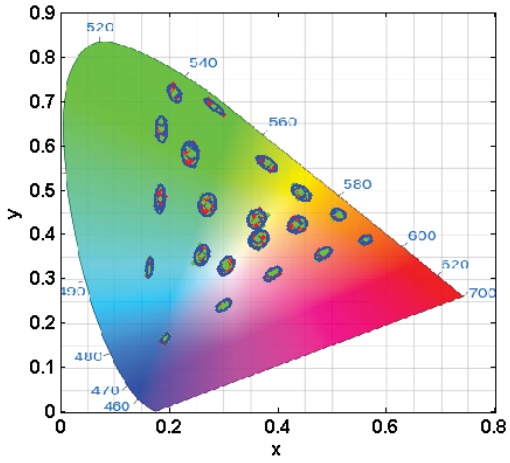

(a)

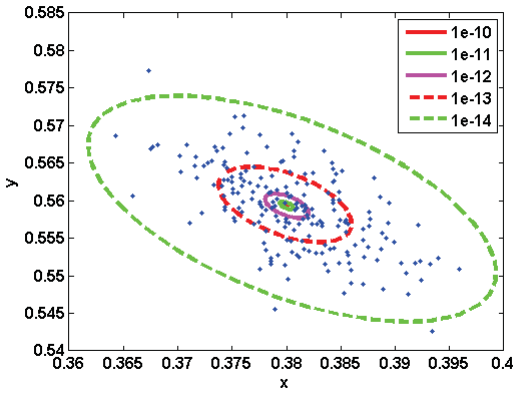

(b)

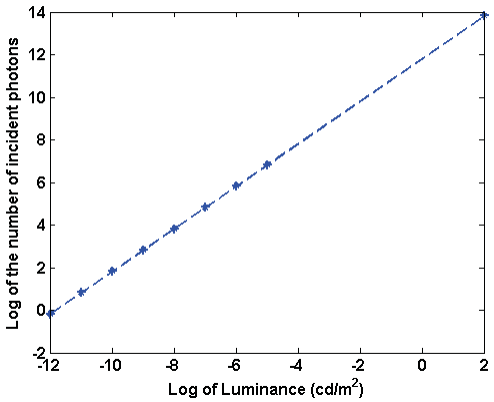

(c)

Figure 4–5: Results of scenario I (part 1): (a) Generated samples for each selected data point of the *RGB598* database. (b) Generated samples and the fitted ellipses for different intensity factors for the data point number 3. (c) The log number of incident photons at different luminance levels.

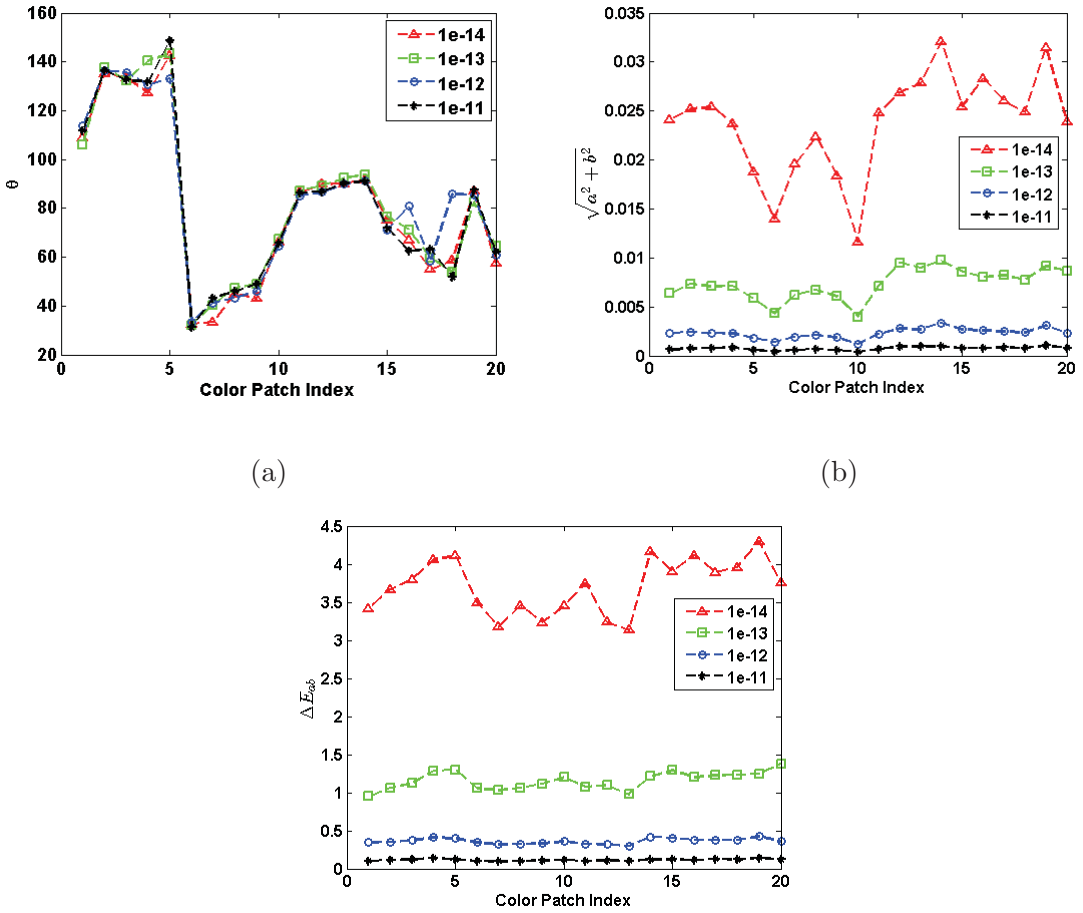

(a) (b)

(c)

Figure 4–6: Results of scenario I (part 2): (a) The estimated inclination angles of ellipses obtained from the PCA algorithm. (b) The size of fitted ellipses corresponding to different intensity factors. (c) The average of ΔE_{ab} values over the samples of each intensity factor.

toward the average chromaticity of the image sensor's black point and shrinks the size of the image gamut. This fact is also analytically proven in section 4.5.4. In comparison to the photon noise, which introduces a more significant effect at a luminance of 10^{-11} cd/m^2 and lower, this issue starts from a much higher luminance value of 10 cd/m^2 for the dark current. This issue indicates the greater effects of dark noise in degrading the quality of measurements, as compared to the effects of phtoton noise. The angle of the ellipses' inclination, θ, induced by the dark noise, is totally different from that of the photon noise. The ellipses are aligned more horizontally for low intensities, and their angles of inclination are separated from each other in different intensity factors than the results of scenario I. Another interesting point is the opposite behavior of the ellipse size variations as a function of the color patch index in different light intensities. In scenario I, the size of the ellipses are more uniform for lower intensity factors than for higher values of F; however, in scenario II, the opposite of this pattern is exhibited, as seen in Fig. 4–8-b, where the size of lower intensity ellipses are more uniform than high intensity values.

4.5.4 Dark Current Noise Impacts on the Color Gamut of Dark Images

The results of scenario II show that dark current induces some chromaticity shifts on the measured samples by the camera, which leads to desaturating captured colors. In this subsection, we provide an analytical rationale to explain the color desaturation of measured samples resulting from dark current noise in the image sensor.

The measured sample (noisy sample), I, can be decomposed into the noise free component, Δ, and the dark current noise, n.

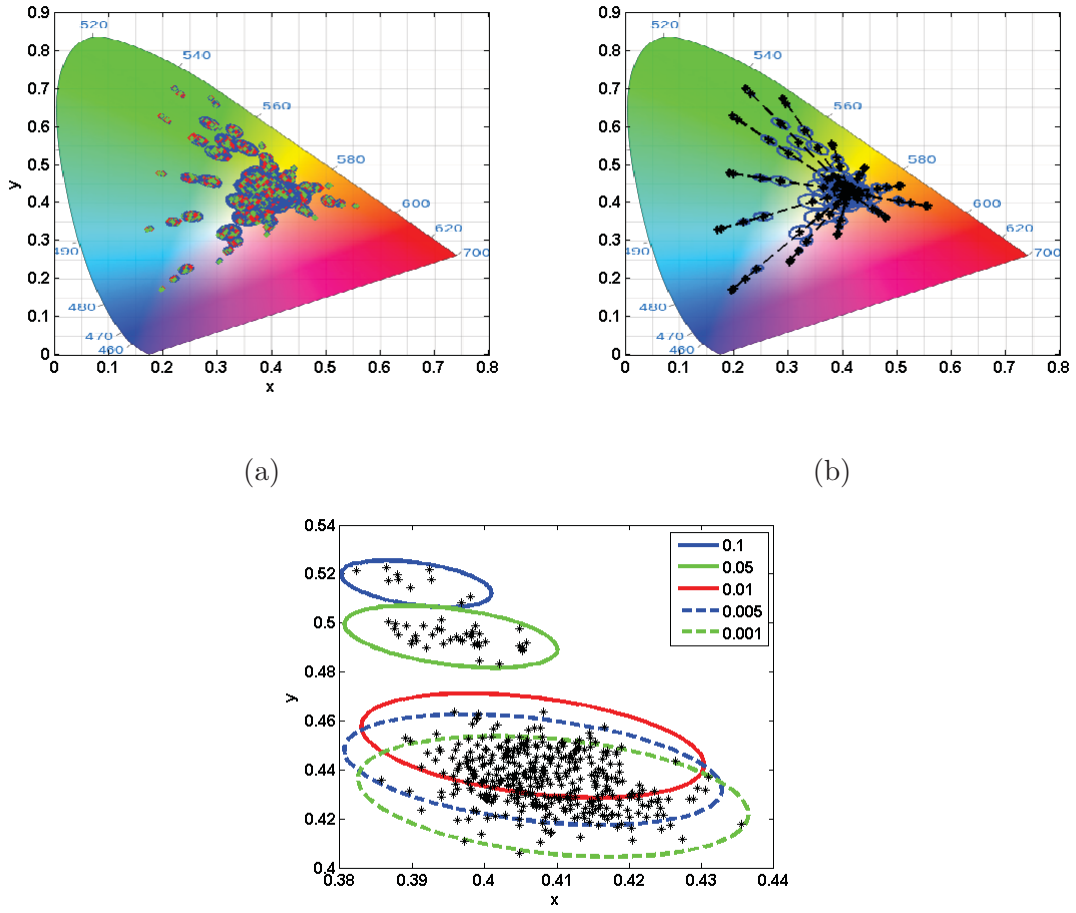

(a) (b)

(c)

Figure 4–7: The results of scenario II performed over the *RGB598* database when only photon noise and dark noise are taken into account in the image formation model. (a) Drawn samples for each selected data point of the *RGB598* database and the fitted ellipse to the samples are plotted. (b) Subfigure in part (a) is regenerated after removing the samples and specifying the center of ellipses together with the line of movement of each data point with the light level (c). The result of sub-figure (a) is magnified for the datapoint number 3.

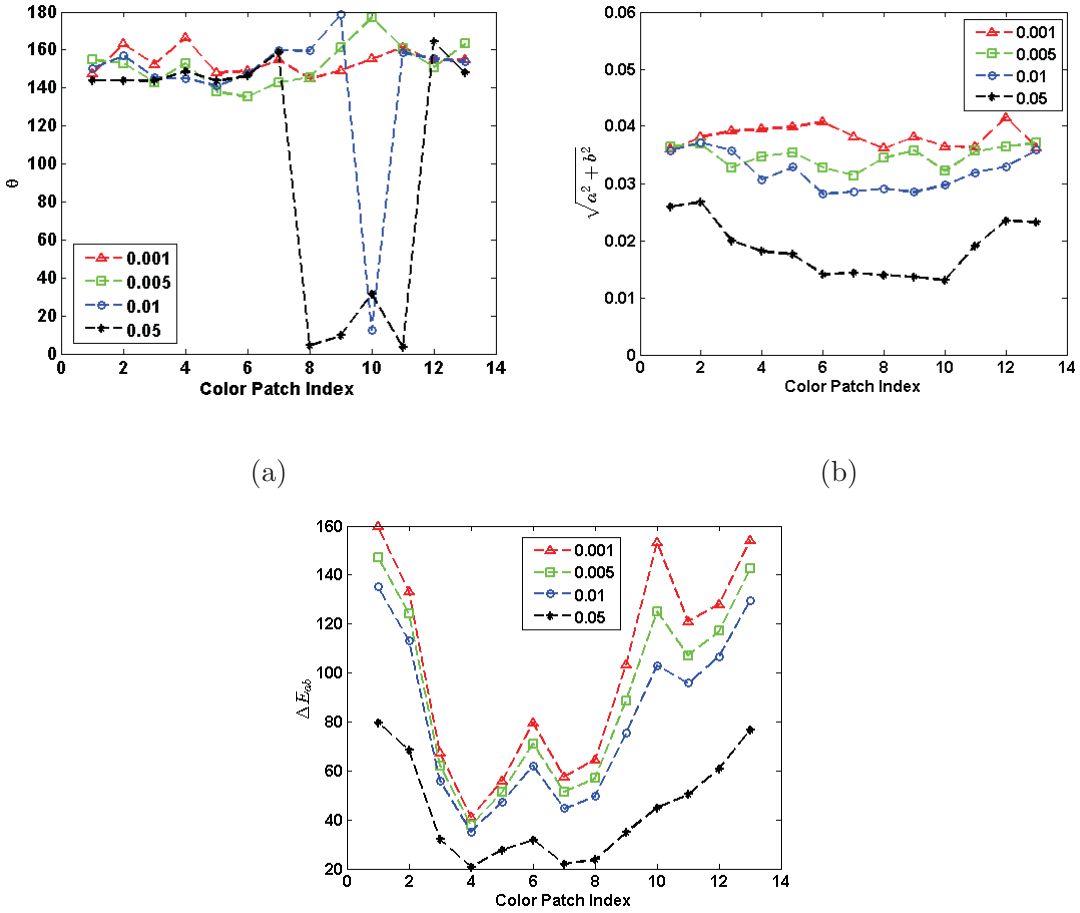

Figure 4–8: The results of scenario II performed over the *RGB598* database when only photon noise and dark noise are taken into account in the image formation model. (a) The estimated inclination angles of ellipses obtained from the PCA algorithm for different intensity factors are shown for all color patches. (b) The size of fitted ellipses corresponding to different intensity factors for all selected color patches is compared. (c) The average of ΔE_{ab} values over the samples of each intensity factor.

$$I = \Delta + n \tag{4.16}$$

We transfer the measured sample to the XYZ space by applying the transformation matrix M:

$$I_M = MI = M\Delta + Mn = \Delta_M + n_M. \tag{4.17}$$

$$I_M = \begin{bmatrix} i_M^1 \\ i_M^2 \\ i_M^3 \end{bmatrix}, \Delta_M = \begin{bmatrix} \delta_M^1 \\ \delta_M^2 \\ \delta_M^3 \end{bmatrix}, n_M = \begin{bmatrix} n_M^1 \\ n_M^2 \\ n_M^3 \end{bmatrix} \tag{4.18}$$

Then the xy-chromaticity values corresponding to each component I_M, Δ_M, n_M are derived.

$$\begin{aligned} I_c &= \begin{bmatrix} i_c^1 \\ i_c^2 \end{bmatrix} = \frac{1}{i_M^1 + i_M^2 + i_M^3} \begin{bmatrix} i_M^1 \\ i_M^2 \end{bmatrix} = \kappa_1 \begin{bmatrix} i_M^1 \\ i_M^2 \end{bmatrix} \\ \Delta_c &= \begin{bmatrix} \delta_c^1 \\ \delta_c^2 \end{bmatrix} = \frac{1}{\delta_M^1 + \delta_M^2 + \delta_M^3} \begin{bmatrix} \delta_M^1 \\ \delta_M^2 \end{bmatrix} = \kappa_2 \begin{bmatrix} \delta_M^1 \\ \delta_M^2 \end{bmatrix} \\ n_c &= \begin{bmatrix} n_c^1 \\ n_c^2 \end{bmatrix} = \frac{1}{n_M^1 + n_M^2 + n_M^3} \begin{bmatrix} n_M^1 \\ n_M^2 \end{bmatrix} = \kappa_3 \begin{bmatrix} n_M^1 \\ n_M^2 \end{bmatrix} \end{aligned} \tag{4.19}$$

The following equation holds between conversion factors κ_1, κ_2, and $\kappa 3$.

$$\frac{1}{\kappa_1} = \frac{1}{\kappa_2} + \frac{1}{\kappa_3} \Rightarrow \kappa_1 = \frac{\kappa_2 \kappa_3}{\kappa_2 + \kappa_3} \tag{4.20}$$

The relation between the chromaticity components can be obtained as follows:

$$\begin{aligned} i_M^1 &= \delta_M^1 + n_M^1 \\ i_c^1 &= \kappa_1 i_M^1 = \frac{\kappa_2\kappa_3}{\kappa_2+\kappa_3} i_M^1 = \frac{\kappa_2\kappa_3}{\kappa_2+\kappa_3}\delta_M^1 + \frac{\kappa_2\kappa_3}{\kappa_2+\kappa_3} n_M^1 \\ &= \frac{\kappa_3}{\kappa_2+\kappa_3}(\kappa_2\delta_M^1) + \frac{\kappa_2}{\kappa_2+\kappa_3}(\kappa_3 n_M^1) = \frac{\kappa_3}{\kappa_2+\kappa_3}\delta_c^1 + \frac{\kappa_2}{\kappa_2+\kappa_3} n_c^1 \end{aligned} \tag{4.21}$$

If α is selected as $\alpha = \frac{\kappa_3}{\kappa_2+\kappa_3}$ then,

$$\begin{aligned} i_c^1 &= \alpha\delta_c^1 + (1-\alpha)n_c^1 \\ i_c^2 &= \alpha\delta_c^2 + (1-\alpha)n_c^2. \end{aligned} \tag{4.22}$$

Equation 4.22 can be written in this matrix form:

$$\begin{aligned} I_c &= \alpha\Delta_c + (1-\alpha)n_c \\ 0 &\le \alpha \le 1. \end{aligned} \tag{4.23}$$

This equation implies that in the xy-chromaticity space the noise free sample, measured sample, and dark noise lie on a straight line. Moreover, the measured sample in the chromaticity diagram lies somewhere between the noise free sample and noise depending on α value. The α factor can be obtained from the noise free signal intensity κ_2 and the dark noise intensity κ_3 as follows:

$$\alpha = \frac{\kappa_3}{\kappa_2+\kappa_3} = \frac{1}{1+\frac{\kappa_2}{\kappa_3}} = \frac{1}{1+\frac{\text{noise intensity}}{\text{signal intensity}}} \tag{4.24}$$

where the noise intensity value can be approximated by the mean value of dark noise.

If we assume that the three channels of the image sensor have similar mean dark current values, the chromaticity of dark noise would be distributed around the white

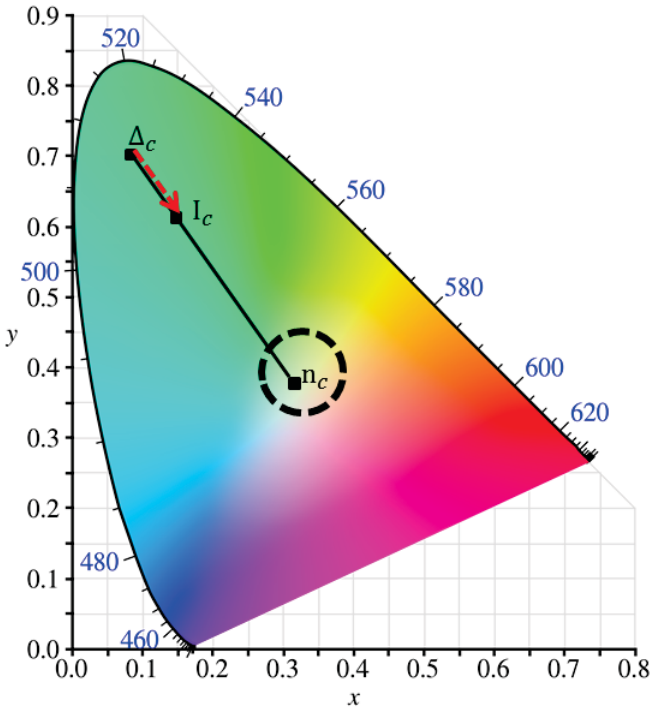

Figure 4–9: The measured samples are pushed toward the white point due to presence of dark current.

point. Hence, we define a sacred region around the white point, which surrounds the dark noise samples. As Fig. 4–9 depicts, the noisy sample would lie between the noise free sample and the white point, implying that the presence of dark noise leads to desaturating the measured samples.

4.5.5 Scenario III: Real Image Sensor Simulation

A similar scenario to scenario II is obtained with all noise types and the saturation function being active. In this case, only data points indices with 1-13 are used to perform the simulation. Figures 4–10 and 4–11 depicts the results. In

Figs. 4–10-a and 4–10-b, some data points make the sensor saturated at high intensity factors. Non-linear effects imposed by these saturated samples are explicitly revealed in Fig. 4–10-b. Moreover, the quantization level in the model leads to sparse samples in the chromaticity diagram, since it is not possible to have all chromaticity values in the output of image sensor. Aside from this, this scenario's pattern of results resembles that of scenario II, implying the dominant influence of dark noise at low light levels.

4.5.6 SNR Sensitivity Analysis

In this subsection, the sensitivity analysis of the SNR value (given in eq. 4.13) to the parameters of dark current, read noise, and including or excluding the quantization noise is presented. In this regard, only one noise is considered at a time (the other noises are deactivated in the model) and the parameters corresponding to that noise are set based on the values given in Table 5–3. For the dark current and read noise, their corresponding parameters ($(\sigma^i_{dark})^2$, and σ_{read} respectively) are incremented by 10%, and the change in the SNR value is averaged over 200 samples drawn in each trial. In Table 5–3, the dark current parameter is given for the temperature of $20°C$. Based on the dark current versus temperature curve given in [139] for a CCD image sensor, to increase dark current by 10% at $20°C$, the temperature should go up approximately by $1°C - 2°C$. The read noise parameter depends on the the type of image sensor (CCD or CMOS) and the ISO setting of the camera. In Fig. 2 of [143], the read noise value of three image sensors is compared and indicates that changing the ISO setting of a CCD chip between the consecutive steps may change the read noise standard deviation by 10%-20%.

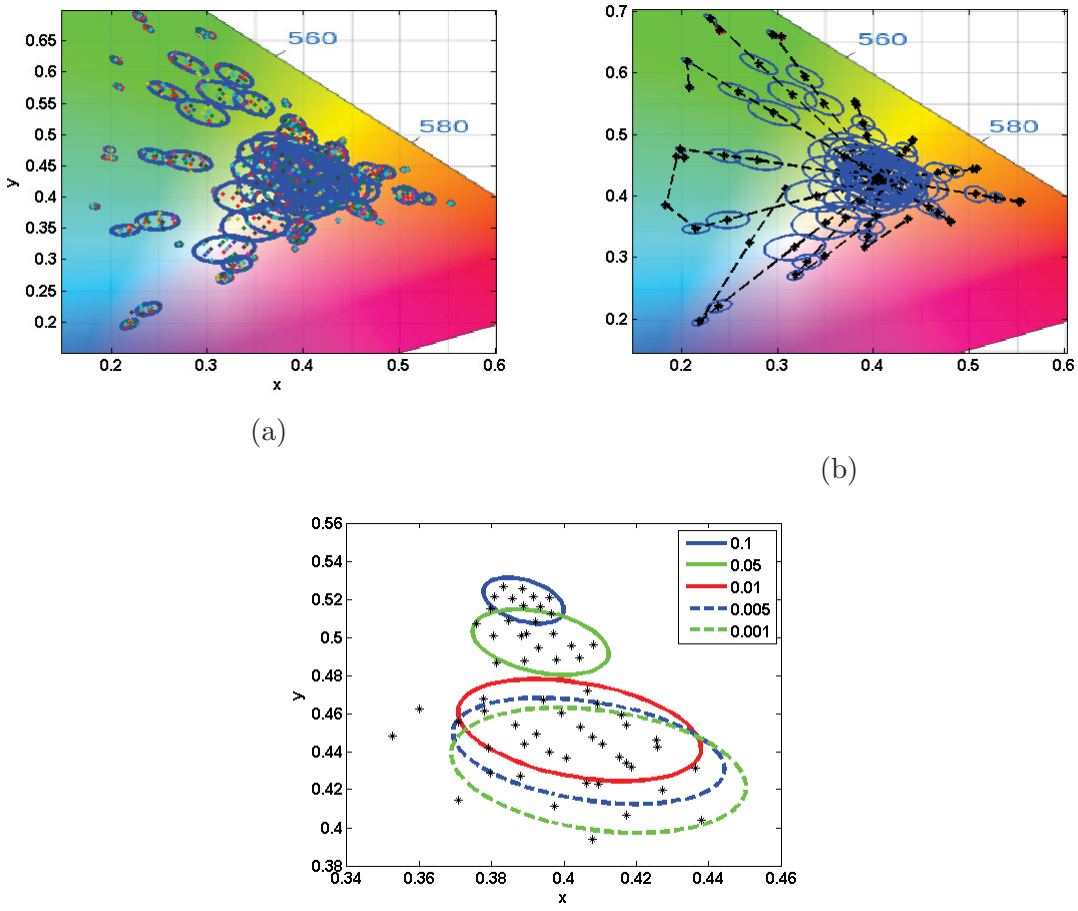

Figure 4–10: The results of scenario III performed over the *RGB598* database when only photon noise and dark noise are taken into account in the image formation model. (a) Drawn samples for each selected data point of the *RGB598* database and the fitted ellipse to the samples are plotted. (b) Subfigure in part (a) is regenerated after removing the samples and specifying the center of ellipses together with the line of movement of each data point with the light level (c) The result of sub-figure (a) is magnified for the datapoint number 3.

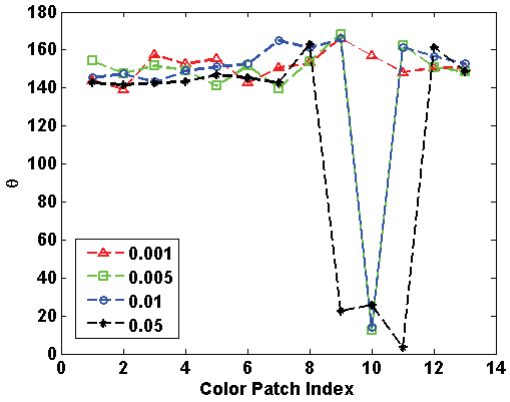

(a)

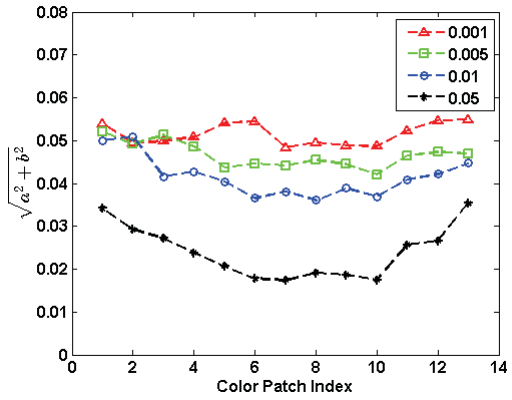

(b)

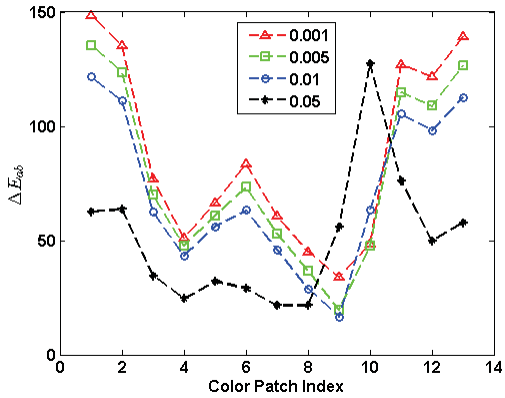

(c)

Figure 4–11: The results of scenario III performed over the *RGB598* database when only photon noise and dark noise are taken into account in the image formation model. (a) The estimated inclination angles of ellipses obtained from the PCA algorithm for different intensity factors are shown for all color patches. (b) The size of fitted ellipses corresponding to different intensity factors for all selected color patches is compared. (c) The average of ΔE_{ab} values over the samples of each intensity factor.

The SNR change can be obtained by the following formula:

$$\Delta SNR(\%) = 100 \times \frac{SNR_1 - SNR_2}{SNR_1}. \tag{4.25}$$

In this equation, SNR_1 and SNR_2 represent the SNR values before and after incrementing the parameters, respectively. Since the noise parameters used for SNR_2 are greater than those of SNR_1, it is expected to have $SNR_1 > SNR_2$, and hence $\Delta SNR > 0$. A similar procedure is used for evaluating the quantization noise by comparing the SNR of the measurements with and without quantization noise. To avoid saturation effects on the results, the intensity factor is set to $F \in \{0.1, 0.05, 0.01, 0.005, 0.001\}$. This analysis is performed on the boundary color patches with the following indices: {1, 3, 6, 8, 10, 12} (see Fig. 4–2). The results of the analysis are reported for the R,G, and B sensor types in Figs. 4–12, 4–13, and 4–14. The maximum of SNR change happens in the smallest intensity factor for the dark current and read noise SNR sensitivity curves. However, this pattern is not seen in the quantization noise SNR sensitivity curves, as the R and G sensors have their maximum in different intermediate intensities. Figure 4–13 shows that the SNR change associated with read noise monotonically increases as the light level falls off. This statement is roughly true for the dark noise curves but does not hold for the quantization noise sensitivity curves. In general, no consistent pattern can be found among the SNR sensitivity results of quantization noise implying that this noise does not highly depend on the intensity value. An interesting point noted in Figs. 4–12 and 4–13 is that for each sensor type, the data points to which the sensor is more sensitive have lower SNR sensitivities compared to other data points. For example,

in Figs. 4–12-a and 4–13-a, the reddish color patch (index=6) has the least SNR sensitivity for almost all intensity factors of the red channel. In Figs. 4–12-b and 4–13-b, for the green sensor, the greenish color patches (index=1,12) have lower SNR sensitivities compared to the other color samples. This conclusion is only true for dark current and read noise curves. Comparing the average SNR sensitivity of the three noise types reveals that read noise variations have the least impact on the SNR (less than 1%), then dark noise affects SNR between 1-9%, and the quantization noise has the most significant influence on SNR.

4.6 Concluding Remarks

This chapter investigated the image sensor color measurement close to its absolute sensing threshold. In this regard, a similar approach to the one introduced in Chapter 3 was used. The results of this investigation are summarized as follows. First, photon noise, read noise, and quantization error lead to uncertain measurements distributed around the noise free measurements. The chromaticities of these noisy samples are distributed in a cloud that can be well-fit to an elliptical region in the xy-chromaticity diagram. Second, even for an ideal image sensor, in very dark situations, stable measurement of the incoming light to the camera is impossible due to the physical limitations imposed by the fluctuations in photon emission rate. Third, dark current noise reveals dynamic effects on color measurements by shifting their chromaticities towards the chromaticity of the camera black point. Fourth, dark current dominates the other sensor noise types in the image sensor in terms of affecting the chromaticity of measurements.

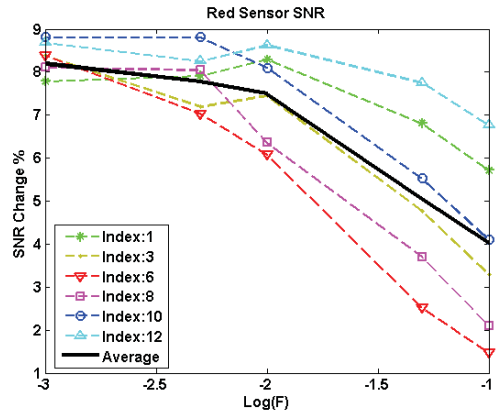

(a)

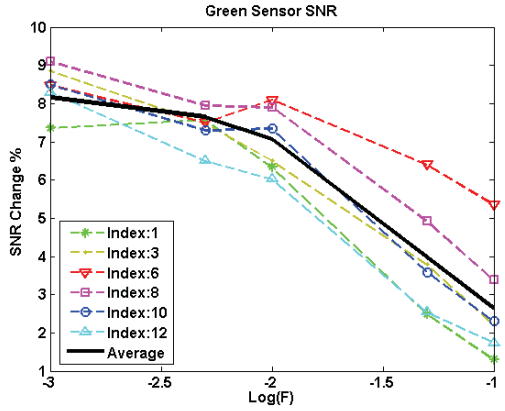

(b)

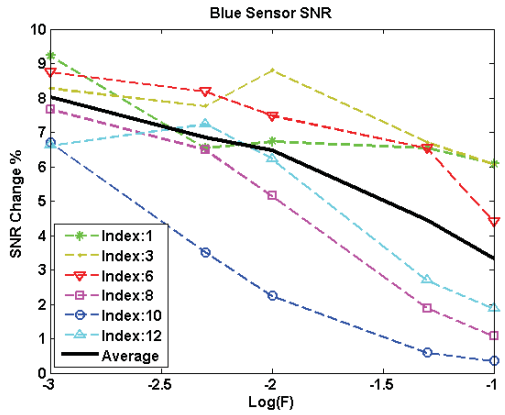

(c)

Figure 4–12: SNR sensitivity curves of the R, G, and B sensor types with respect to the dark current noise parameters for different color patches are plotted in (a), (b), and (c) respectively.

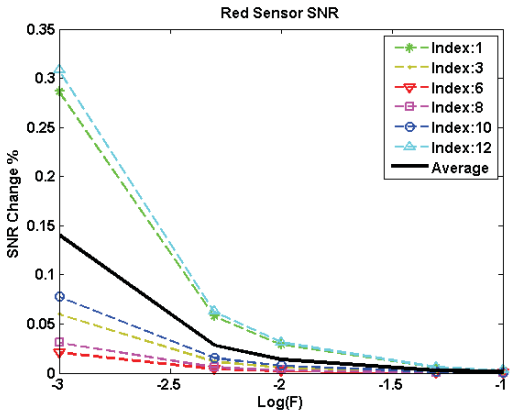

(a)

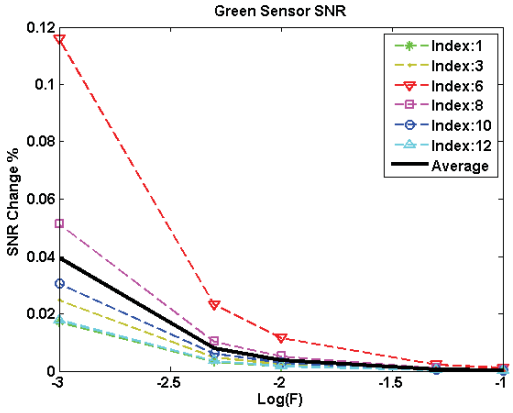

(b)

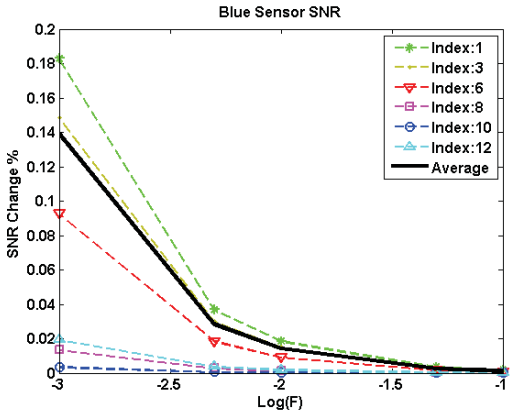

(c)

Figure 4–13: SNR sensitivity curves of the R, G, and B sensor types with respect to the read noise parameters for different color patches are plotted in (a), (b), and (c) respectively.

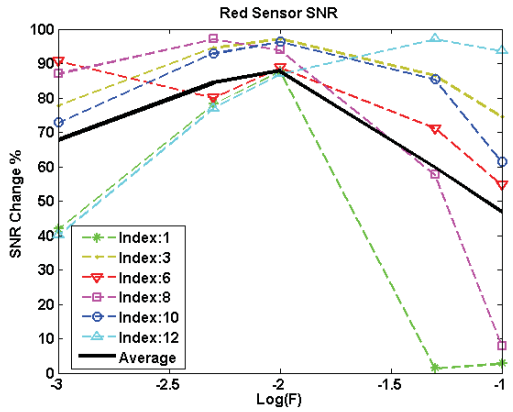

(a)

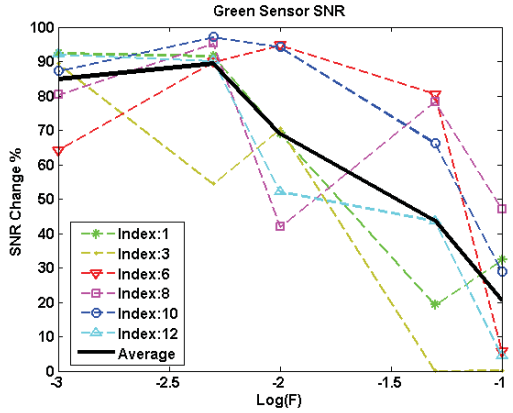

(b)

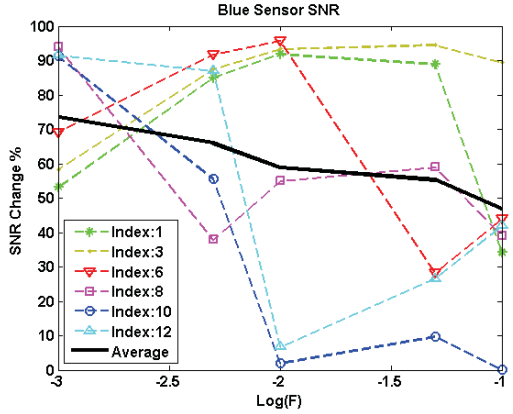

(c)

Figure 4–14: SNR sensitivity curves of the R, G, and B sensor types with respect to the quantization noise for different color patches are plotted in (a), (b), and (c) respectively.

The work presented in this chapter demonstrated that spectral methods can serve as a tool for incorporating photon and dark noise into the image sensor model for color measurement at low light levels. Moreover, photon noise and dark noise, which both follow the Poisson distribution, are the dominant noise types and introduce a more significant error to the image sensor measurements in dark conditions. However, most of the present denoising algorithms assume a Gaussian distribution for the measurement noise in image sensors. Hence, the denoising algorithms which serve low light conditions should be revised according to the behaviour of noise. The results of this chapter can be used to develop a more realistic chromatic denoising scheme for low light color measurement. Last but not least, the study of to what extent, and under what conditions these noises become visible to the human subjects should be investigated in future works.

CHAPTER 5
At Twilight: Mesopic Color Vision Models

In Chapters 3 and 4, we focused on cone responses and image sensor measurements at low light levels (mainly in the scotopic region). In this chapter, we study color vision models for simulating and rendering images in mesopic conditions. In relation to this, we consider two problems: first, simulating a mesopic scene and displaying it in photopic conditions; and second, rendering photopic scenes to be displayed in mesopic conditions. The solution to the first problem would be a mesopic color appearance model, and an *image retargeting algorithm* would be a general approach to address both problems. Mesopic color appearance models are needed in many advanced image processing algorithms such as tone reproduction techniques and color retargeting approaches. Many of the existing mesopic color appearance models do not perform very well (in terms of consistency with psychophysical measurements and reproduction of realistic mesopic colors) and are not able to handle noisy measurements.

In this chapter, we first compare some of the well-known mesopic vision models currently available in the literature. Then, we propose a noise-aware spectral color vision model for the mesopic range. All of these models are implemented, evaluated and compared to each other in the results section. One of the main purposes of this study is to illustrate the weaknesses and strengths of well-known mesopic models and

analyse their similarities and differences. Furthermore, this chapter aims at investigating the quality of tone mapping techniques (especially iCAM06) in reproducing mesopic scenes. Most of the existing tone mapping techniques do not do well in mesopic color reproduction.

Image retargeting approaches aim to provide a unified framework for image rendering in which both the intended scene luminance and the actual luminance of the display are taken into account. The remainder of this chapter is dedicated to introducing a new color retargeting approach for the mesopic range to be used in the image rendering pipeline of displays.

5.1 Proposed Method: Maximum Entropy Spectral Modeling Approach for Mesopic Vision

We saw in Chapter 3 that ideal cone responses in scotopic conditions become more uncertain. The spectral theory of color vision developed by Clark and Skaff [16] provides a tool to address the issues of uncertain measurements and estimating the spectral power distributions corresponding to these uncertain measurements in the photopic condition. In this section, this theory is extended to cover the mesopic and scotopic ranges as well. The flowchart of the proposed spectral color vision model in this work is shown in Fig. 5–1. The model is comprised of three interconnected parts: the spectral color appearance model, the CIE system for mesopic photometry, and the adaptation block, which are introduced in the following subsections.

5.1.1 Maximum Entropy Spectral Modeling Approach for Mesopic Vision

Clark and Skaff proposed a spectral model for color vision in [16] based on which we introduce a model for low light situations. We summarize the basic equations in

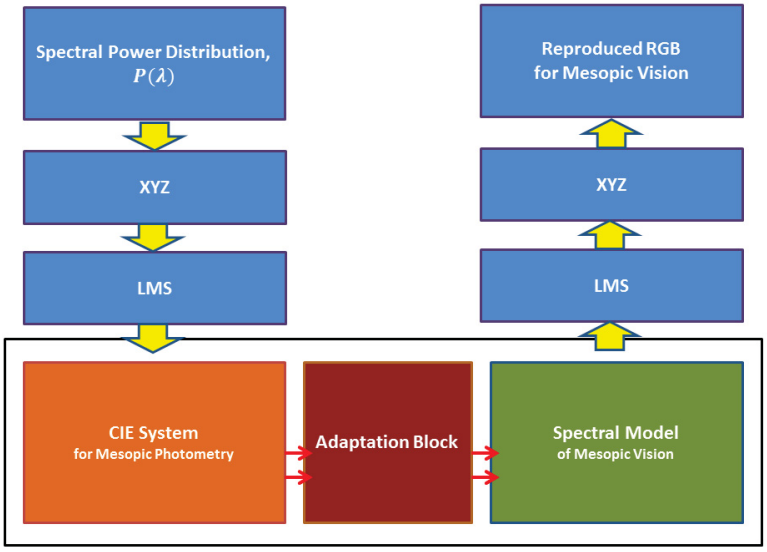

Figure 5–1: The flowchart of the proposed spectral mesopic color vision model

the following. We assume that the measurement is given by:

$$r = \beta \int_{\Lambda} f(\lambda)p(\lambda)d\lambda + \nu \tag{5.1}$$

where $f(\lambda)$ is the spectral profile of the imaging device, $p(\lambda)$ is the normalized spectral power distribution, ν represents the additive noise and Λ specifies the visible light spectrum range. Taking out the intensity factor, β, the normalized response will be:

$$\eta = \int_{\Lambda} f(\lambda)p(\lambda)d\lambda + \frac{\nu}{\beta}. \tag{5.2}$$

The response is normalized such that $\int p(\lambda)d\lambda = 1$. It has been shown that the maximum entropy estimation of the spectral power distribution, $\hat{p}(\theta, \lambda)$, belongs to

the exponential family:

$$\hat{p}(\theta, \lambda) = exp(< f(\lambda), \theta > -\psi(\theta)) \tag{5.3}$$

where <> defines the dot product of vectors $f(\lambda)$ and θ; additionally, $\psi(\theta)$ is a normalization function to ensure that $\int \hat{p}(\theta, \lambda) d\lambda = 1$. Then, the normalized measurement estimation can be obtained using the following formula:

$$\hat{\eta}(\theta) = \int_{\Lambda} f(\lambda) \hat{p}(\theta, \lambda) d\lambda. \tag{5.4}$$

It is worth mentioning that θ and $\hat{\eta}$ are dual coordinate systems for the exponential family and they relate to each other as follows [144].

$$\hat{\eta}(\theta) = \frac{\partial \psi(\theta)}{\partial \theta} \tag{5.5}$$

Given the noisy measurement η, the parameter θ can be obtained by solving an optimization problem:

$$\hat{\theta} = \underset{\theta}{\operatorname{argmin}} \{ (\hat{\eta}(\theta) - \eta)^T A (\hat{\eta}(\theta) - \eta) - \gamma H(\theta) \} \tag{5.6}$$

where A is a positive definite matrix, and $H(\theta)$ denotes the entropy function corresponding to $\hat{p}(\lambda)$. In the case of modeling the human visual system, the term $f(\lambda)$ refers to the cone spectral sensitivity functions. However, as mentioned before, the model for the mesopic condition will be slightly different, and we should modify the above model to make it appropriate for mesopic vision. In mesopic conditions, the cone and rod cells are both responsible for our vision. Hence, we modify equation 5.1

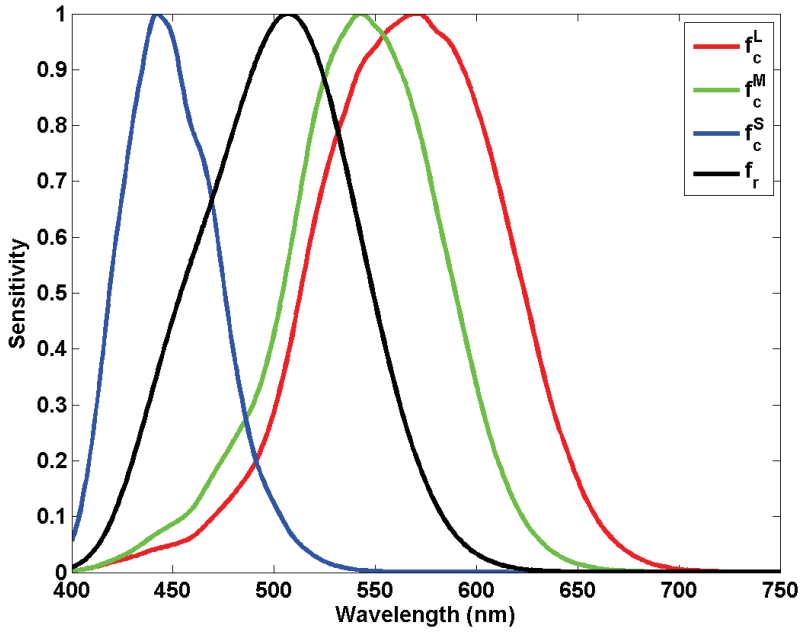

Figure 5–2: Plot of normalized cones and rods' spectral sensitivities based on the 2° data of Table 2 of [6].

to fit the new situation:

$$r^i = \beta_c \int_\Lambda f_c^i(\lambda) p(\lambda) d\lambda + \beta_r \int_\Lambda w^i f_r(\lambda) p(\lambda) d\lambda + \nu \qquad i \in \{L, M, S\}. \tag{5.7}$$

In this equation, β_c and β_r are coefficients determining the relative contribution of the cone and rod responses where $\beta_c + \beta_r = 1$, w^i specifies the relative weight of the rod output to each cone response, $f_c(\lambda)$ and $f_r(\lambda)$ are normalized cone and rod spectral sensitivity functions, respectively (see Fig. 5–2), and the superscript ^{i} specifies the type of cone cells. The above equation can be simplified as follows:

$$r^i = \beta_c \int_\Lambda [f_c^i(\lambda) + \xi w^i f_r(\lambda)] p(\lambda) d\lambda + \nu \qquad i \in \{L, M, S\} \tag{5.8}$$

where $\xi = \frac{\beta_r}{\beta_c}$. So, replacing $f(\lambda)$ with $f_{mes}(\lambda) = f_c(\lambda) + \xi W f_r(\lambda)$ in equation 5.1 will give us the spectral model for mesopic vision. In this equation, $W = diag(\left[w^L, w^M, w^S\right])$ is a diagonal matrix containing the w^i coefficients. The graphical representation of this model is shown in Fig. 5–3. It is worth mentioning that ξ may vary with the luminance level. However, one point is still unclear, which is how the γ and ξ should be defined. We address this issue using the new CIE system for mesopic photometry, which was presented in 2.4.1.1.

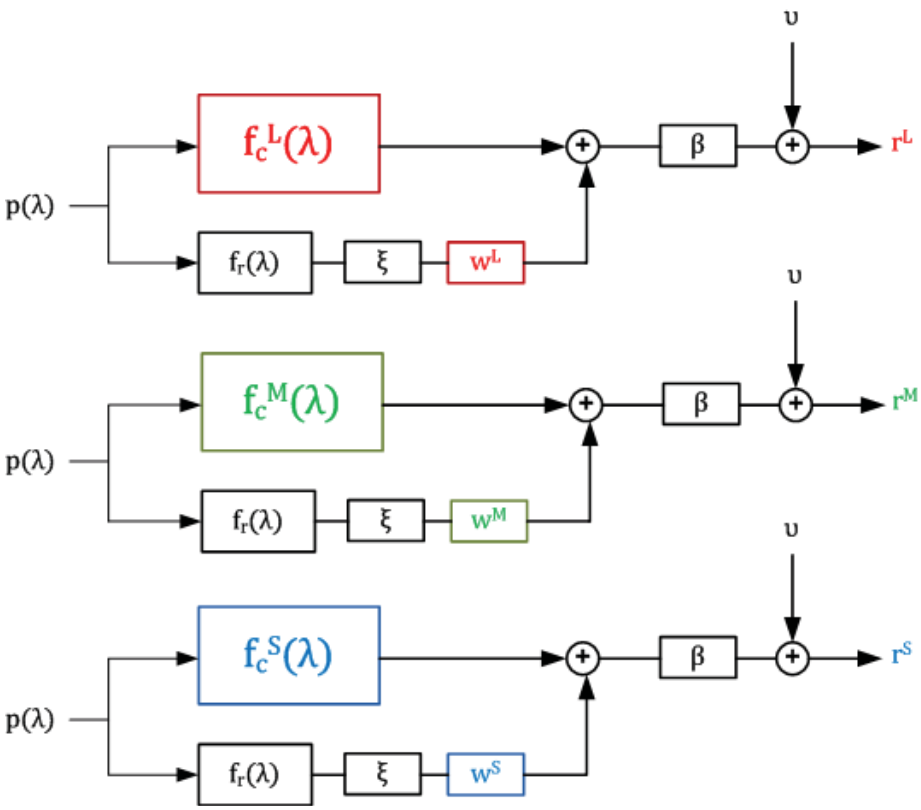

Figure 5–3: The schematic of the spectral theory of color vision for the mesopic range

5.1.2 CIE System for Mesopic Photometery

Taking advantage of the new CIE system for mesopic photometry, we can adjust the parameters of the spectral color appearance model by introducing an adapting factor as a function of the mesopic measure, m. This model is introduced in Section 2.4.1.1.

5.1.3 Adaptation Block

In the spectral mesopic color vision model, γ and ξ are adapting parameters which depend on the mesopic factor obtained from the CIE system for mesopic photometry. We can define γ and ξ as follows.

$$\begin{aligned} \gamma &= (1-m) \times c \\ \xi(m) &= \frac{e^{1-m}-1}{e-1} \end{aligned} \tag{5.9}$$

where c is a constant term for tuning purposes. Therefore, the CIE system for mesopic photometry can be employed in mesopic color appearance models; however, to find the mesopic luminance the major limitation is that the photopic and scotopic luminance values need to be given.

5.2 Results and Discussion

5.2.1 Materials and Methods

In this section, we simulate a number of well-known mesopic models introduced in sections 2.4.2.1 to 2.4.2.5 in order to compare them and discuss their performance. In this regard, we designed a prototype that includes all the aforementioned models together with the proposed spectral mesopic color vision model. Using the prototype, we can simulate Munsell patches surrounded by a white background viewed under

different light levels from scotopic conditions to fully photopic situations. The aim of this prototype is to provide a framework in which we can compare the output of different mesopic models in various light intensities simultaneously. We take advantage of the new CIE system for mesopic photometry to calculate the mesopic factor and the mesopic luminance value. The parameters of different models are chosen based on the settings recommended in the original articles. The parameters of the spectral model are specified as: $W = \text{diag}([3\ 3\ 5])$ and $c = 2$. The standard D65 illuminant is selected to render the white point. We should note that in implementing iCAM06, the surround adjustment and colorfulness adjustment are disabled, because they do not correspond to the mesopic color appearance performance of this model. A snapshot of the implemented prototype is shown in Fig. 5–4. The upper left patch is the reference color patch in the fully photopic condition. The remaining color patches depict the appearance of the patch under mesopic vision as displayed in the photopic condition (i.e. the intensity of the white point is mapped to 255.)

5.2.2 Scenario I: Evaluating Mesopic Color Vision Models on a Single Patch

In the first test scenario, the outputs of different methods are compared relative to each other for a single Munsell patch, called "10GY 60/10", when the light source has the equi-energy spectrum. Models are evaluated under 14 luminance values ranging from 0.002 to 1000 cd/m^2. Fig. 5–5 shows the examined light intensities and the corresponding mesopic measures. The chromaticities of the output of each model under the range of light intensities are shown in Fig. 5–6. The output of each model shows the photopic-rendered appearance (i.e. the mesopic appearance of the color patch is simulated on a photopic display) of the original color patch

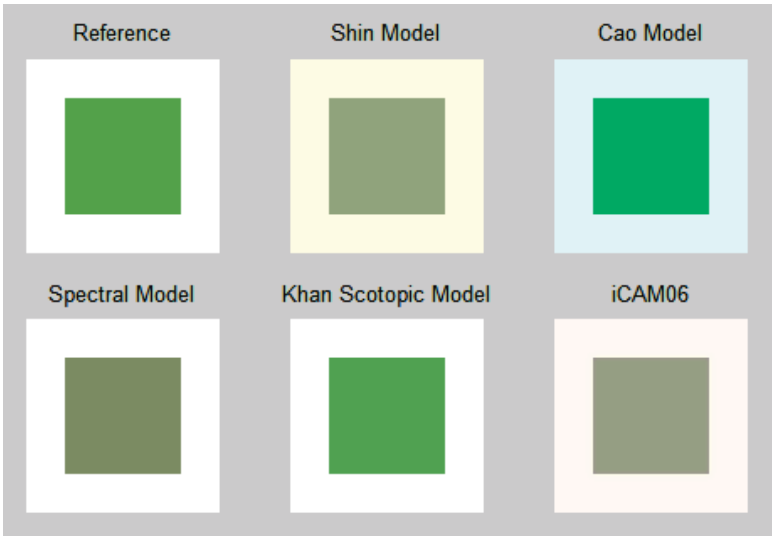

Figure 5–4: A snapshot of the implemented prototype for the luminance of 0.3 cd/m^2 where the mesopic factor $m = 0.6$. (Please be advised that the output colors are represented in the sRGB space and the effect of the display on the appearance of color patches is not considered here.)

when it is viewed under a given light level by the standard human observer. The output chromaticity values of the iCAM06, Cao and Khan models vary along a line in the xy-chromaticity diagram, because these models assume that the rod responses are linearly added to the cone responses. It should be noted that the Cao model produces negative chromaticity values, which are not physically plausible, in the far end of the mesopic region (close to the scotopic range) and the scotopic region. As we go further through the mesopic region toward the scotopic range, the output chromaticities of the iCAM06, Shin and spectral mesopic color vision models get closer to the achromatic region of the chromaticity diagram; however, the Khan model approaches the bluish region inside the chromaticity diagram.

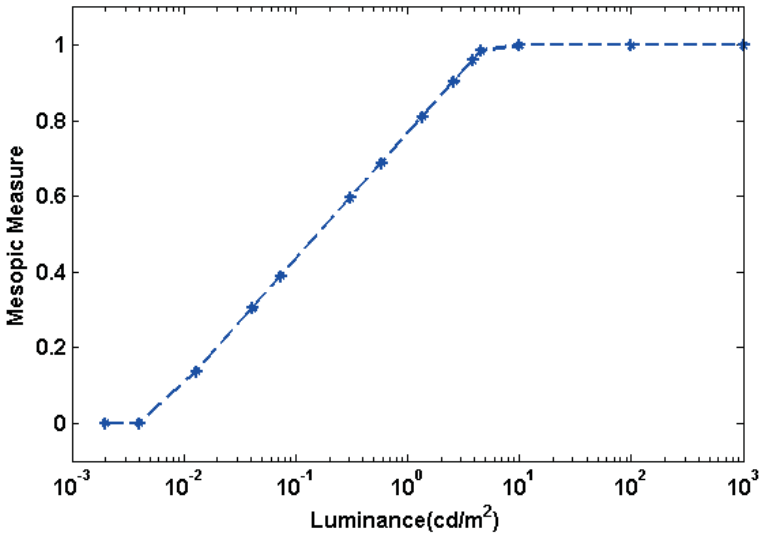

Figure 5–5: Luminance values and the corresponding mesopic measure considered in scenario I

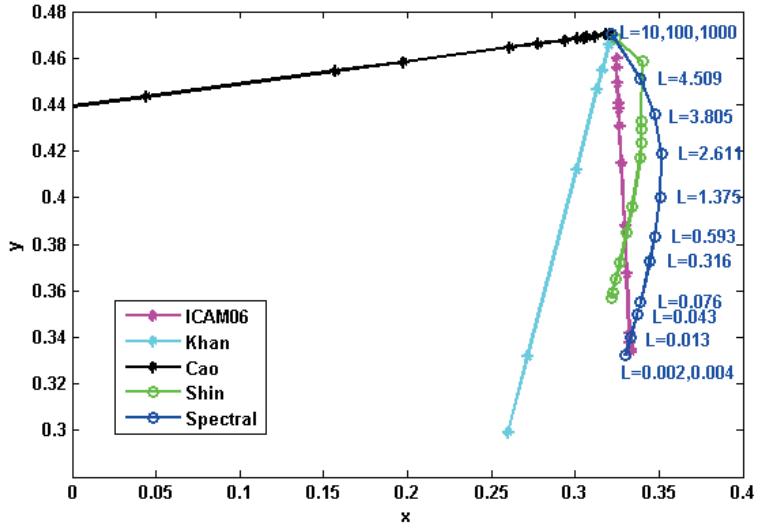

Figure 5–6: Output of different models for the "10GY 60/10" Munsell patch under different luminance levels.

Table 5–1: Mean mutual color differences of the mesopic models under given luminance values

	Shin	Spectral	iCAM	Cao	Khan
Shin	0	**9.14**	**10.15**	256.33	24.75
Spectral		0	**15.78**	254.48	21.64
iCAM			0	254.07	24.53
Cao				0	240.07
Khan					0

Table 5–1 tabulates the mean mutual ΔE_{ab} chromaticity differences computed for all the model pairs to compare their photopic representation of the simulated color patch over the range of light intensities. In this regard, we can say that the Shin, iCAM06, and the spectral models are fairly close to each other. Additionally, based on the fact that the Cao model generates invalid chromaticity responses (close to the scotopic range), we may expect large color differences between it and the other models. If we consider the Shin model as a reference (since it is obtained through psychophysical experiments), we can say that the spectral model does fairly well in terms of modeling mesopic vision, because the spectral mesopic color vision model is closer to the Shin model, from the ΔE_{ab} point of view, compared to the other models. The main difference between both the spectral and Shin models and the iCAM model is that the former models treat the rod response in a nonlinear way while the latter assumes a linear contribution of the rod response to the mesopic vision. Bear in mind that the linear assumption holds for the Cao and Khan models as well.

5.2.3 Scenario II: Evaluating the Overall Performance of Mesopic Models

In the second scenario, we carried out the same evaluation process as the first test over a set of chosen Munsell patches covering various hue angles (as Shin suggested in [65]). In this scenario, we limit ourselves to the three best models: the Shin model, the spectral model and iCAM06. The list of the Munsell color patches involved in this scenario can be found in Table 3–1.

First, we investigate the effect of selecting the mesopic measure as an adaptive factor in the spectral model. Figure 5–7 shows a case in which a spectral model without using the mesopic measure in the γ adjustment is compared with the spectral model introduced in scenario I. This figure shows that without using the mesopic measure, this model cannot deal with the photopic situations satisfactorily and it outputs desaturated colors. Mean mutual color differences are calculated for the three selected models, where the spectral model is substituted with the non-adaptive version with $\gamma = 2$ (see Table 5–2). The results imply that the non-adaptive spectral mesopic color vision model produces results that are quite different from the other two models: iCAM and Shin. Second, we compare the performance of the three selected mesopic models dealing with 10 different patches under 14 different light intensities, as shown in Fig. 5–5. Fig. 5–8 depicts the results in the xy-chromaticity diagram. The output chromaticities of the spectral mesopic color vision model reflects the nonlinearities of mesopic vision better than iCAM06. Bear in mind that in the scotopic range, our work and the iCAM06 model give rise to, more or less, similar achromatic perception; however, the Shin model tends towards a greenish percept in that condition.

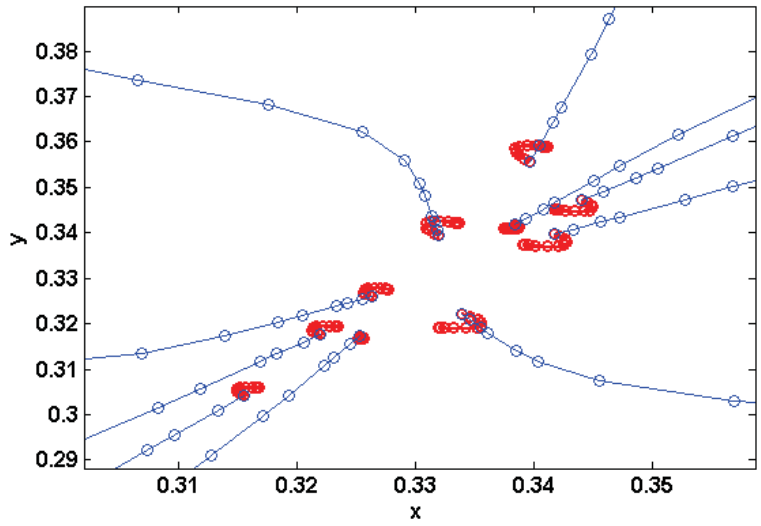

Figure 5–7: Investigating the effect of adaptation term in the spectral model: The red circles indicate the output of the spectral model when $\gamma = 2$ and no adaptation term is used, while the blue circles depict the spectral model with the same adjustment as the first experiment.

5.3 A Color Retargeting Approach for Mesopic Vision

Retargeting approaches aim at providing a unified framework for image rendering in which both the intended scene luminance and the luminance of the display are taken into account (read Section 2.5.2). At the core of any color retargeting method, a color appearance model and its inverse are employed. Such a color appearance model should therefore be invertible and cover the entire luminance range of the human visual system. There are not many available models which meet these two conditions. Moreover, most of these models were developed based on psychophysical experiments on simple color patches, and they are not suitable to be used for complex images. In this section, a color retargeting approach based on the mesopic model of Shin et al. [65] is developed to work with complex images. In this regards,

Table 5–2: Mean mutual ΔE_{ab} color differences calculated when the spectral model does not include the adaptive term as a function of the mesopic measure

	Shin	Spectral	iCAM
Shin	0	**17.91**	**10.15**
Spectral (no adaptation)		0	**23.24**
iCAM			0

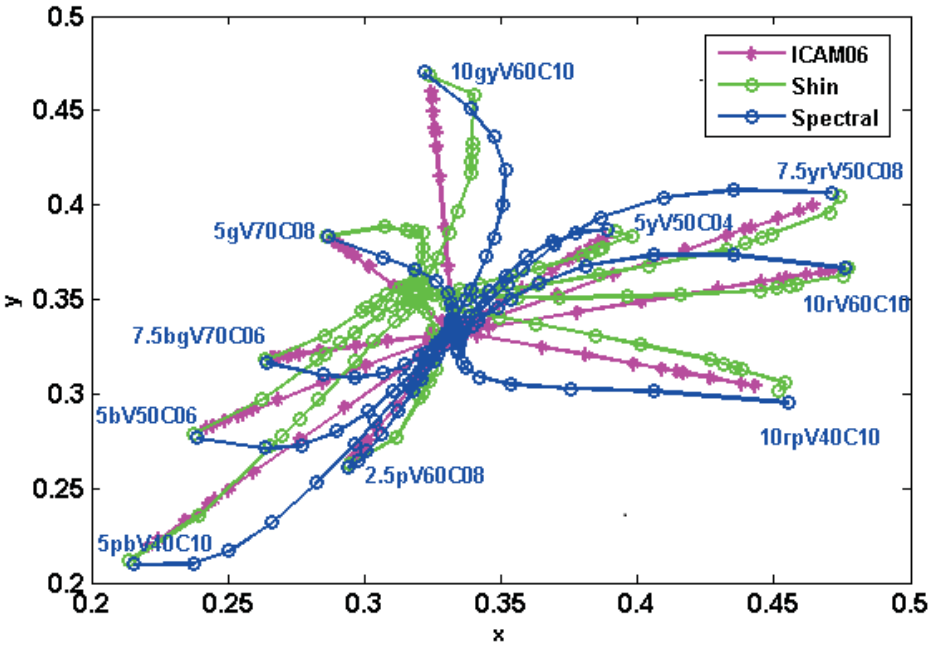

Figure 5–8: The output of the iCAM, Shin and Spectral models for 10 different Munsell color patches under various luminance values.

we derive the inverse for the Shin model to compensate for color appearance changes on displays dimmed to the mesopic range and viewed in a dark environment. We evaluate this method using quantitative approaches and the results show a discriminative improvement in the simulated perceived color quality for mesopic vision. The

proposed method can be incorporated into image retargeting techniques and display rendering mechanisms.

We made the following assumptions in the proposed algorithm: first, the display should be viewed with a dark surround and the influence of the surround is not considered in the color vision model; second, the model does not take the size of stimuli into account; and third, spatial and temporal properties of the human visual system are not addressed (i.e. pixels are treated as independent in the image). Hence, the proposed framework can be combined with image retargeting methods [2] to model our visual mechanisms more thoroughly.

5.3.1 Shin's Color Appearance Model for Mesopic Vision

Shin et al. proposed a modified version of the Boynton two-stage model with fitting parameters to account for the rod intrusion in mesopic vision [65]. The goal of the model is to find the matching colors in the photopic range for the input colors in the mesopic range. The parameters of the model are obtained as a function of luminance based on the asymmetric color matching experimental data. In their experiment, the observer is presented with a Munsell color chip under the mesopic condition and is asked to match the appearance of that patch with the simulated image reproduced by this model on the CRT display under photopic conditions. The model is as follows:

1. The XYZ image (i.e. the linear RGB image which is transformed to the XYZ color space) is input to the model and is converted to the LMS space.

$$
\begin{aligned}
[X\ Y\ Z]^t &= M_{rgb2xyz} \cdot [R\ G\ B]^t \\
LMS = [L_p\ M_p\ S_p]^t &= M_{xyz2LMS} \cdot XYZ
\end{aligned}
\tag{5.10}
$$

2. The LMS signals are then substituted into the opponent channel equations of the Boynton two-stage model [113]:

$$
\begin{aligned}
A(E) &= \alpha(E) K_w((L_p + M_p)/(L_{pw} + M_{pw})) \\
&\quad + \beta(E) K'_w (Y'/Y'_w)^\gamma \\
r/g(E) &= l(E)(L_p - 2M_p) + a(E)Y' \\
b/y(E) &= m(E)(L_p + M_p - S_p) + b(E)Y'
\end{aligned}
\tag{5.11}
$$

where E represents the scene photopic luminance, $A(E), r/g(E),$ and $b/y(E)$ are achromatic, red/green and blue/yellow opponent responses respectively; the indices p and w indicate "photopic" and "white point", respectively; Y' represents the scotopic luminance; $\alpha(E), \beta(E), l(E), a(E), m(E),$ and $b(E)$ are the fitting functions indicating the relative contribution of the rod's response to the opponent channels; and K_w and K'_w are the maximum responses of the luminance channel at photopic and scotopic conditions, respectively.

3. Then, the opponent responses, $A(E), r/g(E)$, and $b/y(E)$, are transformed back to the XYZ space and then to the RGB space.

$$
[X_m\ Y_m\ Z_m]^t = M_{opp2xyz} \cdot [A(E)\ \ r/g(E)\ \ b/y(E)]^t \tag{5.12}
$$

Table 5–3: Parameters of the Shin model

Parameter	value
K_w	1
K'_w	78.4
γ	0.77

Table 5–4: Transformation matrices used in the Shin Model

Parameter	value
$M_{rgb2xyz}$, [145]	$\begin{bmatrix} 0.4124 & 0.3576 & 0.1805 \\ 0.2126 & 0.7152 & 0.0722 \\ 0.0193 & 0.1192 & 0.9505 \end{bmatrix}$
$M_{xyz2LMS}$, [65]	$\begin{bmatrix} 0.155 & 0.543 & -0.033 \\ -0.155 & 0.457 & 0.033 \\ 0 & 0 & 1 \end{bmatrix}$
$M_{opp2xyz}$ [65]	$\begin{bmatrix} 1.008 & 2.149 & -0.212 \\ 1 & 0 & 0 \\ 1 & 0 & -1 \end{bmatrix}$

where X_m, Y_m, and Z_m represent the mesopic simulated version of the XYZ input to be viewed in photopic conditions. The parameters of the Shin model are selected according to Table 5–3. Functions ($\alpha(E)$, $\beta(E)$, $l(E)$, $a(E)$, $m(E)$, $b(E)$) are evaluated based on interpolation over the given points in Table 1. of [65]. The transformation matrices used in the model are listed in Table 5–4.

5.3.2 Developing the inverse of Shin's model

As mentioned earlier, perceptual rendering necessitates involving both a color vision model and its reverse. Given the intended luminance of the original image, the forward color appearance model - the Shin model in our case- predicts the color perceptual attributes for a standard human observer. The goal of the inverse model is to take the output of the forward model (the simulated perceived original image

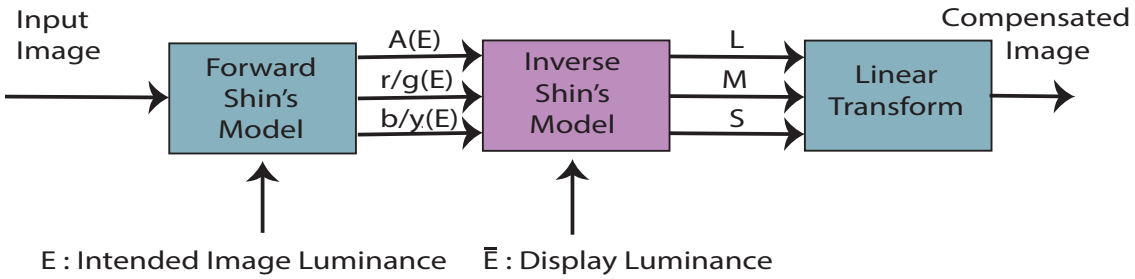

Figure 5–9: Schematic of the color retargeting method

at the intended luminance based on the Shin model) and predict the RGB values of the compensated image such that the color appearance of this image rendered on a display with a specific luminance value resembles the perceived original image. Hence, in order to develop the inverse model, we feed the color perceptual attributes of the forward model into the inverse model (i.e. the inverse Shin's model) along with the luminance of the target display and obtain the compensated image to be rendered on the display. The schematic of this perceptual model is shown in Fig.5–9.

To develop the inverse of this nonlinear color vision model we carry out the following steps:

First, the opponent responses of the forward model ($A(E)$, $r/g(E)$, $b/y(E)$) are fed to the inverse model. We assume that the compensated image based on the display luminance, $\overline{E}$, produces the same opponent responses as the opponent responses of the forward model to make a perfect match to the perceived image at the intended luminance, E.

Second, the functions: $\alpha(\overline{E}), \beta(\overline{E}), l(\overline{E}), a(\overline{E}), m(\overline{E}),$ and $b(\overline{E})$ are evaluated for the

average display luminance, $\overline{E}$.

Third, the computed functions and opponent responses are substituted in the forward model (Eq. 5.11) and the $\overline{LMS}$ values of the compensated image can be obtained as follows:

$$\begin{aligned}
\overline{L_p} + \overline{M_p} &= ((L_{pw} + M_{pw})/(\alpha(\overline{E})K_w)) \times \\
&\qquad (A(E) - \beta(\overline{E})K'_w(Y'/Y'_w)^\gamma) \\
\overline{L_p} - 2\overline{M_p} &= \frac{(r/g(E) - a(\overline{E}) \times Y')}{l(\overline{E})} \\
\overline{L_p} + \overline{M_p} - \overline{S_p} &= \frac{(b/y(E) - b(\overline{E}) \times Y')}{m(\overline{E})}.
\end{aligned} \tag{5.13}$$

Fourth, the left hand side variables of Eq. 5.13 are transformed to $\overline{L_p}$, $\overline{M_p}$, and $\overline{S_p}$ using a simple linear transformation.

$$\begin{bmatrix} \overline{L_p} \\ \overline{M_p} \\ \overline{S_p} \end{bmatrix} = \begin{bmatrix} 1 & 1 & 0 \\ 1 & -2 & 0 \\ 1 & 1 & -1 \end{bmatrix}^{-1} \times \begin{bmatrix} \overline{L_p} + \overline{M_p} \\ \overline{L_p} - 2\overline{M_p} \\ \overline{L_p} + \overline{M_p} - \overline{S_p} \end{bmatrix} \tag{5.14}$$

And finally, a linear transformation is applied to convert the $\overline{LMS}$ values to XYZ and subsequently to RGB values. Figure 5–10 depicts the schematic of the proposed inverse Shin model.

5.4 Results and Discussion

In this section, the proposed color retargeting algorithm is evaluated using quantitative experiments.

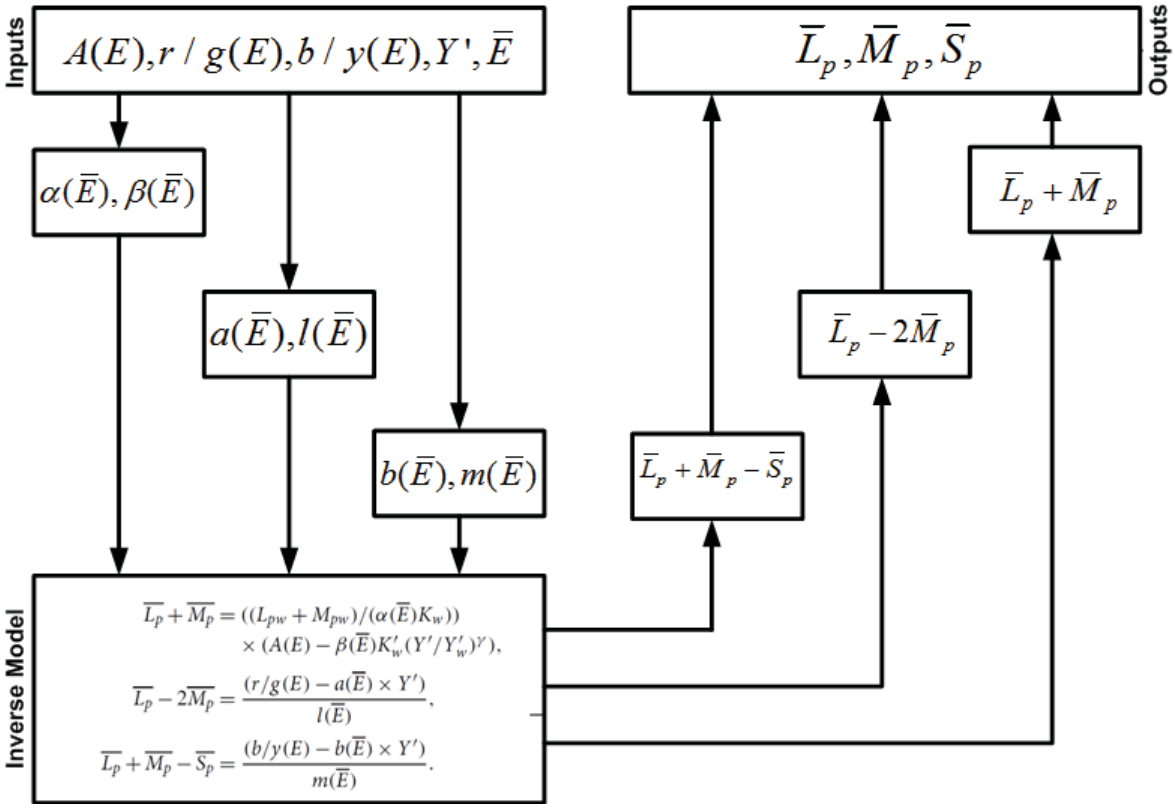

Figure 5–10: Schematic of the inverse Shin color retargeting method

5.4.1 Scenario I: Quantitative Evaluation

In the quantitative evaluation, the human subject is replaced by the Shin mesopic model to predict the human observer's color perception at low light levels. The evaluation procedure is depicted in Fig. 5–11. The forward Shin model is employed to simulate the perceived image at different luminance levels. This model takes in an image, the reference white and the light level under which the image is viewed. The output of the model is the simulated perceived image at photopic conditions in the XYZ space. To derive the corresponding color perceptual attributes, the XYZ values and the reference white can be given in the CIELab space.

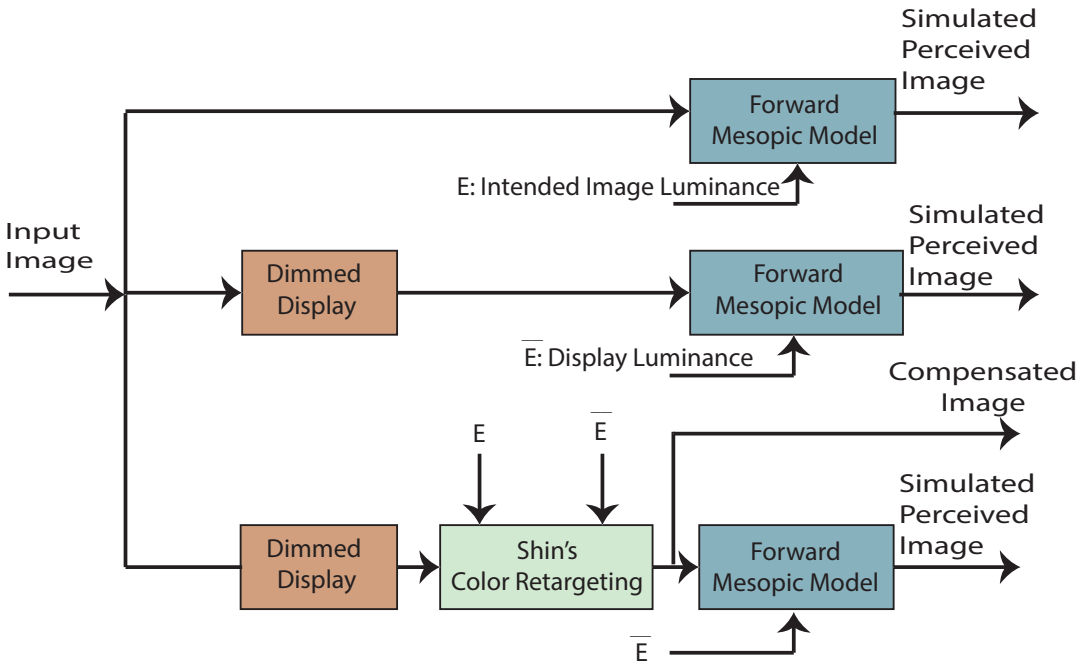

Figure 5–11: The procedure for evaluating the proposed Shin color retargeting method: the simulated perceived image at the intended scene luminance, E, is compared to the simulated perceived image viewed on a dim display (in the mesopic range) with the luminance $\overline{E}$ when no processing is done to the image and the simulated perceived image processed by our color retargeting method viewed on the same display.

This experiment is conducted on 4 images: {Multi-object Scene, Car, Walk Stones, Red Room} where the images are viewed in a dark surround. The results are shown in Figs. 5–12-5–15. Each of the figures shows: (a) the simulated perceived original image on a bright display ($L_{src} = 250cd/m^2$), (b) the simulated perceived unprocessed image on a dark display ($L_{dest} = 2cd/m^2$), (c) the simulated perceived compensated image on a dark display with the same brightness level, (d) the compensated image, (e) the simulated perceived gamut of the image shown in (a), (f)

the simulated perceived gamut of the unprocessed image on a dark display, (g) the simulated perceived gamut of the compensated image viewed on a dark display, and (h) the comparison of the three simulated perceived gamuts depicted in (e), (f), and (g). It is worth mentioning that the gamut of each image is shown in the LAB space, which is approximately a perceptually uniform color space.

The results shown in Figs. 5–12 to 5–15 demonstrate that the compensated image has a larger simulated perceived gamut and a better simulated color appearance at dark conditions as compared to the unprocessed image viewed at the same condition. For example, in the *Multi-object Scene* image in Fig. 5–12, you may compare the checker board colors in Fig. 5–12-(b) and 5–12-(c) to see that the colors in the simulated perceived compensated image more resemble the colors in Fig. 5–12-(a); or in the *Car* image, the blue color of the sky and the car is maintained better as compared with the unprocessed image on the dark display. The simulated perceived unprocessed *Walk Stone* image shows washed out colors while in the simulated perceived compensated image, the blue sky, green grass and brown stones are more clearly visible. Figure 5–14-(h) demonstrates that the simulated perceived gamut of the unprocessed image in dark conditions has shrunk to the center of the *ab*-chromaticity diagram (achromatic region) and the simulated perceived gamut of the compensated image brings back a fairly large portion of the lost simulated perceived color gamut. In Fig. 5–15, the red color of the wall, carpet and the vase, the color of the cushions and the picture hung on the wall are more vivid in the dark compensated image compared to the unprocessed image.

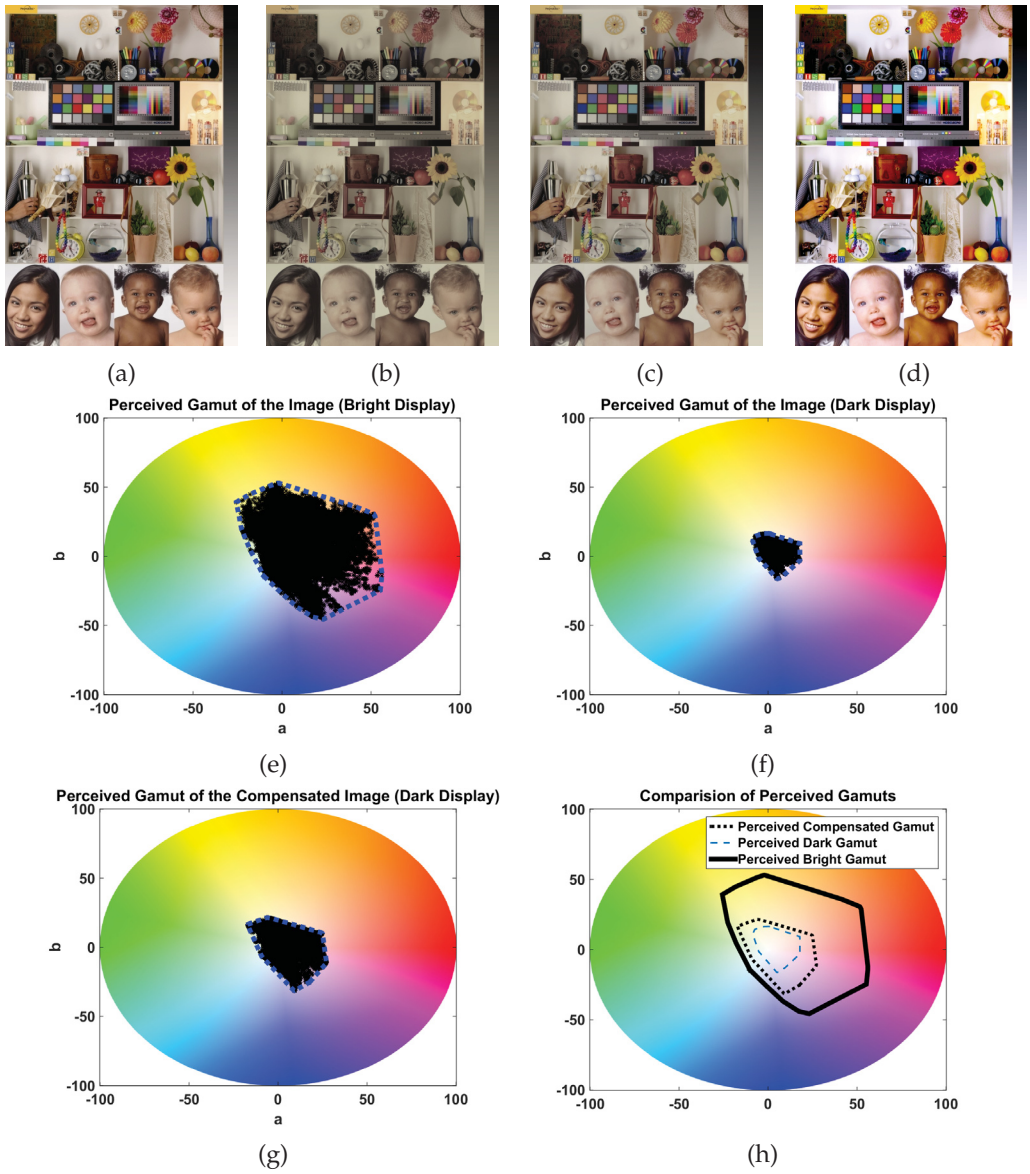

Figure 5–12: The reverse Shin model is tested based on the evaluation schematic shown in Fig. 5–11. (a) Perceived colors in the Original Scene ($L_{source} = 250cd/m^2$) (b) Perceived colors on a dimmed display ($L_{dest} = 2cd/m^2$) (c) Perceived colors of the compensated image ($L_{dest} = 2cd/m^2$) (d) Compensated image (rendered on the display) ($L_{dest} = 2cd/m^2$) (e) Gamut of the original scene (f) Gamut of the simulated perceived image on a dimmed display (g) Simulated perceived gamut of the compensated image (h) Comparison of simulated perceived gamuts [7]

(a) Simulated perceived colors in the Original Scene ($L_{source} = 250cd/m^2$)

(b) Simulated perceived colors on a Dimmed Display ($L_{dest} = 2cd/m^2$)

(c) Simulated perceived colors of Compensated Image ($L_{dest} = 2cd/m^2$)

(d) Compensated image (rendered on the display) ($L_{dest} = 2cd/m^2$)

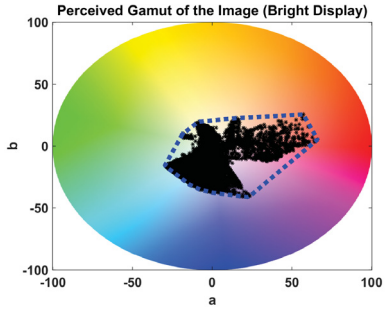

(e) Simulated perceived gamut of the original scene

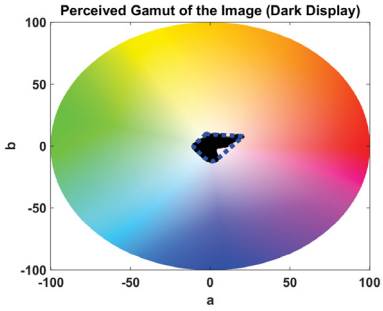

(f) Gamut of simulated perceived image on a dimmed display

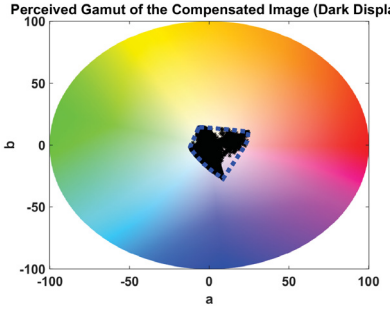

(g) Simulated perceived gamut of compensated image

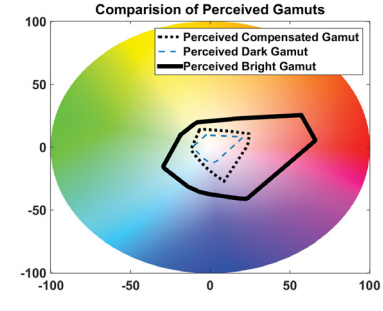

(h) Comparison of simulated perceived gamuts

Figure 5–13: The reverse Shin model is tested based on the evaluation schematic shown in Fig. 5–11 [7].

(a) Simulated perceived colors in the Original Scene ($L_{source} = 250cd/m^2$)

(b) Simulated perceived colors on a Dimmed Display ($L_{dest} = 2cd/m^2$)

(c) Simulated perceived colors of Compensated Image ($L_{dest} = 2cd/m^2$)

(d) Compensated image (rendered on the display) ($L_{dest} = 2cd/m^2$)

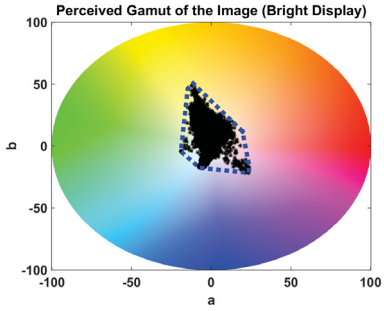

(e) Simulated perceived gamut of the original scene

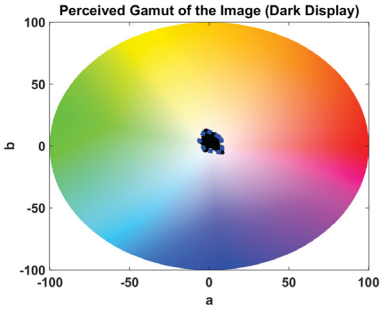

(f) Gamut of simulated perceived image on a dimmed display

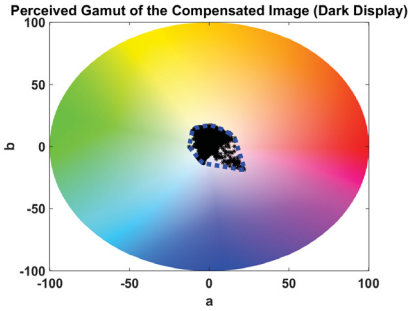

(g) Simulated perceived gamut of compensated image

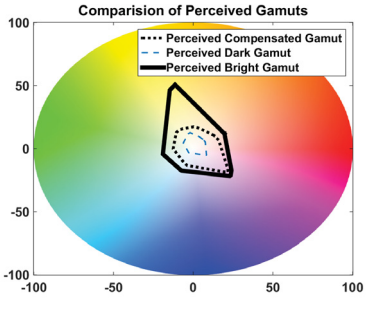

(h) Comparison of simulated perceived gamuts

Figure 5–14: The reverse Shin model is tested based on the evaluation schematic shown in Fig. 5–11 [7].

(a) Simulated perceived colors in the Original Scene ($L_{source} = 250cd/m^2$)

(b) Simulated perceived colors on a Dimmed Display ($L_{dest} = 2cd/m^2$)

(c) Simulated perceived colors of Compensated Image ($L_{dest} = 2cd/m^2$)

(d) Compensated image (rendered on the display) ($L_{dest} = 2cd/m^2$)

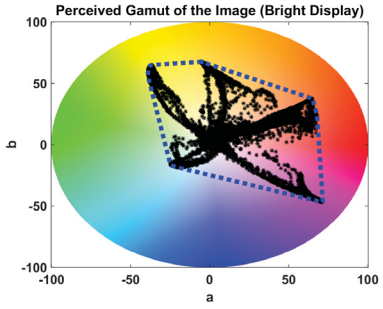

(e) Simulated perceived gamut of the original scene

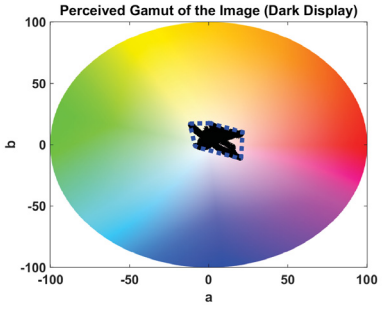

(f) Gamut of simulated perceived image on a dimmed display

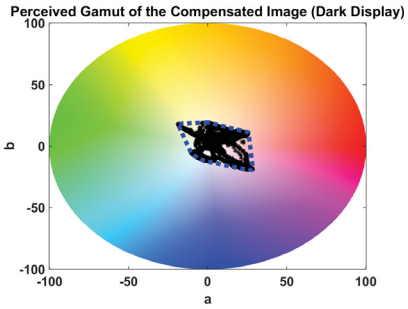

(g) Simulated perceived gamut of compensated image

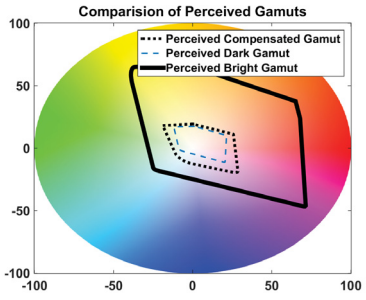

(h) Comparison of simulated perceived gamuts

Figure 5–15: The reverse Shin model is tested based on the evaluation schematic shown in Fig. 5–11 [7].

To evaluate the color appearance quality of images quantitatively, a color difference metric can be employed. A particular application of the quantitative assessment techniques is to replace a human subject in evaluating the quality of images, and accordingly, gives rise to a less expensive, more effective, more repeatable and consistent, and more time efficient approach. The metric used for this purpose should be based on a comprehensive color appearance model. There are several color difference measures in the literature such as ΔE_{xy}, ΔE_{ab}, ΔE_{94}, and ΔE_{00}; however, none of them gives an ideal perceptual measure to be used with complex images. In spite of the reported limitations and deficiencies of these measures, they are the only available metrics for quantitative color quality assessment and have been used in the literature extensively. Hence, the quantitative evaluation of our method is done as follows.

The chromaticity difference measure, ΔE^c_{94}, is derived from the well-known color difference metric, ΔE_{94} by removing the lightness component from the ΔE_{94} formula. ΔE^c_{94} is used to evaluate the chromaticity deviation of simulated perceived uncompensated and compensated images on the dimmed display compared to the perceived colors of the original scene.

$$\Delta E^c_{94} = \sqrt{(\frac{\Delta C^*_{ab}}{k_C S_C})^2 + (\frac{\Delta H^*_{ab}}{k_H S_H})^2} \tag{5.15}$$

where

$$
\begin{aligned}
&C_1^* = \sqrt{(a_1^*)^2 + (b_1^*)^2}, C_2^* = \sqrt{(a_2^*)^2 + (b_2^*)^2} \\
&\Delta C_{ab}^* = C_1^* - C_2^* \\
&\Delta a^* = a_1^* - a_2^*, \Delta b^* = b_1^* - b_2^* \\
&\Delta H_{ab}^* = \sqrt{(\Delta a^*)^2 + (\Delta b^*)^2 - (\Delta C_{ab}^*)^2} \\
&S_C = 1 + K_1 C_1^*, S_H = 1 + K_2 C_1^*
\end{aligned}
\tag{5.16}
$$

and where (a_1^*, b_1^*) and (a_2^*, b_2^*) refer to the a^*b^* values of two CIE 1976 $L^*a^*b^*$ coordinates, K_1 is set to 0.045, $K_2 = 0.015$, and $k_C = k_H = 1$ [63].

The results of the perceptual chromaticity difference between the dark and bright image for both uncompensated and compensated approaches of Figs. 5–12-5–15 are shown in Table 5–5. The ΔE_{94}^c measure of compensated images is reduced by almost a factor of 2 as compared to that of the uncompensated images.

Another quantitative measure, which is introduced in this work, is the percentile coverage of the simulated perceived gamut of images at dark relative to the simulated perceived gamut of the bright image (i.e. the proportion of the overlapping area of the simulated perceived gamut of the dark image to the simulated perceived gamut of the original bright image.) In the rest of the chapter, we refer to this measure as the Effective Gamut Ratio (EGR). The EGR index is used to evaluate the performance of our proposed method on compensating the shrunk gamut area of the simulated perceived unprocessed image and the results are reported in Table 5–6. The EGR measure is shown to be almost two times bigger for the compensated images with

our method as compared to the unprocessed ones; and the EGR of the *Walk Stones* image is enhanced by a factor of 4.

Figure 5–16 shows the ΔE^c_{94} and EGR indices of the four images at different display luminance values: 1, 2, 5, and 10 cd/m^2. We can summarize the results as follows: first, the perceptual difference of compensated images is smaller than that of unprocessed images for all examined luminance values; second, the ΔE^c_{94} measure decreases as the display luminance grows; third, our proposed method covers a greater portion of the simulated perceived gamut of the original image compared to the unprocessed one; and fourth, the EGR index increases with respect to the display luminance.

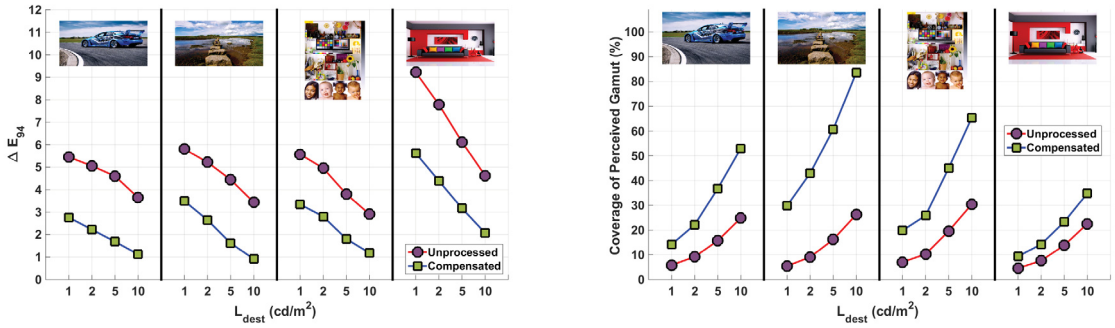

(a) (b)

Figure 5–16: The ΔE^c_{94} measure and the EGR index are evaluated for the unprocessed and compensated images at different display luminance levels: 1, 2, 5, and 10 cd/m^2.

5.4.2 Scenario II: Comparing with Other Methods

In this scenario, we compare the performance of different algorithms in terms of their ΔE^c_{94} and EGR indices. The results are shown in Table 5–5 and Table 5–6.

5.4.2.1 Experimental Methods

In this scenario, the following methods are evaluated:

Our color retargeting method: is based on the forward and inverse of the Shin mesopic model introduced in this chapter as a color retargeting approach in Fig. 5–9.

The Wanat color retargeting approach [2] is proposed by Wanat and Mantiuk. In this algorithm, the Cao algebraic model and its inverse are employed in the retargeting method. This algorithm is implemented and used for processing images as described in [2].

iCAM06 is one of the most well-known image appearance methods in the literature [119]. The input parameters of this model are set as: maximum luminance, $max_L = 2$ (cd/m^2); overall contrast, p = 0.7; and surround adjustment, $gamma_{value}$=1.

A set of 5 images is added to our image set for this test, shown in column (a) of Fig. 5–17. The images are selected such that they span a range of colors: red, green, blue, yellow, purple, orange, and brown. Figure 5–17 depicts the output of the different models. Columns (b), (c), and (d) show the result of applying the Wanat color retargeting model, iCAM06, and our method, respectively.

5.4.2.2 Discussion

In this subsection, we compare the quantitative performance of the introduced methods on the image set based on the ΔE^c_{94} and EGR indices. Table 5–5 and Table 5–6 summarize the quantitative results of the methods. The two tables show the superiority of our proposed method over the other discussed techniques. Table 5–6 shows that the gamut coverage of our method varies over the images, since the

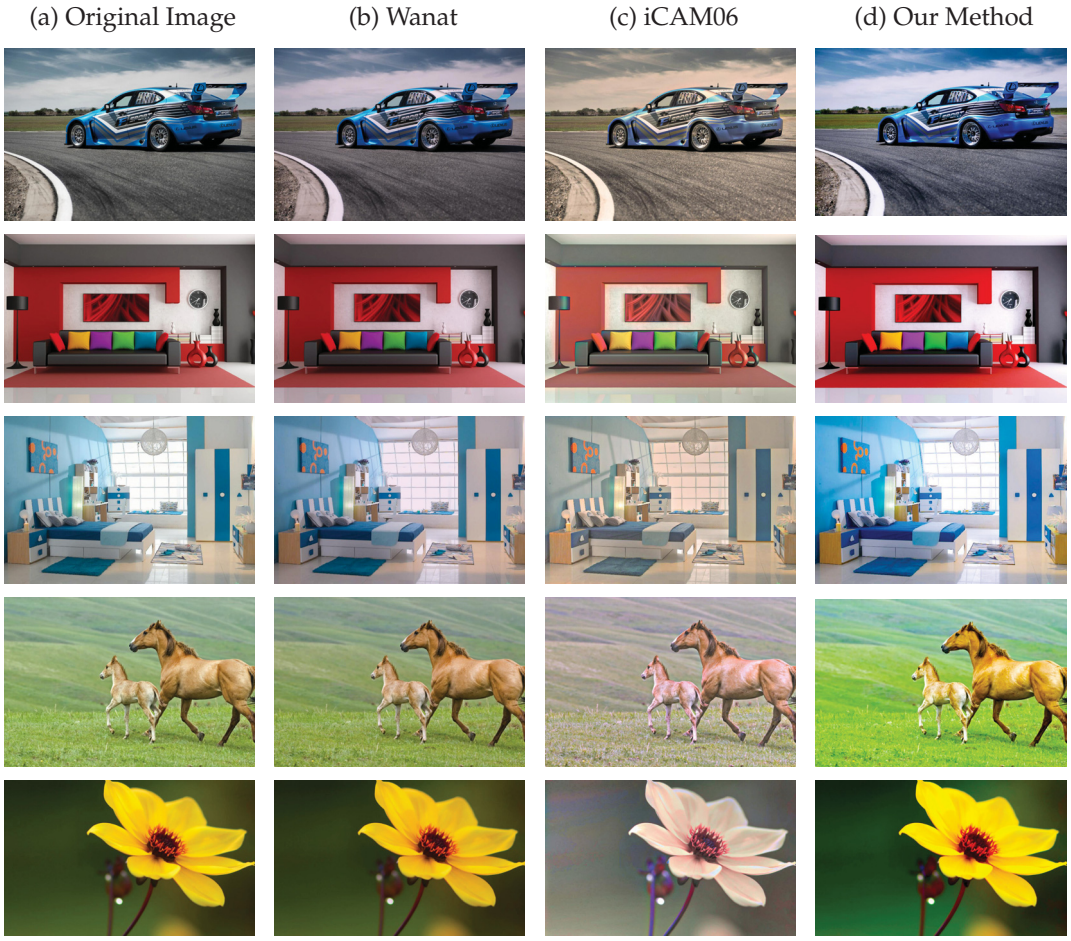

Figure 5–17: The original images and the results of different approaches applied to each image are shown. Images are processed for $L_{src} = 250$ cd/m^2 and $L_{dest} = 2$ cd/m^2 [7].

Table 5–5: Mean ΔE^c_{94} measure between a test image viewed at $L_{dest} = 2\ cd/m^2$ and the perceived original image at $L_{src} = 250\ cd/m^2$

Test Image	Unprocessed	Our Method	Wanat	iCAM06
Multi-object Scene	5.0	**2.80**	4.37	5.62
Car	5.05	**2.23**	4.36	7.23
Walk Stones	5.22	**2.65**	4.54	5.74
Red Room	7.79	**4.39**	7.09	7.42
Blue Room	6.19	**3.36**	5.43	8.26
Horse	6.58	**3.45**	7.17	10.93
Flower	23.61	**21.17**	24.15	31.13

Table 5–6: The EGR index (the percentile coverage of the perceived gamut (%)) between a test image viewed at $L_{dest} = 2\ cd/m^2$ and the perceived original image at $L_{src} = 250\ cd/m^2$

Test Image	Unprocessed	Our Method	Wanat	iCAM06
Multi-object Scene	10.3	**25.9**	12.0	9.9
Car	9.2	**22.1**	10.2	10.0
Walk Stones	9.1	**43.0**	14.8	20.5
Red Room	7.6	**14.3**	7.7	9.9
Blue Room	13.5	**36.3**	14.8	17.7
Horse	9.7	**25.8**	9.92	14.2
Flower	7.2	**15.8**	7.6	15.3

performance of our model is content dependent and the images in our database span different chromaticities.

The ΔE^c_{94} index of our algorithm is significantly smaller than other methods over all the images except the Flower image, in which our method is the best but its difference from the Wanat and Unprocessed algorithms is not significant. In the Flower image, the three approaches: Wanat's, Unprocessed and our method all have similar performances. This similarity may be due to the dominant yellow color of this image. As described in [16], the yellow hues appear less saturated than other

monochromatic colors. Hence, in dark conditions, yellow is more subject to losing its colorfulness. Moreover, the comparison of perceived gamuts in scenario I (see Figs. 5–12-5–15) shows that the compensated gamut is not extended towards the yellowish region of the chromaticity diagram very much. Furthermore, the results show that iCAM06 underperformed compared with other algorithms because iCAM06 is not designed for compensation purposes and is only able to predict the appearance of the image for an intended luminance.

CHAPTER 6
Conclusion and Future Work

In this thesis, the importance of addressing low-light situations in the area of color science is pointed out. Most of the theories and techniques of image processing and color science do not employ detailed models of human visual perception mechanisms, and moreover, are developed under the basic assumption of photopic viewing conditions. However, through the rapid advancement of technology and by introducing the night mode capturing/rendering possibilities in recent cameras/displays, users can achieve their goals of preserving the high perceptual fidelity of images while capturing/rendering images. Hence, the importance of having viable models and solutions for the mesopic and scotopic range of the human visual system to be deployed in these technologies becomes more and more clear.

One of the objectives of this thesis was to answer the question of how different types of noise may affect photoreceptor responses and image sensor color measurements at low light levels. Moreover, we highlighted two specific problems corresponding to, first, a lack of a good mesopic color appearance model, and second, employing perceptual color appearance models in real world image processing techniques. The spectral mesopic color vision model was proposed as an approach that can take into account the effects of noise at low light levels and rod intrusion in the mesopic range.

In Chapter 3, a photon detection modeling of photoreceptors and associated basic physical principles were used to investigate how photoreceptor responses are

affected by the photon noise and the intensity of light. We showed that the spectral power distribution of light is more prone to fluctuations when the light intensity goes low and lower. The result of this research highlights the significance of photon noise close to the detection threshold of the human visual system and even in the mesopic range. We suggest that photon noise should be incorporated into the visual appearance modeling of not only scotopic vision, but also mesopic vision. However, in the photopic range, the photon noise's effect on the mesopic color appearance phenomenon is negligible.

In Chapter 4, we examined the effects of different types of noise on color measurements of image sensors at low light levels. In this regard, a typical image sensor with a detailed noise model was implemented. The image sensor model was employed in several computational tests to investigate the color measurements at low light intensities, close to the detection threshold of the sensor, in the presence of noise. Results of this chapter can be summarized as follows: first, even an ideal image sensor without any device noise cannot measure consistent colors in the scotopic range due to the photon noise; second, in contrast to the photon noise and read noise, which make the generated samples at low light levels distributed around the high intensity samples, the dark current noise pushes the measurements towards the center of the chromaticity diagram (lower saturation values); third, dark current induces a much more severe impact on color measurements in comparison to photon noise, read noise and quantization error.

The first part of Chapter 5 discussed different mesopic color vision models, including the maximum entropy spectral model for mesopic vision, and studied them

from two different points of view: feasibility, and performance. Additionally, this chapter evaluated one of the well-known tone reproduction methods, iCAM06, in terms of the mesopic color reproduction quality. The results showed that only the Shin model and the spectral model are able to reflect the inherent nonlinearities of mesopic vision. The Cao model leads to infeasible chromaticity values near the scotopic region. The iCAM06 model exhibits a behaviour closer to the Shin and spectral models rather than the Khan or Cao models. However, iCAM06 has a clear weakness in its tone compression operator. This model assumes that an equally weighted rod response is added to the cone responses, which turns out to be incorrect. On the other hand, the proposed spectral mesopic model is inspired by current theories on mesopic vision, is intuitive, and works under scotopic and photopic situations as well as in the mesopic region. The spectral model is one of the first mesopic vision models to take advantage of the recently proposed CIE system for mesopic vision. Likewise, the spectral model gives us an estimated power spectrum for the light incident on photoreceptors, which can be exploited for obtaining the scotopic luminance value. Obtaining the scotopic luminance is necessary for most color appearance models, which involves rod-cone interaction; however, without knowing the power spectrum of the light, computing the exact amount of this quantity is not possible. Hunt proposed an approximate formula calculating the scotopic luminance of illuminants based on their photopic luminance values [149]. It is shown that for the equi-energy stimulus, $L_s = 2.26L$, where L and L_s are the photopic and scotopic luminance respectively. In the real world we are never faced with the perfect equi-energy stimulus,

and so most of the non-spectral models for mesopic vision rely on this approximate formula to get the scotopic luminance.

In the second part of Chapter 5, a color retargeting technique based on the Shin mesopic model was implemented. In this regard, the inverse of the Shin model was derived for use in compensating for color deviations on dimmed displays (to the mesopic range). The proposed method is a practical approach for perceptually rendering dark images and compensating for color deviations imposed by the human visual system while viewing a dim display. This algorithm was assessed quantitatively. Our method was able to roughly reduce the ΔE^c_{94} measure and expand the gamut area of simulated perceived images by the factor of two, compared to the unprocessed images.

To sum up, the results of this study will enable us to attain other objectives of primary concern in the machine vision research, e.g. developing image quality measures, introducing efficient denoising algorithms, developing realistic color noise perception models, addressing mesopic and scotopic conditions in current digital cameras and developing new tone mapping algorithms for rendering color images perceived more naturally.

6.1 Contributions

The contributions of this thesis are as follows:

1. Development of a photon-accurate model of cone photoreceptor responses for use in studying cone signals close to the absolute threshold of the visual system

(a) It is shown that close to the absolute threshold of the visual system, cone responses become noisy and the distribution of the chromaticity representation of cone responses form an elliptical shape over time.

(b) It is demonstrated that the spectral composition of light falling on cones affects the size and orientation of the ellipses fitted to the distribution of the chromaticity representation of the cone responses.

2. Development of a photon-accurate image sensor model to analyse the color measurement at low light levels

   (a) photon noise, read noise, and quantization error as shown to lead to uncertain measurements distributed around the noise free measurements; and the chromaticity of these noisy samples are distributed in a cloud that can be well-fit to an elliptical region in the xy-chromaticity diagram.

   (b) It is shown that, even for an ideal image sensor, in scotopic conditions, obtaining stable measurements of color is impossible due to the physical limitation imposed by the fluctuations in the photon emission rate

   (c) It is demonstrated that, as compared to the chromaticity of noise-free measurements, dark current shifts the chromaticity of measured samples towards the chromaticity of the camera black point in the xy-chromaticity diagram. The amount of this shift depends on the light levels; the lower the luminance is, the larger the amount of the shift would be.

   (d) It is shown that dark current dominates the other sensor noise types in the image sensor.

3. Development of a maximum entropy spectral modeling approach to mesopic vision
   (a) Evaluation of existing mesopic vision models
   (b) Unification of photopic, mesopic, and scotopic vision models in the spectral theory of color vision
   (c) The first mesopic vision model which takes noise into account is presented
   (d) Incorporating the recent CIE system for mesopic photometry in a color vision model
4. Development of a color retargeting approach for mesopic vision to serve image rendering algorithms
   (a) application of the Shin CAM to real world images,
   (b) derivation of the inverse of Shin's mesopic color appearance model,
   (c) development of a color retargeting approach based on Shin's model,
   (d) development of a technique for perceptual rendering of images and compensating color deviations imposed by the human visual system while viewing a dimmed display in the dark.

6.2 Future Work

In this section, some prospective extensions of the proposed research in this thesis are introduced.

6.2.1 Applying the Spectral Mesopic Color Vision Model to Real World Images

The spectral theory of color vision for mesopic vision has several benefits over the empirical models of mesopic vision, as we mentioned in Chapter 5. However, this method is proposed and evaluated for color patches, and it should be extended

according to the image appearance modeling framework for spatially complex stimuli to be appropriate for real world images [127]. Moreover, the adapting white point and the background and surround adaptation mechanisms should be incorporated in the model.

6.2.2 Spectral Color Appearance Model and Spectral Color Difference Metric for Image Quality Assessment

It is indicated in [127] that, so far, color difference measurement and color appearance modeling are treated separately; however, these two subjects should be unified because the color difference between two samples should be measured according to their perceptual attributes, which should be given by color appearance models.

As mentioned before, existing color difference formulae are not appropriate for low light levels. As an example, assume that two Munsell color patches of green and blue hues with the same Value (lightness) and Chroma are viewed under photopic conditions, and any of the introduced color difference formulae are able to distinguish between the perception of the two patches. When the luminance value falls off, the perceptual difference between the two becomes less noticeable, although the outputs of the color difference formulae remain still the same as those of the photopic situation. We may address this problem in two ways: first, the spectral color appearance model can be leveraged to take the luminance-induced effects on color perception into account; second, developing a new spectral color difference formula.

In the first approach, which is the simplest way of addressing the problem, given an image at any arbitrary light level, we can derive its perceived simulated image for photopic conditions using the color appearance model. After deriving the perceived

simulated images (for photopic conditions) from the reference and test image, we can apply the normal color difference formula based on the CIE Lab color space. The same procedure can be used for evaluating color noise in images and single patches.

In the second approach, a perceptual spectral color difference metric should be developed. This approach will introduce a new metric for calculating the color difference assuming that the spectral power distribution associated with each pixel is available or it can be estimated somehow. In this regards, we can use the spectral model introduced in Section 5.1.1, which is capable of taking the luminance-induced perceptual effects on the color difference formula into account.

The spectral power distribution can be estimated using the maximum entropy based spectral theory of color perception introduced in Section 5.1.1. Then, a color difference formula should be introduced based on the obtained spectral representation of color patches. Such a color difference formula can be superior over conventional color difference metrics in terms of precision, because in the process of projecting a high dimensional quantity into a lower dimensional space, we may lose considerable information. Using spectral estimation, we can retrieve a part of the lost information and base our prospective color difference measure in the high dimensional estimated spectral power distribution. The main assumption of this theory is that a metameric estimation of the true spectra can be obtained using the maximum entropy approach.

Two possible choices for the color difference formula (based on the true spectra or estimated spectra) are the Kullback-Leibler divergence, which is non-symmetric, or the Jeffreys divergence, which is a symmetric measure. The Kullback-Leibler

divergence is given by:

$$D_{KL}(\hat{p}(\theta_{\text{test}},\lambda)||\hat{p}(\theta_{\text{ref}},\lambda)) = \int_{\Lambda} \hat{p}(\theta_{\text{test}},\lambda) \ \ \ln(\frac{\hat{p}(\theta_{\text{test}},\lambda)}{\hat{p}(\theta_{\text{ref}},\lambda)})d\lambda \tag{6.1}$$

where $\hat{p}(\theta_{\text{test}},\lambda)$ and $\hat{p}(\theta_{\text{ref}},\lambda))$ are the estimated spectral power distribution of the test and reference image, respectively. The Jeffreys divergence can be defined as the sum of two divergences: one between $\hat{p}(\theta_{\text{test}},\lambda)$ and $\hat{p}(\theta_{\text{ref}},\lambda))$ and the other between $\hat{p}(\theta_{\text{ref}},\lambda))$ and $\hat{p}(\theta_{\text{test}},\lambda)$.

$$D_{Jeffreys}(\hat{p}(\theta_{\text{test}},\lambda)||\hat{p}(\theta_{\text{ref}},\lambda)) = D_{KL}(\hat{p}(\theta_{\text{test}},\lambda)||\hat{p}(\theta_{\text{ref}},\lambda)) + D_{KL}(\hat{p}(\theta_{\text{ref}},\lambda)||\hat{p}(\theta_{\text{test}},\lambda)) \tag{6.2}$$

However, the introduced divergences need to be modified to meet all the required specifications of a perceptual color difference metric. After defining a spectral color difference formula, such a measure can be substituted for the CIEDE2000 color difference in the S-CIELab method, and gives rise to a more promising image quality assessment metric that works for different lighting conditions.

We believe that this approach will provide a better framework for addressing the concept of perceptual color difference metric, because it is capable of taking luminance and noise into account in the color appearance modelling, while most of conventional CAMs are only valid for noise free photopic situations.

6.2.3 Image Sensor Modeling

Chapter 4 can be further extended by incorporating the exposure time and ISO setting parameters into the model and then a set of optimal adjustments for the

camera can be derived for different lighting conditions. These optimal adjustments will enable photographers to get output images with the highest SNR values.

6.2.4 The Mesopic Color Retargeting Approach

Plans for future extensions of the color retargeting approach in Chapter 5 include: first, to incorporate the proposed framework into the existing image retargeting techniques such as [2]; second, evaluating our algorithm in a subjective experiment and comparing it with a larger set of existing methods; third, addressing limitations of this model by taking into account the chromatic adaptation and surround effect in the human visual system.

6.2.5 Noise-aware Perceptual Tone Mapping Operator for Dark Images

It is pointed out in [146] that most of the existing tone mapping operators may amplify noise in the images, and dark regions of images are more prone to noise. Hence, tone mapping operators should also be aware of noise in the images and avoid boosting noise in the process of tone mapping. On the other hand, a tone mapping operator is expected to preserve the perceptual fidelity of the image, i.e. the output of the tone mapping technique should resemble the original scene as it is perceived by a human observer. Usually tone mapping operators are applied to the achromatic channel of images, but they also may impose some unwanted color changes to the output image. These color changes should be corrected using a separate color correction algorithm.

Getting a realistic output image from a tone mapping operator is contingent to bringing the three topics of CAM, tone mapping techniques and denoising algorithms

together. We quote again from Reinhard: "Color appearance models and tone mapping operators are the two sides of the same coin." Most tone mapping operators can not perform very well over low light images. Moreover, most color appearance models are developed for photopic conditions. A thorough color appearance model that can cover the entire range of the human visual system can help tone mappers to avoid imposing unwanted color changes. We could also combine our spectral mesopic color vision model, which is able to address measurement noise, with a tone mapping operator or be integrated with a tone mapper such as iCAM06.

6.2.6 Chromatic Denoising and Image Enhancement Operator for Low Light Images

The human visual system is shown to be more sensitive to achromatic noise compared with chromatic noise. However, the results of Chapters 3 and **4** depict the significance of chromatic noise in dark images. The chromatic noise at low light conditions can be captured by the image sensor, and it will be noticeable when the captured image is viewed in photopic conditions. This issue highlights the importance of removing chromatic noise from dark images.

Dark noise pushes the original chromaticity of the image toward the white point. Equation 4.23 indicates that the chromaticity of the noise-free sample, measured sample and dark current are aligned along the line connecting the noise free sample to the noise. The measured sample's amount of deviation from the noise free sample is determined by the α factor in Eq. 4.23 which is a function of the signal to noise ratio.

Dark noise is bounded in a region that encapsulates the white point in the chromaticity diagram, as shown in Fig. 4–9. However, other noise types do not

necessarily lead to physically realizable chromaticity values. Image noise can be estimated as the sum of expected values of four temporal noises: dark noise, photon shot noise, read noise and quantization noise. Among these forms of noise, the first two are of non-zero mean, and the last two have zero mean.

Chromatic denoising methods are few in number in the literature; among them, the Lucchese and Mitra chromatic filter for color images has gained the most attention [61]. This filter can work either in the u'v'Y or xyY space, and is based on the center of gravity law of additive color mixtures. However, this model presumes the noise in the image has zero mean and therefore cannot address noises with Poisson distribution. Hence, the work presented in Chapter 4 can be extended by introducing a chromatic denoising operator for low light images.

References

[1] A. Stockman and L. T. Sharpe, "Into the twilight zone: the complexities of mesopic vision and luminous efficiency," *Ophthalmic and Physiological Optics*, vol. 26, no. 3, pp. 225–239, 2006.

[2] R. Wanat and R. K. Mantiuk, "Simulating and compensating changes in appearance between day and night vision," *Proceedings of SIGGRAPH 2014*, vol. 33, pp. 147:1–147:12, 2014.

[3] D. Cao, "Color vision and night vision," *Retina*, pp. 285–299, 2012.

[4] W. Bialek, *Biophysics: searching for principles*. Princeton University Press, 2012.

[5] W. Brown and D. MacAdam, "Visual sensitivities to combined chromaticity and luminance differences," *JOSA*, vol. 39, no. 10, pp. 808–823, 1949.

[6] A. Stockman and L. T. Sharpe, "The spectral sensitivities of the middle- and long-wavelength-sensitive cones derived from measurements in observers of known genotype," *Vision research*, vol. 40, no. 13, pp. 1711–1737, 2000.

[7] M. Rezagholizadeh, T. Akhavan, A. Soudi, H. Kaufmann, and J. J. Clark, "A retargeting approach for mesopic vision: Simulation and compensation," *Journal of Imaging Science and Technology*, vol. 60, no. 1, pp. 10 410–1, 2016.

[8] M. Rezagholizadeh and J. J. Clark, "Maximum entropy spectral modeling approach to mesopic tone mapping," in *Color and Imaging Conference*, no. 1. Society for Imaging Science and Technology, 2013, pp. 154–159.

[9] M. P. Lucassen, P. Bijl, and J. Roelofsen, "The perception of static colored noise: detection and masking described by CIE94," *Color Research & Application*, vol. 33, no. 3, pp. 178–191, 2008.

[10] K. Blankenbach, A. Sycev, S. Kurbatfinski, and M. Zobl, "Optimizing and evaluating new automotive hmi image enhancement algorithms under bright

light conditions using display reflectance characteristics," *Journal of the Society for Information Display*, vol. 22, no. 5, pp. 267–279, 2014.

[11] A.-M. Chang, D. Aeschbach, J. F. Duffy, and C. A. Czeisler, "Evening use of light-emitting ereaders negatively affects sleep, circadian timing, and next-morning alertness," *Proceedings of the National Academy of Sciences*, vol. 112, no. 4, pp. 1232–1237, 2015.

[12] D. Wueller, "Low light performance of digital still cameras," in *Proc. SPIE*, vol. 8667. International Society for Optics and Photonics, 2013, pp. 86 671H–86 671H–9.

[13] A. Agah, A. Hassibi, J. D. Plummer, and P. B. Griffin, "Design requirements for integrated biosensor arrays," in *Proc. SPIE*, vol. 5699. International Society for Optics and Photonics, 2005, pp. 403–413.

[14] M. Nuutinen, O. Orenius, T. Saamanen, and P. Oittinen, "A reduced-reference method for characterizing color noise in natural images captured by digital cameras," in *Color and Imaging Conference*. Society for Imaging Science and Technology, 2010, pp. 80–85.

[15] M. Rezagholizadeh and J. J. Clark, "Photon detection and color perception at low light levels," in *Computer and Robot Vision (CRV), 2014 Canadian Conference on*. IEEE, 2014, pp. 283–290.

[16] J. J. Clark and S. Skaff, "A spectral theory of color perception," *JOSA A*, vol. 26, no. 12, pp. 2488–2502, 2009.

[17] T. Ajito, T. Obi, M. Yamaguchi, and N. Ohyama, "Expanded color gamut reproduced by six-primary projection display," in *Electronic Imaging*. International Society for Optics and Photonics, 2000, pp. 130–137.

[18] D. Shin, Y. Kim, N. Chang, and M. Pedram, "Dynamic voltage scaling of oled displays," in *Design Automation Conference (DAC), 2011 48th ACM/EDAC/IEEE*. IEEE, 2011, pp. 53–58.

[19] A. Sarkar, L. Blondé, P. Le Callet, F. Autrusseau, J. Stauder, and P. Morvan, "Modern displays: Why we see different colors, and what it means?" in *Visual Information Processing (EUVIP), 2010 2nd European Workshop on*. IEEE, 2010, pp. 1–6.

[20] T. O. Maier, A. F. Kurtz, and E. A. Fedorovskaya, "Observer metameric failure reduction method," Jul. 27 2012, uS Patent App. 13/559,647.

[21] D. Long and M. D. Fairchild, "Reducing observer metamerism in wide-gamut multiprimary displays," in *IS&T/SPIE Electronic Imaging*. International Society for Optics and Photonics, 2015, pp. 93 940T–93 940T.

[22] W. A. Thornton and W. N. Hale, "Color-imaging primaries and gamut as prescribed by the human visual system," in *Electronic Imaging*. International Society for Optics and Photonics, 1999, pp. 28–35.

[23] R. Ramanath, "Minimizing observer metamerism in display systems," *Color Research & Application*, vol. 34, no. 5, pp. 391–398, 2009.

[24] F. Koenig, K. Ohsawa, M. Yamaguchi, N. Ohyama, and B. Hill, "Multiprimary display: discounting observer metamerism," in *9th Congress of the International Color Association*. International Society for Optics and Photonics, 2002, pp. 898–901.

[25] J. Bergquist, "52.2: Display with arbitrary primary spectra," in *SID Symposium Digest of Technical Papers*, vol. 39, no. 1. Wiley Online Library, 2008, pp. 783–786.

[26] M. D. Fairchild and D. R. Wyble, "Mean observer metamerism and the selection of display primaries," in *Color and Imaging Conference*, vol. 2007, no. 1. Society for Imaging Science and Technology, 2007, pp. 151–156.

[27] A. Sarkar, L. Blondé, P. L. Callet, F. Autrusseau, P. Morvan, and J. Stauder, "Toward reducing observer metamerism in industrial applications: colorimetric observer categories and observer classification," in *Color and Imaging Conference*, vol. 2010, no. 1. Society for Imaging Science and Technology, 2010, pp. 307–313.

[28] S. W. Zamir, J. Vazquez-Corral, and M. Bertalmio, "Gamut mapping in cinematography through perceptually-based contrast modification," *Selected Topics in Signal Processing, IEEE Journal of*, vol. 8, no. 3, pp. 490–503, 2014.

[29] R. Kimmel, D. Shaked, M. Elad, and I. Sobel, "Space-dependent color gamut mapping: A variational approach," *Image Processing, IEEE Transactions on*, vol. 14, no. 6, pp. 796–803, 2005.

[30] N. Bonnier, F. Schmitt, H. Brettel, and S. Berche, "Evaluation of spatial gamut mapping algorithms," in *Color and Imaging Conference*, vol. 2006, no. 1. Society for Imaging Science and Technology, 2006, pp. 56–61.

[31] J. Morovic and Y. Wang, "A multi–resolution, full–colour spatial gamut mapping algorithm," in *Color and Imaging Conference*, vol. 2003, no. 1. Society for Imaging Science and Technology, 2003, pp. 282–287.

[32] R. Bala, R. deQueiroz, R. Eschbach, and W. Wu, "Gamut mapping to preserve spatial luminance variations," *Journal of Imaging Science and Technology*, vol. 45, no. 5, pp. 436–443, 2001.

[33] S. W. Zamir, J. Vazquez-Corral, and M. Bertalmío, "Gamut extension for cinema: psychophysical evaluation of the state of the art and a new algorithm," in *IS&T/SPIE Electronic Imaging*. International Society for Optics and Photonics, 2015, pp. 93 940U–93 940U–12.

[34] M. J. Murdoch, D. Sekulovski, and I. Heynderickx, "Preferred color gamut boundaries for wide-gamut and multiprimary displays," *Color Research & Application*, vol. 39, no. 2, pp. 169–178, 2014.

[35] S. Nakauchi, S. Hatanaka, and S. Usui, "Color gamut mapping based on a perceptual image difference measure," *Color Research & Application*, vol. 24, no. 4, pp. 280–291, 1999.

[36] H. Anderson, E. K. Garcia, and M. R. Gupta, "Gamut expansion for video and image sets," in *Image Analysis and Processing Workshops, 2007. ICIAPW 2007. 14th International Conference on*. IEEE, 2007, pp. 188–191.

[37] R. L. Heckaman and J. Sullivan, "18.3: Rendering digital cinema and broadcast tv content to wide gamut display media," in *SID Symposium Digest of Technical Papers*, vol. 42, no. 1. Blackwell Publishing Ltd, 2011, pp. 225–228.

[38] J. Laird, R. Muijs, and J. Kuang, "Development and evaluation of gamut extension algorithms," *Color Research & Application*, vol. 34, no. 6, pp. 443–451, 2009.

[39] E. Reinhard, "Tone reproduction and color appearance modeling: two sides of the same coin?" in *Final Program and Proceedings - IS & T/SID Color Imaging Conference*, 2011, pp. 171–176.

[40] M. Nuutinen and P. Oittinen, "Reduced-reference methods for measuring quality attributes of natural images in imaging systems," Ph.D. dissertation, Aalto University, Finland, 2012.

[41] U. Engelke and H.-J. Zepernick, "Perceptual-based quality metrics for image and video services: a survey," in *Next Generation Internet Networks, 3rd EuroNGI Conference on*. IEEE, 2007, pp. 190–197.

[42] G. M. Johnson and M. D. Fairchild, "A top down description of s-cielab and ciede2000," *Color Research & Application*, vol. 28, no. 6, pp. 425–435, 2003.

[43] S.-J. Han, L. Xu, H. Yu, R. J. Wilson, R. L. White, N. Pourmand, and S. X. Wang, "CMOS integrated DNA microarray based on GMR sensors," in *International Electron Devices Meeting 2006 (IEDM'06)*. IEEE, 2006, pp. 1–4.

[44] Y. Ma, X. Gu, and Y. Wang, "Color discrimination enhancement for dichromats using self-organizing color transformation," *Information Sciences*, vol. 179, no. 6, pp. 830–843, 2009.

[45] A. K. Kvitle, M. Pedersen, and P. Nussbaum, "Quality of color coding in maps for color deficient observers," *Electronic Imaging*, vol. 2016, no. 20, pp. 1–8, 2016.

[46] G. M. Machado, "A model for simulation of color vision deficiency and a color contrast enhancement technique for dichromats," Master's thesis, Universidade Federal Do Rio Grande Do Sul.

[47] T. Wachtler, U. Dohrmann, and R. Hertel, "Modeling color percepts of dichromats," *Vision Research*, vol. 44, no. 24, pp. 2843–2855, 2004.

[48] G. V. Paramei, D. L. Bimler, and C. R. Cavonius, "Effect of luminance on color perception of protanopes," *Vision Research*, vol. 38, no. 21, pp. 3397–3401, 1998.

[49] M. Shohara and K. Kotani, "Modeling and application of color noise perception dependent on background color and spatial frequency," in *18th IEEE International Conference on Image Processing (ICIP) 2011,*. IEEE, 2011, pp. 1689–1692.

[50] ——, "Measurement of color noise perception," in *17th IEEE International Conference on Image Processing (ICIP), 2010*. IEEE, 2010, pp. 3225–3228.

[51] J. Kuang, X. Jiang, S. Quan, and A. Chiu, "Perceptual color noise formulation," in *Electronic Imaging 2005*. International Society for Optics and Photonics, 2005, pp. 90–97.

[52] M. Shohara and K. Kotani, "The dependence of visual noise perception on background color and luminance," in *Picture Coding Symposium (PCS), 2010*. IEEE, 2010, pp. 594–597.

[53] G. M. Johnson and M. D. Fairchild, "The effect of opponent noise on image quality," in *Electronic Imaging 2005*. International Society for Optics and Photonics, 2005, pp. 82–89.

[54] K. Sakatani and T. Itoh, "A new metric for color noise evaluation based on chroma and hue-angle," in *International Conference on Digital Printing Technologies*. IS & T Society for Imaging Science and Technology, 1997, pp. 574–578.

[55] X. Song, G. M. Johnson, and M. D. Fairchild, "Minimizing the perception of chromatic noise in digital images," in *Color and Imaging Conference*. Society for Imaging Science and Technology, 2004, pp. 340–346.

[56] J. Kleinmann and D. Wueller, "Investigation of two methods to quantify noise in digital images based on the perception of the human eye," in *Electronic Imaging 2007*. International Society for Optics and Photonics, 2007, pp. 64 940N–64 940N.

[57] S. K. Naik and C. Murthy, "Hue-preserving color image enhancement without gamut problem," *Image Processing, IEEE Transactions on*, vol. 12, no. 12, pp. 1591–1598, 2003.

[58] L. Lucchese and S. Mitra, "Filtering color images in the xyY color space," in *Image Processing, 2000. Proceedings. 2000 International Conference on*, vol. 3, 2000, pp. 500–503 vol.3.

[59] L. Lucchese, S. Mitra, and J. Mukherjee, "A new algorithm based on saturation and desaturation in the xy chromaticity diagram for enhancement and re-rendition of color images," in *Image Processing, 2001. Proceedings. 2001 International Conference on*, vol. 2. IEEE, 2001, pp. 1077–1080.

[60] L. Lucchese and S. K. Mitra, "A new method for denoising color images," in *Image Processing. 2002. Proceedings. 2002 International Conference on*, vol. 2. IEEE, 2002, pp. II–373.

[61] ——, "A new filtering scheme for processing the chromatic signals of color images: definition and properties," in *Multimedia Signal Processing, 2002 IEEE Workshop on*. IEEE, 2002, pp. 93–96.

[62] ——, "A new class of chromatic filters for color image processing. theory and applications," *Image Processing, IEEE Transactions on*, vol. 13, no. 4, pp. 534–548, 2004.

[63] M. D. Fairchild, *Color appearance models*. John Wiley & Sons, 2013.

[64] M. Rezagholizadeh and J. J. Clark, "Image sensor modeling: Color measurement at low light levels," *Journal of Imaging Science and Technology*, vol. 58, no. 3, pp. 30 401–1, 2014.

[65] J. Shin, N. Matsuki, H. Yaguchi, and S. Shioiri, "A color appearance model applicable in mesopic vision," *Optical review*, vol. 11, no. 4, pp. 272–278, 2004.

[66] E. Reinhard, W. Heidrich, P. Debevec, S. Pattanaik, G. Ward, and K. Myszkowski, *High dynamic range imaging: acquisition, display, and image-based lighting*. Morgan Kaufmann, 2010.

[67] J. Decuypere, J.-L. Capron, T. Dutoit, and M. Renglet, "Mesopic contrast measured with a computational model of the retina," in *Proceedings of CIE 2012 Lighting Quality and Energy Efficiency*, 2012, pp. 77–84.

[68] G. Polymeropoulos, N. Bisketzis, and F. Topalis, "A tetrachromatic model for colorimetric use in mesopic vision," *Color Research & Application*, vol. 36, no. 2, pp. 82–95, 2011.

[69] Y. Kwak, L. W. MacDonald, and M. R. Luo, "Mesopic color appearance," in *Electronic Imaging 2003*. International Society for Optics and Photonics, 2003, pp. 161–169.

[70] T. Ishida, "Color identification data obtained from photopic to mesopic illuminance levels," *Color Research & Application*, vol. 27, no. 4, pp. 252–259, 2002.

[71] D. Cao, J. Pokorny, V. C. Smith, and A. J. Zele, "Rod contributions to color perception: linear with rod contrast," *Vision research*, vol. 48, no. 26, pp. 2586–2592, 2008.

[72] A. Stockman, "Color vision mechanisms," Ph.D. dissertation, University of Pennsylvania, 2010.

[73] S. M. Khan and S. N. Pattanaik, "Modeling blue shift in moonlit scenes by rod cone interaction," *Journal of VISION*, vol. 4, no. 8, p. 316a, 2004.

[74] P. G. Barten, *Contrast sensitivity of the human eye and its effects on image quality*. SPIE press, 1999, vol. 72.

[75] D. Baylor, "How photons start vision," *Proceedings of the National Academy of Sciences*, vol. 93, no. 2, pp. 560–565, 1996.

[76] D. Baylor, T. Lamb, and K.-W. Yau, "Responses of retinal rods to single photons." *The Journal of physiology*, vol. 288, pp. 613–634, 1979.

[77] F. Rieke and D. Baylor, "Single-photon detection by rod cells of the retina," *Reviews of Modern Physics*, vol. 70, no. 3, pp. 1027–1036, 1998.

[78] B. Sakitt, "Counting every quantum," *The Journal of physiology*, vol. 223, no. 1, pp. 131–150, 1972.

[79] V. Lakshminarayanan, "Vision and the single photon," in *Optics & Photonics 2005*. International Society for Optics and Photonics, 2005, pp. 332–337.

[80] G. W. Schwartz and F. Rieke, "Controlling gain one photon at a time," *eLife*, vol. 2, 2013.

[81] D. Baylor, B. Nunn, and J. Schnapf, "Spectral sensitivity of cones of the monkey macaca fascicularis." *The Journal of Physiology*, vol. 390, no. 1, pp. 145–160, 1987.

[82] F. Naarendorp, T. M. Esdaille, S. M. Banden, J. Andrews-Labenski, O. P. Gross, and E. N. Pugh, "Dark light, rod saturation, and the absolute and incremental sensitivity of mouse cone vision," *The Journal of Neuroscience*, vol. 30, no. 37, pp. 12 495–12 507, 2010.

[83] M. F. Deering, "A photon accurate model of the human eye," in *ACM Transactions on Graphics (TOG)*, vol. 24, no. 3. ACM, 2005, pp. 649–658.

[84] S. Hecht, S. Shlaer, and M. H. Pirenne, "Energy, quanta, and vision," *The Journal of general physiology*, vol. 25, no. 6, pp. 819–840, 1942.

[85] T. Cornsweet, *Visual perception*. Academic press, 2012.

[86] G. Wyszecki and W. S. Stiles, *Color Science*. Wiley New York, 1982.

[87] S. L. Elliott and D. Cao, "Scotopic hue percepts in natural scenes," *Journal of vision*, vol. 13, no. 13, pp. 15–15, 2013.

[88] P. Kellnhofer, T. Ritschel, P. Vangorp, K. Myszkowski, and H.-P. Seidel, "Stereo day-for-night: Retargeting disparity for scotopic vision," *ACM Transactions on Applied Perception (TAP)*, vol. 11, no. 3, p. 15, 2014.

[89] W. B. Thompson, P. Shirley, and J. A. Ferwerda, "A spatial post-processing algorithm for images of night scenes," *Journal of Graphics Tools*, vol. 7, no. 1, pp. 1–12, 2002.

[90] P. Kellnhofer, T. Ritschel, K. Myszkowski, E. Eisemann, and H.-P. Seidel, "Modeling luminance perception at absolute threshold," in *Computer Graphics Forum*, vol. 34, no. 4. Wiley Online Library, 2015, pp. 155–164.

[91] J. Pokorny, M. Lutze, D. Cao, and A. J. Zele, "The color of night: Surface color perception under dim illuminations," *Visual Neuroscience*, vol. 23, no. 3-4, pp. 525–530, 2006.

[92] J. J. McCann, "Colors in dim illumination and candlelight," in *Color and Imaging Conference*, vol. 2007, no. 1. Society for Imaging Science and Technology, 2007, pp. 313–318.

[93] J. A. Ferwerda, S. N. Pattanaik, P. Shirley, and D. P. Greenberg, "A model of visual adaptation for realistic image synthesis," in *Proceedings of the 23rd annual conference on Computer graphics and interactive techniques*. ACM, 1996, pp. 249–258.

[94] J. J. McCann and J. L. Benton, "Interaction of the long-wave cones and the rods to produce color sensations," *JOSA*, vol. 59, no. 1, pp. 103–106, 1969.

[95] A. G. Kirk and J. F. O'Brien, "Perceptually based tone mapping for low-light conditions," *ACM Trans. Graph.*, vol. 30, no. 4, p. 42, 2011.

[96] M. Rezagholizadeh and J. J. Clark, "Image sensor modeling: Noise and linear transformation impacts on the color gamut," in *Computer and Robot Vision (CRV), 2015 12th Conference on*. IEEE, 2015, pp. 169–175.

[97] P. D. Burns, "Analysis of image noise in multispectral color acquisition," Ph.D. dissertation, Rochester Institute of Technology, 1997.

[98] R. W. G. Hunt, "Revised colour-appearance model for related and unrelated colours," *Color Research & Application*, vol. 16, no. 3, pp. 146–165, 1991. [Online]. Available: http://dx.doi.org/10.1002/col.5080160306

[99] M. D. Fairchild, "Rlab: a color appearance space for color reproduction," in *IS&T/SPIE's Symposium on Electronic Imaging: Science and Technology*. International Society for Optics and Photonics, 1993, pp. 19–30.

[100] ——, "A revision of ciecam97s for practical applications," *Color Research & Application*, vol. 26, no. 6, pp. 418–427, 2001.

[101] N. Moroney, M. D. Fairchild, R. W. Hunt, C. Li, M. R. Luo, and T. Newman, "The ciecam02 color appearance model," in *Color and Imaging Conference*, vol. 2002, no. 1. Society for Imaging Science and Technology, 2002, pp. 23–27.

[102] M. D. Fairchild, *Color appearance models*. Wiley, 2005.

[103] U. Stabell and B. Stabell, "Scotopic contrast hues triggered by rod activity," *Vision research*, vol. 15, no. 10, pp. 1115–1118, 1975.

[104] R. Hunt, "An improved predictor of colourfulness in a model of colour vision," *Color Research & Application*, vol. 19, no. 1, pp. 23–26, 1994.

[105] Y. Kwak, L. W. MacDonald, and M. R. Luo, "Prediction of lightness in mesopic vision," in *Color and Imaging Conference*, vol. 2003, no. 1. Society for Imaging Science and Technology, 2003, pp. 301–307.

[106] R. Wanat and R. K. Mantiuk, "A comparison of night vision simulation methods for video," in *Proceedings of the 11th European Conference on Visual Media Production*. ACM, 2014, p. 16.

[107] Z. Vas, P. Bodrogi, J. Schanda, and G. Varady, "The non-additivity phenomenon in mesopic photometry," *Light & Engineering*, vol. 18, no. 3, 2010.

[108] K. Sagawa and K. Takeichi, "System of mesopic photometry for evaluating lights in terms of comparative brightness relationships," *JOSA A*, vol. 9, no. 8, pp. 1240–1246, 1992.

[109] Y. He, A. Bierman, and M. S. Rea, "A system of mesopic photometry," *Lighting Research and Technology*, vol. 30, no. 4, pp. 175–181, 1998.

[110] M. Viikari, A. Ekrias, M. Eloholma, and L. Halonen, "Modeling spectral sensitivity at low light levels based on mesopic visual performance," *Clinical ophthalmology (Auckland, NZ)*, vol. 2, no. 1, p. 173, 2008.

[111] L. Halonen and M. Puolakka, "Development of mesopic photometry: The new CIE recommended system," *Light and Engineering*, vol. 20, no. 2, pp. 56–61, 2012.

[112] R. W. G. Hunt, *The reproduction of colour*. Fountain Press, England, 1995.

[113] R. M. Boynton, *Human color vision*. Holt Rinehart and Winston, 1979.

[114] P. E. Debevec and J. Malik, "Recovering high dynamic range radiance maps from photographs," in *ACM SIGGRAPH*. ACM, 1997, pp. 369–378.

[115] R. Mantiuk, A. Tomaszewska, and W. Heidrich, "Color correction for tone mapping," in *Computer Graphics Forum*, vol. 28, no. 2. Wiley Online Library, 2009, pp. 193–202.

[116] T. Pouli, A. Artusi, F. Banterle, A. O. Akyüz, H.-P. Seidel, and E. Reinhard, "Color correction for tone reproduction," in *Color and Imaging Conference*, vol. 2013, no. 1. Society for Imaging Science and Technology, 2013, pp. 215–220.

[117] S. N. Pattanaik, J. A. Ferwerda, M. D. Fairchild, and D. P. Greenberg, "A multiscale model of adaptation and spatial vision for realistic image display," in *Proceedings of the 25th annual conference on Computer graphics and interactive techniques*. ACM, 1998, pp. 287–298.

[118] P. Irawan, J. A. Ferwerda, and S. R. Marschner, "Perceptually based tone mapping of high dynamic range image streams," in *Proceedings of the Sixteenth Eurographics conference on Rendering Techniques*. Eurographics Association, 2005, pp. 231–242.

[119] J. Kuang, G. M. Johnson, and M. D. Fairchild, "iCAM06: A refined image appearance model for hdr image rendering," *Journal of Visual Communication and Image Representation*, vol. 18, no. 5, pp. 406–414, 2007.

[120] F. Durand and J. Dorsey, *Interactive tone mapping*. Springer, 2000.

[121] G. Krawczyk, K. Myszkowski, and H.-P. Seidel, "Perceptual effects in real-time tone mapping," in *Proceedings of the 21st spring conference on Computer graphics*. ACM, 2005, pp. 195–202.

[122] M. Mikamo, M. Slomp, T. Tamaki, and K. Kaneda, "A tone reproduction operator accounting for mesopic vision," in *ACM SIGGRAPH ASIA 2009 Posters*. ACM, 2009, p. 41.

[123] B. Masia, G. Wetzstein, P. Didyk, and D. Gutierrez, "A survey on computational displays: Pushing the boundaries of optics, computation, and perception," *Computers & Graphics*, vol. 37, no. 8, pp. 1012–1038, 2013.

[124] M. H. Kim, T. Weyrich, and J. Kautz, "Modeling human color perception under extended luminance levels," in *ACM Transactions on Graphics (TOG)*, vol. 28, no. 3. ACM, 2009, p. 27.

[125] B. A. Wandell and E. Chichilnisky, "Color appearance in images measurements and musings," in *Color and Imaging Conference*, vol. 1994, no. 1. Society for Imaging Science and Technology, 1994, pp. 1–4.

[126] M. D. Fairchild and G. M. Johnson, "Image appearance modeling," in *Electronic Imaging 2003*. International Society for Optics and Photonics, 2003, pp. 149–160.

[127] ——, "Meet iCAM: A next-generation color appearance model," in *Color and Imaging Conference*, vol. 2002, no. 1. Society for Imaging Science and Technology, 2002, pp. 33–38.

[128] J. J. McCann, "Color gamuts in dim illumination," in *Electronic Imaging 2008*. International Society for Optics and Photonics, 2008, pp. 680 703–680 703.

[129] M. G. Raymer and K. Srinivasan, "Manipulating the color and shape of single photons," *Physics Today*, vol. 65, no. 11, pp. 32–37, 2012.

[130] R. W. Rodieck and R. W. Rodieck, *The first steps in seeing*. Sinauer Associates Sunderland, 1998.

[131] D. L. MacAdam, "Visual sensitivities to color differences in daylight," *JOSA*, vol. 32, no. 5, pp. 247–273, 1942.

[132] G. D. Field, A. P. Sampath, and F. Rieke, "Retinal processing near absolute threshold: from behavior to mechanism," *Annu. Rev. Physiol.*, vol. 67, pp. 491–514, 2005.

[133] S. W. Hasinoff, F. Durand, and W. T. Freeman, "Noise-optimal capture for high dynamic range photography," in *Computer Vision and Pattern Recognition (CVPR), 2010 IEEE Conference on*. IEEE, 2010, pp. 553–560.

[134] J. E. Farrell, F. Xiao, P. B. Catrysse, and B. A. Wandell, "A simulation tool for evaluating digital camera image quality," in *Electronic Imaging 2004*. International Society for Optics and Photonics, 2003, pp. 124–131.

[135] J. E. Farrell, P. B. Catrysse, and B. A. Wandell, "Digital camera simulation," *Applied Optics*, vol. 51, no. 4, pp. A80–A90, 2012.

[136] X. Liu, "CMOS image sensors dynamic range and SNR enhancement via statistical signal processing," Ph.D. dissertation, stanford university, 2002.

[137] J. Chen, K. Venkataraman, D. Bakin, B. Rodricks, R. Gravelle, P. Rao, and Y. Ni, "Digital camera imaging system simulation," *Electron Devices, IEEE Transactions on*, vol. 56, no. 11, pp. 2496–2505, 2009.

[138] K. Sperlich and H. Stolz, "Quantum efficiency measurements of (EM) CCD cameras: high spectral resolution and temperature dependence," *Measurement Science and Technology*, vol. 25, no. 1, p. 015502, 2014.

[139] K. K. Hamamatsu, *Opto-semiconductor Handbook*. Japan: Hamamatsu Photonics, 2009.

[140] K. Barnard, L. Martin, B. Funt, and A. Coath, "A data set for color research," *Color Research & Application*, vol. 27, no. 3, pp. 147–151, 2002.

[141] K. Barnard and B. Funt, "Camera characterization for color research," *Color Research & Application*, vol. 27, no. 3, pp. 152–163, 2002.

[142] L. I. Smith, "A tutorial on principal components analysis," 2002.

[143] C. Stark, "DSLR vs. CCD: A bench test comparison," *AstroPhoto Insight Magazine (Special Hardware Issue)*, vol. 3, no. 7, pp. 32–41, 2007.

[144] S. Amari and H. Nagaoka, *Methods of Information Geometry*. AMS Bookstore, 2000, vol. 191.

[145] G. Ward, "High dynamic range imaging," in *Color and Imaging Conference*, vol. 2001, no. 1. Society for Imaging Science and Technology, 2001, pp. 9–16.

[146] G. Eilertsen, R. K. Mantiuk, and J. Unger, "Real-time noise-aware tone mapping," *ACM Trans. Graph*, vol. 34, no. 6, p. 198, 2015.